Aspects of Small Airborne Passive Millimetre-Wave Imaging Systems

by

David Michael Patrick Smith

Dissertation presented in fulfilment of the requirements for the degree of Doctor of Philosophy in Engineering at the Engineering Faculty, Stellenbosch University

Promotor: Prof. Petrie Meyer

Department of Electrical and Electronic Engineering

March 2010

Declaration

By submitting this dissertation electronically, I declare that the entirety of the work contained therein is my own, original work, that I am the owner of the copyright thereof (unless to the extent explicitly otherwise stated) and that I have not previously in its entirety or in part submitted it for obtaining any qualification.

March 2010

Abstract

Keywords – Passive Millimetre-Wave Imaging, Image Reconstruction, Kalman Filter, Multi-Octave Stripline Multiplexer

Passive millimetre-wave (PMMW) imaging is a technique that uses radiometers to detect thermal radiation emitted and reflected by metallic and non-metallic objects. While visual and infra-red emissions are attenuated by atmospheric constituents, PMMW emissions are transmitted, resulting in consistent contrast between different objects from day to night in clear weather and in low-visibility conditions to form images for a range of security and inclement weather applications.

The use of a PMMW imaging system on a small unmanned aerial vehicle (UAV) offers extremely attractive possibilities for applications such as airborne surveillance for search and rescue operations, which are often hindered by inclement weather making visibility poor and endangering the rescuers as the search vehicle flies through the bad weather zone. The UAV would fly above the bad weather zone, with the PMMW imaging system detecting the thermal radiation emitted and reflected by objects in the MMW spectrum through the inclement weather. The 35GHz propagation window is chosen for the greater transmission through atmospheric constituents.

The design of the PMMW imaging system is severely limited by the size of the UAV, particularly in the inability to incorporate any form of optical or mechanical scanning antenna. A possible solution is a long, thin antenna array fitted under the wings of the UAV. Such an antenna has a narrow, high gain, frequency-scanned beam along the plane perpendicular to the flight path, but a very broad beam along the plane of the flight path blurs the image, making it difficult to accurately determine the position of an object or to differentiate between objects situated along the plane of the flight path.

This dissertation proposes a technique of image reconstruction based on the Kalman filter, a recursive filter that uses feedback control to estimate the state of a partially observed non-stationary stochastic process, to reconstruct an accurate image of the target area from such a detected signal. It is shown that given a simulated target area, populated with an arbitrary number of objects, the Kalman filter is able to successfully reconstruct the image using the measured antenna pattern to model the scanning process and reverse the blurring effect.

Opsomming

Sleutelwoorde – Passiewe Millimeter-Golf Beeldvorming, Beeldherwinning, Kalman Filter, Multi-Oktaaf Strookllyn Multiplekser

Passiewe millimetergolf (PMMG) beeldvorming is 'n tegniek wat van radiometers gebruik maak om termiese straling waar te neem vanaf beide metaal en nie-metaal voorwerpe. Waar optiese en infra-rooi straling attenueer word deur atmosferiese bestanddele, plant PMMG strale ongehinderd voort. Dit lei tot konstante kontras tussen verskillende voorwerpe in daglig of snags, mooi of bewolkte weer, en in ander lae-sigbaarheid toestande om beelde te vorm vir 'n wye reeks sekuriteits- of weertoepassings.

Die gebruik van PMMG beeldvorming op 'n klein onbemande lugtuig (OLT) bied aantreklike moontlikhede vir toepassings in observasie en reddingsoperasies, wat dikwels verhinder word deur bewolke weer wat reddingswerkers in gevaar stel as hul moet vlieg in toestande van lae sigbaarheid. Die OLT kan bokant die onweer vlieg, met die PMMG beeldvormer wat termiese straling in die millimetergolf spektrum vanaf voorwerpe kan waarneem in swaks weerstoestande. Vir verbeterde golfvoortplanting deur atmosferiese bestanddele, word die 35GHz band gekies.

Die ontwerp van die PMMG stelsel word geweldig beperk deur die grootte van die OLT, spesifiek deur die tuig se onvermoë om 'n antenne te huisves wat opties of meganies kan skandeer. 'n Moontlike oplossing is om gebruik te maak van 'n lang, dun antenne samestelling wat onder die OLT se vlerke geplaas word. So 'n antenne het 'n nou, hoë-aanwins bundel wat met frekwensie skandeer langs 'n vlak loodreg tot die vlugtrajek. So 'n antenne het egter 'n baie wye bundel langs die vlugtrajek, wat beeldkwaliteit verlaag en dit moeilik maak om die posisie van 'n voorwerp langs die vlugtrajek te bepaal, of om tussen veelvuldige voorwerpe te onderskei.

Hierdie proefskrif bied 'n tegniek van beeldherwinning gebaseer op die Kalman filter, 'n rekursiewe filter wat terugvoerbeheer gebruik om die toestand van 'n nie-stasionêre stochastiese proses af te skat wat slegs gedeeltelik waargeneem is, om soedoende 'n akkurate beeld van die teikenarea te herkonstrueer vanuit 'n verwronge beeld. Dit word getoon dat, gegewe 'n gesimuleerde teikenomgewing met 'n arbitrêre hoeveelheid voorwerpe, die Kalman filter suksesvol 'n beeld kan herkonstrueer deur gebruik te maak van die antenne se gemete stralingspatroon om die skanderingsproses na te boots, om sodoende die beeldkwaliteit te verhoog.

Acknowledgements

I would like to express my sincere gratitude to the following people and institutes for their support:

- My Mother, for being a mother

- My Sister, for being a sister

- Petrie Meyer, for being a supportive promoter

- The University of Stellenbosch, for being my Alma Mater

- The academic staff at the University who gave their values input

    - Prof KD Palmer, Prof JB de Swardt, Prof BM Herbst, Doctor K Hunter

- The institutes from which I received monetary support throughout my tertiary education

    - The Ashcroft Trust, Harry Crossley Foundation and the NRF

- The people at Reutech Radar Systems who supplied measurement equipment

    - Bryn, Werner and Mike

- The fellow students who worked on the same project

    - Thomas and Evan

- Carlo van Schalkwyk, who designed the controller for the antenna rotator

- Tinus Stander, who translated my Abstract into an Uittreksel

- The people at the fine mechanical workshop who built the components

    - Wessel, Lincoln and Ashley

- The people at the University of Stellenbosch who helped with the measurements

    - Martin, Dirk, André, Mark and Tinus

- The people of Room E206, for making life interesting throughout the five years of my stay

    - Marlize, Thomas, Nicola, Dirk, Tinus, André, Shaun, Madelé, Karla and Sunelle

Table of Contents

List of Figures

List of Tables

List of Acronyms

DC   Direct Current

EKF   Extended Kalman Filter

FOV   Field of View

FPA   Focal Plane Array

FPGA   Field-Programmable Gate Array

IF   Intermediate Frequency

IR   Infra-Red

LNA   Low-Noise Amplifier

LO   Local Oscillator

MMIC   Monolithic Millimetre-Wave Integrated Circuit

MMW   Millimetre-Wave

NF   Noise Figure

PDE   Partial Differential Equation

PMMW   Passive Millimetre-Wave

PSD   Positive Semi Definite

RF   Radio Frequency

TV   Total Variation

UAV   Unmanned Aerial Vehicle

UKF   Unscented Kalman Filter

Chapter 1

Introduction

Imaging techniques form an image of a target area by exploiting the emission, reflection and transmission properties of the objects within the target area. Active imaging systems expend large amounts of energy to artificially illuminate the objects within the target area and form images from the reflected illumination. Passive imaging systems form images from the natural emissions and reflections of objects within the target area.

In both cases the medium separating the radiometer from the target area plays a significant role in affecting the level of emissions that reach the radiometer. As both active and passive systems have a minimum threshold level at which emissions are detectable, an unfavourable environment can cause the level of emissions that reach the radiometer to be below this threshold, with active systems only able to expend a finite level of energy to try and artificially increase the incident emissions.

In the presence of sunlight objects can be detected by the reflected illumination concentrated within the optical region, while in the absence of sunlight objects can be detected by the emitted radiation concentrated within the Infra-Red (IR) region. In clear weather the use of optical radiometers during the day and the use of IR radiometers at night are therefore sufficient to form an image of the target area, but the presence of atmospheric constituents within the medium separating the radiometer from the target area causes significant absorption and scattering at these wavelengths.

Passive Millimetre-Wave (PMMW) imaging is a technique that uses radiometers to detect thermal radiation emitted and reflected by metallic and non-metallic objects. Millimetre-Wave (MMW) imaging systems operate within the MMW region, defined as 30GHz to 300GHz. Imaging within the MMW region in inclement weather is possible because the MMW region contains atmospheric transmission windows around 35GHz, 94GHz, 140GHz and 220GHz, where the attenuation caused by atmospheric constituents is relatively low.

Because MMW emissions are not significantly affected by the presence or absence of the natural illumination of the sun or the majority of atmospheric constituents, images formed using PMMW imaging systems have consistent contrast between different objects from day to night in clear weather and in low-visibility conditions such as fog, smoke, maritime layers and sandstorms.

These images are used in all-weather fixed and mobile land, air and sea surveillance and navigation applications, such as the location and point of origin of boats in search and rescue operations, for reconnaissance and in the detection and capture of drug traffickers. A typical system contains some form of antenna to detect the emissions, fronted by lens to focus the emissions, and some form of detection mechanism to convert the emissions to a form presentable in an image to the operator.

The use of a PMMW imaging system on a small Unmanned Aerial Vehicle (UAV) offers extremely attractive possibilities for applications such as airborne surveillance for search and rescue operations, which are often hindered by inclement weather making visibility poor and endangering the rescuers as the search vehicle flies through the bad weather zone. The UAV would fly above the bad weather zone, with the PMMW imaging system detecting the thermal radiation emitted and reflected by objects in an atmospheric transmission window of the MMW spectrum through the inclement weather.

A typical small UAV is a scaled-down model of an aeroplane and offers an inexpensive option for applications requiring a bird's eye view of a terrain, with some form of camera pointed downwards relaying images to the ground station. The images can be used for anything from beach reports during the summertime to reconnaissance missions for the many branches of the military.

The central fuselage would contain the power supply, fuel, navigation software, communication link to the ground station and for this application the majority of the imaging system. The receiver part of the radiometer would be attached to the underside of the wings of the UAV, and would have to conform to a low-profile, rectangular shape in order to minimise the effect on the areodynamics of the UAV.

This size constraint of the UAV places severe limitations on the design of the PMMW imaging system, particularly in the inability to incorporate any form of optical or mechanical scanning antenna. These techniques require motors, lenses, reflectors and mirrors that are too large, heavy and power-dependent to be supported by a small UAV.

1.1   Proposed Solution

This dissertation proposes a PMMW imaging system, designed to detect objects in low-visibility conditions within an atmospheric transmission window, for use on a small UAV, as depicted in Figure 1.1. The antenna will be fitted under the wings of a small UAV, with the rest of the imaging system contained within the fuselage. PMMW images are formed by capturing the MMW emissions from the target area and measuring the magnitude of the captured emissions.
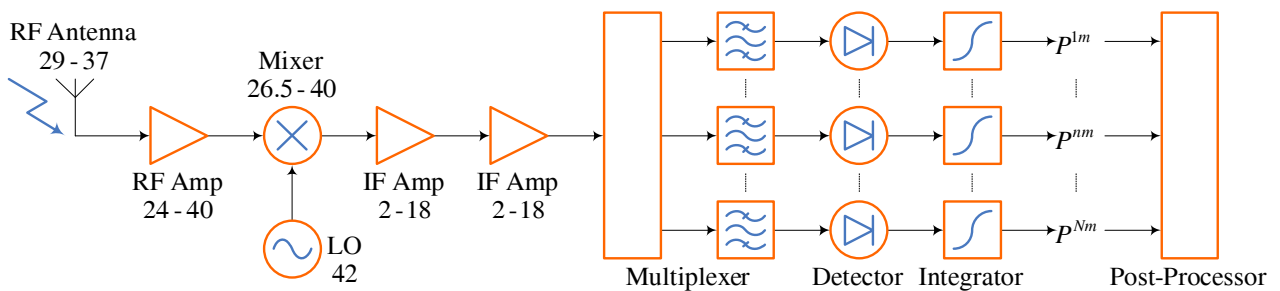
Figure 1.1: Multi-Channel Passive Millimetre-Wave Imaging Radiometer

The choice of atmospheric transmission window is a compromise between price, transmission and resolution. Technology is immature within the atmospheric transmission windows at 140GHz and 220GHz, thereby making these options not cost-effective. For a given antenna aperture size the 94GHz window has greater spatial resolution, but the 35GHz window is chosen for the greater transmission through atmospheric constituents and thin layers of absorbent materials.

The antenna couples the MMW emissions to the radiometer and the detector measures the emissions. As the detectors are operational at a lower frequency range than that of the emissions, a mixer is used to convert the emissions down using a Local Oscillator (LO). With the PMMW imaging system building an image from thermal noise measurements, the MMW emissions are weak signals that need to be strengthened by amplifiers to the level of the input dynamic range of detectors.

The size of the UAV precludes any form of optical or mechanical scanning, thereby limiting the design to one that electronically controls the orientation of the main beam along both planes. However, in using the motion of the UAV to scan along the plane of the flight path, the antenna is only required to scans along the plane perpendicular to the flight path.

The antenna is a long, thin antenna array fitted under the wings of the UAV. Such an antenna has a narrow, high gain, frequency-scanned beam along the plane perpendicular to the flight path, but a very broad beam along the plane of the flight path that blurs the image, making it difficult to accurately determine the position of an object or to differentiate between objects situated along the plane of the flight path.

As the orientation of the antenna tilts linearly as a function of frequency, by measuring the antenna over a wide frequency range the scan angle is swept over the target area. Frequency-scanning arrays are simple, inexpensive and reliable as no controlling electronics and no moving parts are required, with space-to-frequency mapping an inherent property, as depicted in Figure 1.2. While the scan angle is limited, this is an economical, compact and fast system well suited to work with the available space and power on the UAV.
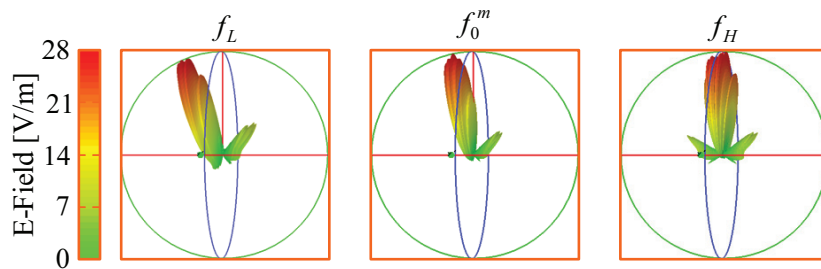
Figure 1.2: Antenna Patterns at Different Frequencies

When using a frequency-scanned array for the antenna the captured MMW emissions have to be split up into different frequency bands before detection to use the space-to-frequency mapping property of the antenna to form the images. This is done by including a multiplexer into the design, with each output channel terminated in a detector, as depicted in Figure 1.1.

The spatial resolution of an imaging system is defined by the number of resolvable pixels across the horizontal Field of View (FOV), and is directly proportional to the size of the antenna and indirectly proportional to the wavelength of the emissions. MMW wavelengths are much longer than optical and IR wavelengths, requiring much larger antennae to achieve equivalent resolution to optical and IR imaging systems. Also, the spatial resolution of an imaging system is limited by the number of channels in the multiplexer

The image is built up line by line as the antenna concurrently scans the target area along the plane perpendicular to the flight path, with each orientation θ_0^m scanned by a beam centred at frequency f_0^m. Division of the frequency range f_L to f_H into M equal-sized contiguous bandwidths each assigned to a different pixel column P^m separates the target area into bands. Division of the flight path time-period t_0 to t_N into N measurements taken at discrete time-intervals each assigned to a different pixel row P^n separates the bands into pixels.

The combination of flight-measuring and scan-filtering maps the $w \times h$ coordinate system of the target area to the $f \times t$ coordinate system of the image of size $N \times M$, as depicted in Figure 1.3. The antenna displays a narrow, high gain, frequency-scanned beam along the plane perpendicular to the flight path, but a very broad beam along the plane of the flight path that leads to a larger area than the target area being detected.
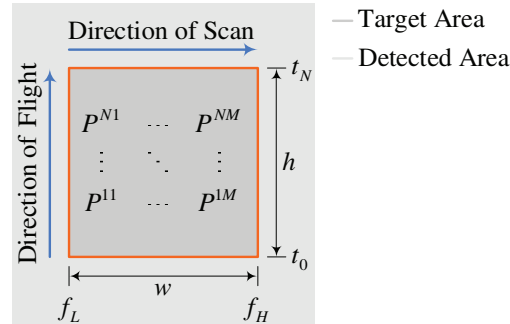
Figure 1.3: Target Area

When flying over the target area the image of an object is blurred along the plane of the flight path, making it difficult to accurately determine the position of an object or to differentiate between objects situated along the plane of the flight path. Prevention of object blurring is impossible as the size of the UAV precludes the use of bulky optics to focus the antenna pattern along the plane of the flight path as well. The only solution is to design a post-processor that reconstructs the target area from the blurred image.

As conventional image reconstruction processes deal with localised object blurring modelled by Gaussian noise, which is insufficient to counter the more global object blurring of the antenna pattern, this dissertation proposes a technique of image reconstruction based on the Kalman filter to reconstruct an accurate image of the target area from such a detected signal. It is shown that the Kalman filter is able to successfully reconstruct the image using the measured antenna pattern to model the scanning process and reverse the blurring effect.

Due to the scope of the project, this dissertation focuses only on the design of the system, the multiplexer and the image reconstruction. The full measurement of an airborne system is a major project on its own, as variations in flight path, yaw and pitch have to be factored into any image data in such a measurement. This is to form the focus of future projects. For the purposes of this work, it was shown that the system can reconstruct simulated targets using the actual measured antenna pattern successfully.

1.2   Original Contribution

The work contains two main original contribution and one smaller one.

- The first major contribution is the proposal of a PMMW imaging system that fits the spatial constraints that a typical UAV enforces

- The second major contribution is the use of a Kalman filter [1, 2] to reconstruct an image of the target from the measurements that such a system would make

- The minor contribution is the design of a contiguous, wideband, stripline, manifold-coupled multiplexer

Up until now the antennae of MMW imaging systems have been designed to obtain a main beam with high gain along both axes and is controlled using a combination of mechanical, optical and electronic techniques. These systems are large, heavy and power-dependent for a small UAV. Therefore, all aerial applications of PMMW imaging have involved large aeroplanes and helicopters capable of supporting such systems.

In this dissertation a system capable of fitting under the wing of a small UAV is designed. This severely restrict the potential realisations of the antenna, which are slightly lessened by making use of the motion of the UAV to control the orientation of the beam along one axis. The resulting antenna pattern contains only a high gain beam along one axis, with a very broad beam along the other axis.

When flying over the target area the image of an object is blurred along the plane of the flight path, making it difficult to determine the position of objects or to differentiate between objects situated along the plane of the flight path. This type of blur is not supported by conventional image reconstruction processes, which deal with localised object blurring modelled by Gaussian noise.

In this dissertation an image reconstruction algorithm capable of dealing with the global object blurring of the antenna pattern is designed. This technique of image reconstruction is based on the Kalman filter to reconstruct an accurate image of the target area from such a detected signal using the measured antenna pattern to model the scanning process and reverse the blurring effect.

A further contribution is the design of contiguous, wideband, stripline, manifold-coupled multiplexer. The majority of contiguous multiplexers function over a narrow band, where the connections between channels and junctions need only be opimised for a narrow band. The majority of multiplexers at microwave frequencies are realised in waveguide due to the loss in substrates at these frequencies.

In this dissertation the frequency range is 1.6 octaves, which results in the second harmonic of the low-band filters overlapping with the passbands of the high-band filters and which is too wide to be implemented in waveguide. While the realisation in stripline led to high in-band loss, the multiplexer is able to correctly divide up the wideband signal into the relevant bandwidths.

1.3 Contents

This dissertation describes the design of a PMMW imaging system that detects objects in low-visibility conditions within the transmission window around 35GHz. In Chapter 2 the proprieties of MMW imaging is compared with optical and IR imaging and applications of MMW imaging are presented. The PMMW imaging system is to be fitted under the wings of a small UAV, where the size of the UAV precludes any form of optical or mechanical scanning. In Chapter 3 the antenna is designed, as well as a reflector for testing purposes.

The MMW emissions are split up into different frequency bands to form the images. In Chapter 4 the multiplexer and filters used to divide of the frequency range into equal-sized contiguous bandwidths is designed. The PMMW imaging system requires good noise performance to deal with the weak MMW emissions. In Chapter 5 the analogue system required to amplify, mix down and detect the signal are designed.

The antenna displays a narrow beam along the plane perpendicular to the flight path, but a broad beam along the plane of the flight path blurs the image, making it difficult to determine the position of an object or to differentiate between objects situated along the plane of the flight path. Prevention of blurring is impossible as the size of the UAV precludes the use of bulky optics to focus the antenna pattern along the plane of the flight path. In Chapter 6 a post-processor is designed to reconstruct the target area from the blurred image.

Chapter 2

Millimetre-Wave Imaging

2.1 Introduction

Imaging techniques form an image of a target area by exploiting the emission, reflection and transmission properties of the objects within the target area, the medium separating the radiometer from the target area and any illumination incident on the target area. The effective temperature T_E of an object is [3]

$$T_E = \varepsilon T_O + \rho T_I + \tau T_B \qquad (2.1.1)$$

where emissivity ε is the measure of the ability of an object to emit the physical temperature of the object, reflectivity ρ is the measure of the ability of an object to reflect the illumination temperature incident on the object and transmissivity τ is the measure of the ability of an object to transmit the background temperature.

For the radiometer to detect an object, the medium separating the radiometer from the target area must transmit a sufficient level of the effective temperature of the object to the radiometer, while emitting a minimal level of its physical temperature and reflecting a minimal level of illumination incident on it. Therefore, the detected temperature T_D of an object is the effective temperature of the separating medium, where the effective temperature of the object is the background temperature of the medium, as depicted in Figure 2.1.
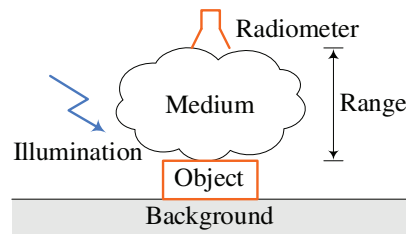
Figure 2.1: Sources of Radiation in Target Area

The emissivity, reflectivity and transmissivity of an object are a function of thickness, material, surface roughness, angle of observation, polarisation and frequency. Objects range between perfect reflectors of the incident illumination ($\varepsilon = 0$, $\rho = 1$) and perfect absorbers of the incident illumination ($\varepsilon = 1$, $\rho = 0$). An image of the target area is formed as each type of object has a different set of emission, reflection and transmission properties, thereby radiating a different effective temperature.

Active imaging systems expend large amounts of energy to artificially illuminate the objects within the target area and form images from the reflected illumination, where objects with high reflectivity are easily detected and objects with low reflectivity are easily hidden. Active imaging systems are able to control the level and geometry of the illumination within the target area, but are plagued by speckle, interference and multi-path effects.

On the other hand passive imaging systems form images from the natural emissions and reflections of objects within the target area, where objects are easily hidden when there is insufficient illumination temperature to be reflected or physical temperature to be emitted. Passive imaging systems are safe for covert and personnel applications as no detected or harmful energy is expended by the antenna and capable of mobile operations as little power is required to operate the imaging system.

The passive detection of objects is simplified by designing the imaging system to work at frequencies where naturally occurring phenomena are at an optimum. All objects with physical temperature above absolute zero emit passive radiation, with the theoretical limit at a given wavelength given by the radiation of a perfect radiator ($\varepsilon = 1$, $\rho = 0$). The radiation W from a perfect radiator is calculated from Planck's law

$$W = \frac{2hc^2}{\lambda^5} \left[\exp\left(\frac{hc}{\lambda k T_O}\right) - 1 \right]^{-1} \tag{2.1.2}$$

where c is the speed of light, h is Planck's constant, k is Boltzmann's constant and λ is the wavelength. The emitted radiation from the sun, with illumination temperature of approximately 6000K, peaks at 623THz in the optical region, while the emitted radiation from a room temperature perfect radiator, with physical temperature of approximately 300K, peaks at 31THz in the Infra-Red (IR) region, as depicted in Figure 2.2.
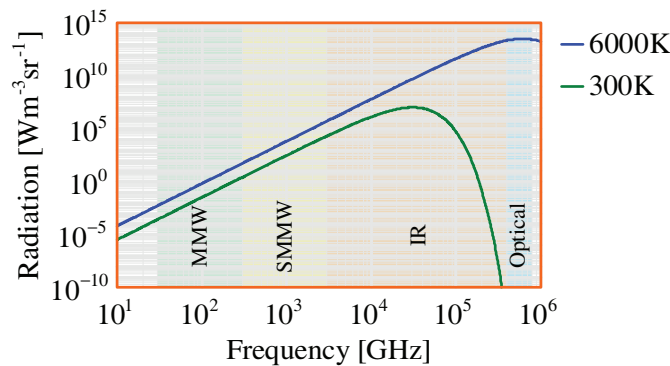
Figure 2.2: Comparison of Perfect Radiator Emissions at Passive Imaging Frequencies

In the presence of sunlight objects can be detected by the reflected illumination concentrated within the optical region, while in the absence of sunlight objects can be detected by the emitted radiation concentrated within the IR region. Therefore in clear weather optical radiometers during the day and IR radiometers at night are sufficient to form an image of the target area, but the presence of atmospheric constituents within the medium separating the radiometer from the target area causes significant attenuation at these wavelengths.

The level of absorption and scattering of radiation is dependent on the type of constituents in the atmosphere. Atmospheric molecules such as oxygen and water vapour absorb emissions at the specific frequencies where the molecules change energy levels. Small particles suspended in the atmosphere scatter emissions as a function of size, shape, refractive index and frequency. The geometrical cross-section of particles such as rain and snow obstruct emissions as a function of the ratio between particle size and wavelength.

To extend the conditions at which imaging is possible Passive Millimetre-Wave (PMMW) imaging systems have been developed in the Millimetre-Wave (MMW) region, defined as 30GHz to 300GHz. MMW emissions can be detected in low visibility conditions that limit optical and IR imaging systems. Extensive research has been performed on the properties of the MMW region, with an overview presented here.

Imaging within the MMW region in inclement weather is possible because the MMW region contains transmission windows around 35GHz, 94GHz, 140GHz and 220GHz, where the attenuation caused by atmospheric constituents is low, as presented in Table 2.1 [4] for temperature of 20°C, pressure of 101kPa and 50% humidity. The best results are achieved within the 35GHz window, with imaging severely limited by heavy rain.

Table 2.1: Attenuation caused by Atmospheric Conditions within the MMW Transmission Windows

Frequency	Attenuation			
	Clear	Drizzle (0.25mm/h)	Heavy Rain (25mm/h)	Fog (100m Visibility)
35GHz	0.13dB/km	0.25dB/km	6.49dB/km	0.50dB/km
94GHz	0.50dB/km	1.11dB/km	12.08dB/km	2.57dB/km
140GHz	1.10dB/km	1.86dB/km	13.02dB/km	5.01dB/km
220GHz	2.24dB/km	3.17dB/km	14.36dB/km	8.59dB/km

Imaging in the MMW region not only allows for imaging in certain low visibility conditions not possible with optical and IR imaging systems, but also allows for imaging through thins layers of materials that are opaque in the optical and IR regions as MMW wavelengths are longer than optical and IR wavelengths, with better transmission attained at lower frequencies. Based on a 3dB criterion, the cut-off frequencies at which certain clothing materials start becoming opaque are presented in Table 2.2 [5].

Table 2.2: Attenuation for Clothing Materials at MMW Frequencies

Fabric	Thickness	Density	Cut-off Frequency
Wool	2.2mm	$214kg/m^3$	350GHz
Linen	1.1mm	$509kg/m^3$	350GHz
Leather	0.75mm	$813kg/m^3$	400GHz
Denim	0.96mm	$490kg/m^3$	50GHz
Silk	0.36mm	$256kg/m^3$	1THz
Nylon	0.19mm	$379kg/m^3$	1THz

The properties of an object are changed when mixed with another substance. The change in the transmissivity of different types of soil when water is added is presented in Table 2.3 [6] at 10GHz. The addition of water molecules to the soil increases the absorption and scattering of emissions, resulting in an image that is able to distinguish between different levels of irrigation of agricultural land [7].

Table 2.3: Calculated Skin Depths of Soil at MMW Frequencies

Soil	Skin Depth	
	Dry	Wet (Water Content)
Loam	4.8m	0.016m (13.77%)
Sand	1.6m	0.01m (16.8%)
Clay	0.55m	0.00m (20%)

The emissivity of common materials at MMW frequencies measured at normal incidence and at one polarisation is presented in Table 2.4 [8]. The unique difference in signature in the MMW region between metallic objects, detected by strongly reflecting the illumination temperature, and non-metallic objects, detected by strongly emitting the physical temperature, result in high contrast images.

Table 2.4: Emissivity for Common Materials at MMW Frequencies

Surface	Emissivity		
	44GHz	94GHz	140GHz
Bare metal	0.01	0.04	0.06
Painted metal	0.03	0.10	0.12
Painted metal under camouflage	0.22	0.39	0.46
Smooth water	0.47	0.59	0.66
Dry gravel	0.88	0.92	0.96
Dry concrete	0.86	0.91	0.95

The ability of an MMW imaging system to distinguish between objects can clearly be seen in the study of the detected temperature of a painted metallic object under camouflage and dry gravel at 94GHz under various atmospheric conditions presented in Table 2.5 [9]. The objects have a physical temperature of 290K and are at a range of 750m from the radiometer, where $\tau = 10^{-\alpha R/10}$. The camouflaged metallic object reflecting the illuminating sky can be seen to be clearly distinguishable from the surrounding absorptive gravel background.

Table 2.5: Detected Temperature for Various Atmospheric Conditions at MMW Frequencies

Atmospheric Condition	Illumination Temperature	Detected Temperature	
		Camouflaged Object	Dry Gravel
Clear, Smoke, Light Fog ($\alpha = 0.6$dB/km)	60K	164K	273K
Thick Fog, Overcast ($\alpha = 1.0$dB/km)	120K	203K	279K
Thick Clouds ($\alpha = 2.0$dB/km)	180K	242K	284K

2.2 Basic System

The simplest system to measure MMW emissions is depicted in Figure 2.3. The antenna couples the emissions to the radiometer, the mixer converts the Radio Frequency (RF) f_{RF} signal to a lower Intermediate Frequency (IF) f_{IF} signal using the Local Oscillator (LO) frequency f_{LO}, the filter removes unwanted mixing products and the detector converts the signal to a Direct Current (DC) voltage proportional to the incident power level.
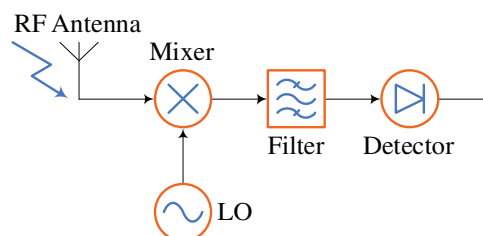
Figure 2.3: Heterodyne Radiometer

The radiometer performs a series of thermal noise measurements of the target area to form an image. The imaging process is characterised by the speed at which images are formed of the target area, the sensitivity to changes in temperature in the target area and the ability to resolve the angular separation between closely-spaced objects in the target area.

The spatial resolution of an imaging system is defined by the number N of resolvable pixels across the horizontal Field of View (FOV), θ

$$N \;=\; \frac{\theta}{\alpha} \tag{2.2.1}$$

where α is the angle subtended by the smallest resolvable object in the target area. This angle is a function of the wavelength of the incident radiation and size of the antenna

$$\alpha \;=\; \frac{\lambda}{\eta D} \tag{2.2.2}$$

where η is the refractive index of the medium and D is the largest dimension of the antenna aperture. MMW wavelengths are much longer than optical and IR wavelengths, requiring much larger antennae to achieve equivalent resolution to IR and optical imaging systems.

The thermal sensitivity of ΔT is the lowest temperature change in the target area that is detectable by the imaging system, and is defined as [10]

$$\Delta T \;=\; T_S / \sqrt{B t_s} \tag{2.2.3}$$

where B is the bandwidth of the noise, t_s is the sample time of the system and T_S is the system temperature.

The system temperature is a function of the Noise Figure (NF) and gain of the individual components

$$T_S \;=\; \left(F_1 + \frac{F_2 - 1}{G_1} + \frac{F_3 - 1}{G_1 G_2} + \ldots - 1 \right) T_O \tag{2.2.4}$$

where T_O is the physical temperature of the system, F_i is the NF of the component of stage i, G_i is the gain of the component of stage i and $L_i = 1/G_i$ is the loss of the component of stage i. The parameters of former stages are more crucial than latter stages. In order to minimise the effect of the loss of the mixer, a high-gain Low-Noise Amplifier (LNA) is needed as high up in the chain as possible.

MMW emissions of room temperature objects are between 10^{10} and 10^7 times smaller than IR emissions within the thermal imaging region of 20THz to 300THz. With 10^3 better temperature contrast in the MMW region than in the IR region [10], the LNA requires at least 10^4 times better noise performance than IR radiometers to be comparable in signal-to-noise ratio with IR imaging systems.

To operate in real time the sample time of the imaging system must be less than the refresh rate of the display. This can be achieved by increasing the number of radiometers in the imaging system, each of which is used to take measurements of different parts of the target area. The sample time t of each receiver is

$$t \;=\; \frac{t_s n}{m} \tag{2.2.5}$$

where m is the total number of pixels in the image and n is the number of radiometers in the imaging system.

The thermal sensitivity of each of these radiometers is

$$\Delta T \;=\; T_S / \sqrt{\frac{B t_s n}{m}} \tag{2.2.6}$$

where it is clear that the more pixels that each radiometer has to measure per sample time of the imaging system, the more difficult to obtain a good thermal sensitivity. Small arrays of more expensive, higher-performance radiometers are far more cost effective than large arrays of cheap radiometers because of the strong dependence of the noise temperature to thermal sensitivity ratio.

2.3   Passive Millimetre-Wave Imaging Applications

The simplest system is a single antenna operating at a single frequency directed at a single orientation raster scanned over the target area by a mechanical motor. The speed at which images are formed is increased by making use of multiple radiometers, each of which is directed at different parts of the target area, with the orientation of the antennae controlled using mechanical, optical or electronic techniques.

Systems that make use of a single antenna have an instantaneous FOV of 1×1 pixels. It is only with the mechanical motion of the antenna or the focusing optics in two dimensions that the whole FOV is measured. These systems are bulky in that they require motors and focusing optics, however the backend is quite simple, requiring only one set of analogue devices.

An example of this is for instance the system described in [11], where the single antenna is connected to an opto-mechanical scanner consisting of a high speed vertical scanner scanning the target area through $\pm 10°$ and a low speed flapping mirror that scanned the beam horizontally through an angle of $60°$, resulting in a $60° \times 20°$ FOV, with a thermal sensitivity of 2K and a spatial resolution of $0.5°$.

When the number of antennae is increased along one dimension in the form of a linear array the instantaneous FOV increases to $a \times 1$ pixels, where a is the scan angle of the array. Only motion in the dimension orthogonal to the array is required to measure the whole FOV. These systems are also bulky in that they still require motors and focusing optics and the backend is more complex, requiring up to a sets of analogue devices.

One such system is described in [12], where the orientation of the antennae are controlled electronically to cover a $30° \times 20°$ FOV, with a thermal sensitivity of 5K, spatial resolution of $0.3°$ and sample times of 33ms. A linear phased-array antenna is used, which is frequency-scanned along the orthogonal dimension. The combination of phase and frequency sorting resolved the measurements into a two-dimensional image.

When the number of antennae is increased along both dimensions in the form of a planar array the instantaneous FOV increases to $a \times b$ pixels, where a is the scan angle of the array in one dimension and b is the scan angle of the array in the other dimension, thereby mitigating the requirement for motion. These systems are compact as no motors or focusing optics are required, however the backend is very complex, requiring up to $a \times b$ sets of expensive MMW analogue devices.

In [13], where the radiometer contains a Focal Plane Array (FPA) of 40×26 individual antennae to cover a $15° \times 10°$ instantaneous FOV, with a thermal sensitivity of 0.4K, spatial resolution of $0.34°$ and sample times of 10ms. The imaging system contains a focusing lens, with each antenna connected to a Monolithic Millimetre-Wave Integrated Circuit (MMIC) that directly amplifies and detects the emissions [14], thereby mitigating the need for oscillators and lossy mixers.

So far only stationary systems have been discussed, but the imaging system can also be attached to an airborne vehicle. In the vehicle providing motion along one dimension the imaging system is only required to scan along the dimension orthogonal to this motion. If the instantaneous FOV of the radiometer is less than the whole FOV along the orthogonal dimension, some form of backward motion of the orientation of the antenna is required to compensate for the forward motion of the vehicle.

Two such systems are described in [9, 15]. In the first the radiometer attached to a helicopter is used to cover a $40° \times 1°$ FOV, with a thermal sensitivity of 0.8K, spatial resolution of $0.5°$ and sample times of 250ms. In the second the radiometer attached to a satellite is used to cover a $34° \times 1°$ FOV, with a spatial resolution of $1.4°$ and sample times of 600ms.

Because MMW emissions are not significantly affected by the presence or absence of the natural illumination of the sun or the majority of atmospheric constituents, images formed using PMMW imaging systems have consistent contrast between different objects from day to night in clear weather and in low-visibility conditions that are used in all-weather fixed and mobile land, air and sea surveillance and navigation applications.

The contrast of metal, fibreglass, wood, rubber and long, trailing wakes to a water background is used to locate boats and trace their point of origin in search and rescue operations, for surveillance and reconnaissance and in the detection and capture of drug traffickers [8]. The high transmissivity of MMW emissions through canvas and plastic coupled with the radiated emissions off human bodies has for instance been used to detect concealed personnel in soft-sided freight vehicles attempting to illegally cross borders [16].

The radiated emissions from a body of water is changed by the introduction of oil, ice and wind as they change the emissivity of the water [17]. This has been used to map the extent and thickness of an oil spill at sea [8], map sea ice movements [7] and measure wind speed [18]. The contrast in emissivity between land, water, vegetation and minerals results in the identification of surface composition of planetary systems, including portable remote sensing of lava flow [19] and mapping of annual rainfall levels [15].

The spectral behaviour of molecules in the MMW region contains a wealth of information about atmospheric chemistry. The resonant spectral lines in the MMW range provide a means of studying Earth's climate for weather monitoring and climate change research [20, 21]. Ground-based radio astronomy observatories require monitoring of the atmospheric emission, attenuation and refraction at MMWs to calibrate out the attenuation and phase delay of the earth's atmosphere in order to isolate the astronomical emissions [22].

2.4 Proposed System

The use of a PMMW imaging system on a small Unmanned Aerial Vehicle (UAV) has possibilities for applications such as airborne surveillance for search and rescue operations, which are hindered by inclement weather making visibility poor and endangering the rescuers as the search vehicle flies through the bad weather zone. The UAV would fly above the bad weather zone, with the PMMW imaging system detecting the radiation emitted and reflected by objects in a MMW atmospheric transmission window through the inclement weather.

A block diagram of the proposed system is depicted in Figure 2.4, with the aspects that were developed for this work highlighted. Due to the scope of the project the rest of the system are built up from purchased components, while the analogue-to-digital conversion, implementation of the post-processor on a Field-Programmable Gate Array (FPGA), incorporation onto an UAV and the communication link with the UAV are omitted.
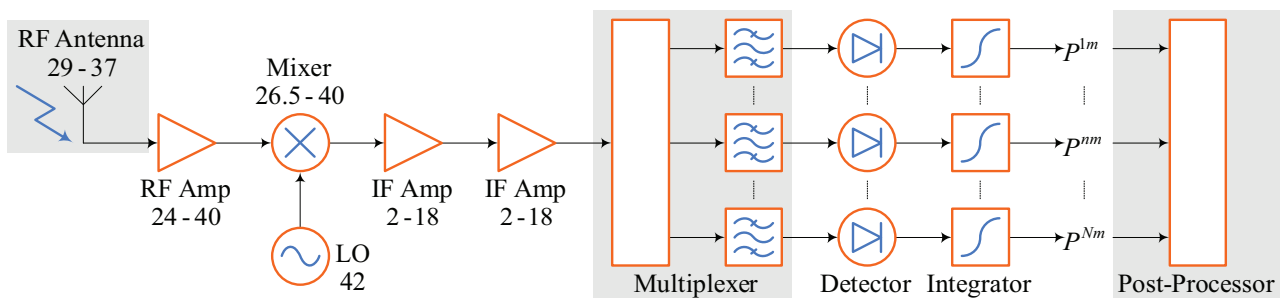
Figure 2.4: Multi-Channel Passive Millimetre-Wave Imaging Radiometer

The choice of atmospheric transmission window is a compromise between price, transmission and resolution. Technology is immature within the atmospheric transmission windows at 140GHz and 220GHz, thereby making these options not cost-effective. For a given antenna aperture size the 94GHz window has greater spatial resolution, but the 35GHz window is chosen for the greater transmission through atmospheric constituents.

The focal application for the PMMW imaging system is maritime airborne surveillance for search and rescue operations, where the PMMW imaging system is primarily required to detect an isolated boat in a sea of water. For this reason the reduced spatial resolution of the 35GHz window is acceptable as it is coupled to the improved response to environmental conditions of the 35GHz window.

The design of the PMMW imaging system is severely limited by the size of a small UAV, such as the examples presented in Table 2.6. As the imaging system is to be fitted under the wing of the UAV, the antenna must conform to the rectangular shape of the wing and have a low profile to maintain the aerodynamics of the UAV, thereby excluding any form of optical or mechanical scanning antenna. The system must be lightweight as a UAV has a limited payload and consume a minimum of power as there is limited available on a UAV.

Table 2.6: Examples of UAV Properties

UAV	Wing Span	Payload	Endurance	Cruise Speed	Altitude
Aerosonde [23]	3.45m	16.8kg	14hrs to 24hrs	50knots	4500m
Silver Fox [24]	2.4m	2.2kg	8hrs	40knots	3600m
Viking [25]	3.66m	9kg	6hrs to 8hrs	50knots	

The proposed solution is a long, thin, slotted-waveguide antenna array of dimensions $515.6 \times 9.1 \times 5.6$mm. The antenna has a narrow, high gain, frequency-scanned beam along the plane perpendicular to the flight path, but a very broad beam along the plane of the flight path. This antenna is chosen for its inherent space-to-frequency mapping, where the orientation of the main beam of the antenna pattern sweeps from an angle of $2°$ off axis at a frequency of 37GHz to an angle of $25°$ off axis at a frequency of 29GHz.

In not employing any form of active elements such as phase shifters or time delays within the antenna design, the main beam of the antenna pattern of each frequency component is directed at a fixed orientation. Therefore, the antenna only scans along a wide FOV along the plane perpendicular to the flight path, with the flight of the UAV used to provide the FOV along the plane of the flight path.

In using the flight of the UAV to sweep the main beam of the antenna pattern along the plane of the flight path, the whole frequency range must be measured concurrently because as the imaging system is propelled forward by the motion of the UAV the main beam is moved forward. Unlike the design of [9], the imaging system does not contain a mechanical motor that compensates for the motion of the UAV.

While devices such as MMICs [14, 26] are capable of direct amplification and detection at MMW frequencies, the majority of affordable, off-the-shelf detectors only operate up to 10GHz [27, 28, 29]. Therefore, a heterodyne system is employed to mix the captured MMW emissions down to a detectable frequency range using a mixer [30] covering the frequency range of 26.5GHz to 40GHz coupled to a 42GHz local oscillator [31].

The LO-mixer combination converts the captured MMW emissions from the RF range of 29GHz to 37GHz to the lower IF range of 5GHz to 12GHz, with the orientation of the main beam of the antenna pattern swept from an angle of $2°$ off axis at a frequency of 5GHz to an angle of $24°$ off axis at a frequency of 12GHz. This output is strengthened using a pair of 32dB amplifiers [32] covering the frequency range of 2GHz to 18GHz.

Of key importance in this work is the development of a first iteration of a PMMW imaging system, with provision made for future work to concentrate on one aspect only, such as increasing the scan angle of the antenna by increasing the frequency range of the antenna. For this reason components with bandwidths larger than that required by the current system were purchased. While these devices add excessive noise to the current system, these components do not need to be replaced when the frequency range is increased.

Price played a role in the chose of frequency ranges of the components. Due to industries standards certain frequencies ranges are more common, resulting in cheaper components at these frequencies. Therefore, am amplifier covering the frequency range of 2GHz to 18GHz is cheaper than one custom-made to fit the 5GHz to 13GHz IF range.

A good system temperature is required as the imaging system forms the image out of a series of thermal noise measurements of low noise, with stages near the frontend having a greater affect. As the mixer supplies 6dB of loss to the imaging system, a LNA [33] with a noise performance of 3.5dB and a gain of 20dB is placed at the output of the antenna to alleviate the effect of the loss of the mixer on the system temperature.

The output of the mixer is split up into 10 contiguous bands of size 800MHz by a stripline multiplexer. The output of each one of these bands is connected to a detector for conversion to a DC voltage proportional to the incident power level. While stripline circuits at microwave frequencies are known to be lossy, with this multiplexer supplying 10dB of loss, the wide band of the multiplexer of 1.6 octaves excluded a waveguide solution.

As the antenna has an inherent space-to-frequency mapping property, the output of each one of the channels is related only to MMW emissions from one portion of the target area. This portion covers a short distance along the plane perpendicular to the flight path due to the narrow beam along this direction. However, this portion covers a large distance along the plane of the flight path due to the very broad beam along this direction.

The blur along the plane of the flight path of the main beam of the antenna pattern would easily be focused by optics, however this is not possible because a compact, low-profile antenna is required to fit under the wings of the UAV. Therefore, an image reconstruction technique is required to reconstruct an accurate image of the target area from the detected signal.

As conventional image reconstruction processes deal with localised blurring modelled by Gaussian noise, which is insufficient to counter the global blurring of the antenna pattern, a novel technique [1, 2] based on the Kalman filter [34] is implemented that uses the measured antenna pattern to model the scanning process and reverse the blurring effect.

2.5 Conclusion

The basic outline of the proposed imaging system is described in this chapter, with each of the following chapters dedicated to an indepth study of the design, manufacture and testing of the various subsystems. This system has been proposed for applications such as airborne surveillance for search and rescue operations because of the unique ability of MMW emissions to be detected in inclement weather. However, the size of the UAV restricts the ability to focus the antenna pattern along both axes, with a novel technique proposed to reconstructed the target area.

Chapter 3

Antenna

3.1 Introduction

For any type of radiometric scanning the antenna is one of the crucial aspects in the system, as it is the device that couples the emissions in free-space to the rest of the system. Two elements of the antenna in particular are of great importance, namely the shape of the beam and the scanning ability. While any design tries to optimise these elements, the environment that the antenna will operate in, namely the wing of a Unmanned Aerial Vehicle (UAV) in this work, places restriction on the shape, dimensions and operation of the antenna.

For the purposes of this dissertation an existing antenna was used [35]. As the characteristics of the antenna are the basis of the system and the image reconstruction algorithm, this chapter gives a short description of the design and the key concepts. This is followed by an indepth explanation of the characterisation of the antenna performed as part of this dissertation for use by the image reconstruction algorithm.

3.2 Antenna

In general, beam forming and beam scanning of antenna are achieved using electronic, optical and mechanical techniques [36]. Beam forming is normally performed by increasing the electrical size of the antenna, as depicted in Figure 3.1. This is achieved mechanically by increasing the physical dimensions of the antenna aperture, optically by focusing the emissions to be captured by the antenna using a reflector, lens or mirror or electronically by increasing the number of antenna in the form of an array.
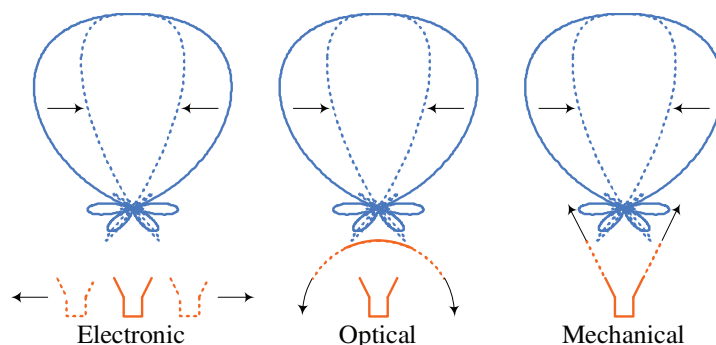
Figure 3.1: Beam Forming Techniques

On the other hand, beam scanning is achieved by repositioning the orientation of main beam of the antenna pattern, as depicted in Figure 3.2. This is achieved mechanically by physical movement of the antenna in the case of the single antenna or antenna array, optically by physical movement or rotation of the reflector, lens or mirror that is being used to focus the emissions to be captured or electronically by adding phase shifts between the antenna elements in the case of the antenna array.
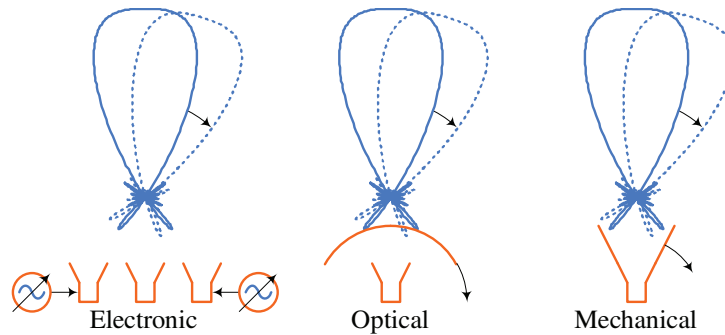
Figure 3.2: Beam Scanning Techniques

The scan angle of mechanical and optical techniques is not limited by the antenna itself and is arbitrarily set by the motor positioning of the antenna and focusing optics. Beam forming in mechanical and optical techniques is determined by the geometric cross-sections of the aperture and focusing optics. The profile in mechanical and optical techniques is fixed by the displacement of the antenna to the focal point of the optics.

The application considered in this dissertation requires an antenna that can be fitted under the wings of a small UAV, thereby placing constraints of size, weight and power on the antenna design to minimise the affect on the aerodynamics of the UAV. The motors, apertures and optics required by mechanical and optical techniques can therefore not be considered as alternatives because they are large, heavy, cumbersome and slow.

It follows that the solution in this work is an antenna array with a main beam that is electronically controlled in two planes. However, if one could use the motion of the UAV to scan along the plane of the flight path, the antenna is only required to scan along the plane perpendicular to the flight path. Such an antenna would need a narrow, high gain beam along the plane perpendicular to the flight path, but will have a very broad beam along the plane of the flight path. Prevention of object blurring in this case is impossible as the size of the UAV precludes the use of bulky optics to focus the antenna pattern along the plane of the flight path as well.

The characteristics of array antennae are determined by the combined effect of the number N of elements, the spacing d between the elements, the amplitude excitation of the individual elements and the phase excitation of the individual elements [37, 38], as depicted in Figure 3.3. By controlling the phase of the individual elements the orientation θ of the main beam is scanned electronically over the target area at a faster rate and in a more flexible manner than that achieved by mechanical and optical techniques.
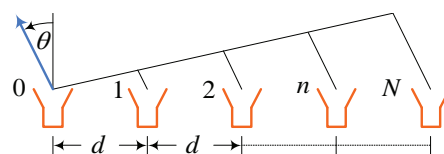
Figure 3.3: Antenna Array

The phase of the antenna is normally controlled actively by adding a phase shifter or time-delay circuit to each element [37, 38], as depicted in Figure 3.4. The scan angle is swept by changing the incremental phase shift ψ of $\frac{2\pi}{\lambda} d \sin \theta_0$ between adjacent elements or by changing the incremental delay τ of $\frac{d}{c} \sin \theta_0$ between adjacent elements, where c is the velocity of propagation. For high gain arrays containing numerous elements this type of steering becomes very expensive, especially in the Millimetre-Wave (MMW) region.
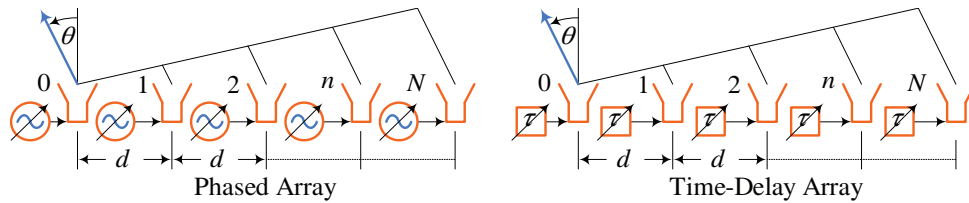
Figure 3.4: Electronic Beam Scanning

An alternative is to use a fixed array so constructed that the main beam scans over a given Field of View (FOV) as a linear function of frequency [37, 38], as depicted in Figure 3.5. Frequency-scanning arrays are simple, inexpensive and reliable as no expensive controlling electronics and no moving parts are required. While the scan angle is limited, this is an economical, compact and fast system well suited to work with the space and power on the UAV.
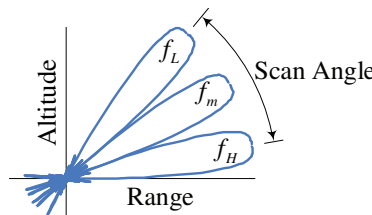
Figure 3.5: Frequency Beam Scanning

Frequency scanning arrays can be implemented either in microstrip or waveguide. Microstrip arrays consist of radiating elements, fed by a microstrip network. They are low cost, light weight, easy to fabricate and low in profile. There is a lot of flexibility in the design of the feed network and radiating elements. However microstrip arrays have high loss at MMW frequencies.

Slotted waveguide arrays consist of resonant or leaky-wave slots cut into one of the walls of a waveguide feed, as depicted in Figure 3.6. Meander waveguides are compact and have a large scan angle, but are mechanically complex and incur high losses in the bends and additional line lengths. Straight waveguides have a small scan angle, but are simple to machine and incur low losses. Operating near cut-off does increase the scan angle, but is sensitive to manufacturing tolerances and has a very non-linear space to frequency mapping.
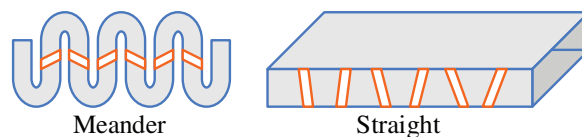
Figure 3.6: Frequency-Scanned Array

For this work, a frequency-scanned array [39] was used to concurrently scan the whole FOV along the plane perpendicular to the flight path. The image is then formed by dividing the captured emissions into frequency bands, each band containing emissions from a different orientation. The elements of the array are equally-spaced and incorporate a weighting amplitude function to minimise side-lobes.

The array implementation is the classic slotted waveguide array that is an excellent solution to the problem at hand, with a shape factor that conform very well to the essentially cross-shaped layout of a UAV. It must be noted at this stage that a fundamental assumption made when proposing a frequency-scanned array as a viable option, is that the power-density spectrum of the objects that need to be detected do not vary by much over the scan bandwidth.

The design specifications of the antenna are presented in Table 3.1. The waveguide dimensions need to be chosen to be able to support the propagation of the desired frequency range f_L to f_H, the slot spacings are set to orient the main beam of the antenna pattern to the desired angle for a given frequency, the number of slots determine the angle subtended by the 3dB beamwidth and the amplitude excitation of the individual elements fix the maximum level of the sidelobes.

Table 3.1: Frequency-Scanned Linear Antenna Array Specifications

Parameter	Value
Frequency Range (f_L to f_H)	29GHz to 37GHz
Scan Angle (θ_L to θ_H)	24° to 2°
3dB Beamwidth	1°
Sidelobe Level	$-21\text{dB}_{\text{max}}$

The antenna is designed using the travelling-wave method, which allows for non-resonant spacing and arbitrary beam placement. This method begins with an equivalent circuit of of lumped elements with admittance Y_n^A spaced d apart, as depicted in Figure 3.7, where G_0 is the conductance of the matched load. The antenna order N determines the angle subtended by the 3dB beamwidth, with an order N of 110 required to obtain the 3dB beamwidth of 1°.
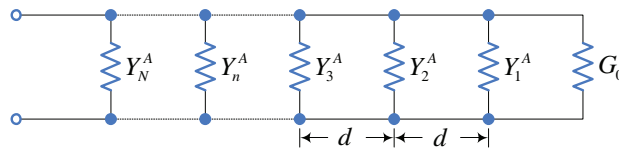
Figure 3.7: Travelling-Wave Array Equivalent Circuit

The FOV is chosen to scan from directly beneath the UAV to one side of the UAV so that an antenna was placed on either wing the two antenna patterns would not overlap. The scan angle θ_0 for a given frequency f can be calculated by equating the phase β of $\frac{2\pi}{\lambda_g}d$ between the elements in the waveguide with the phase $\frac{2\pi}{\lambda}d\sin\theta$ in free-space, that is

$$\theta_0 = \arcsin\left(\sqrt{1 - \left(\frac{\lambda}{2a}\right)^2} - \frac{\lambda n}{d}\right) \tag{3.2.1}$$

where λ is the wavelength in free-space, λ_g is the wavelength in the waveguide, a is the inner broad wall dimension of the waveguide and $n = 1/2$.

With the spacing between the elements set to 4.73mm to obtain a scan angle of $\theta_H = 2°$ at $f_H = 37\text{GHz}$, the scan angle over the whole frequency range is inherently set. The scan angle at nine frequency points within the frequency range are presented in Table 3.2, as calculated using Equation 3.2.1.

Table 3.2: Theoretical Orientation of Main Beam of Far-Field Pattern

Frequency	Orientation	Frequency	Orientation	Frequency	Orientation
29GHz	24.0°	32GHz	13.8°	35GHz	6.2°
30GHz	20.2°	33GHz	11.0°	36GHz	4.0°
31GHz	16.8°	34GHz	8.5°	37GHz	2.0°

The amplitude weighting is based on standard aperture distribution synthesis [37]. The Villeneuve array synthesis [40] is used because is has been developed directly for discrete arrays. The necessary element weights a_n are calculated, as depicted in Figure 3.8, to obtain a pattern with a maximum sidelobe level of 21dB below the main beam and for 6 sidelobes adjacent to main beam which have equal height.
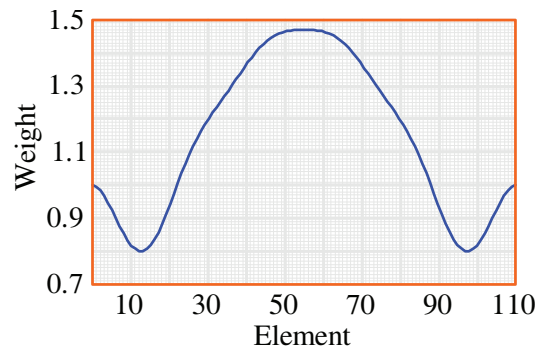
Figure 3.8: Antenna Array Element Amplitude Weights

Lumped elements are calculated for 7% power dissipation in the load as chosen in [35], for a loss of 0.7dB/m within the waveguide and with coupling between slots taken into account [41]. The lumped elements are converted to slots as presented in Appendix A.1, using CST MWS [42] simulations performed at 33.5GHz on 1.5mm thick slots with the wall containing the slots skimmed down by 0.8mm to obtain the necessary coupling.

The antenna is simulated in CST using time-domain analyses with nine far-field probes at frequencies within the frequency range. Cut-planes are made to determine the orientation θ_0 of the main beam of the antenna pattern as a function of frequency, with the orientation presented in Table 3.3.

Table 3.3: CST MWS Simulated Orientation of Main Beam of Far-Field Pattern

Frequency	Orientation	Frequency	Orientation	Frequency	Orientation
29GHz	21.7°	32GHz	13.6°	35GHz	7.0°
30GHz	18.6°	33GHz	11.6°	36GHz	4.6°
31GHz	15.9°	34GHz	9.0°	37GHz	2.7°

The simulated 3D far-field patterns obtained from the far-field probes in CST are depicted in Figure 3.9. The antenna has a narrow, high gain, frequency-scanned beam along the plane perpendicular to the flight path, but a very broad beam along the plane of the flight path.
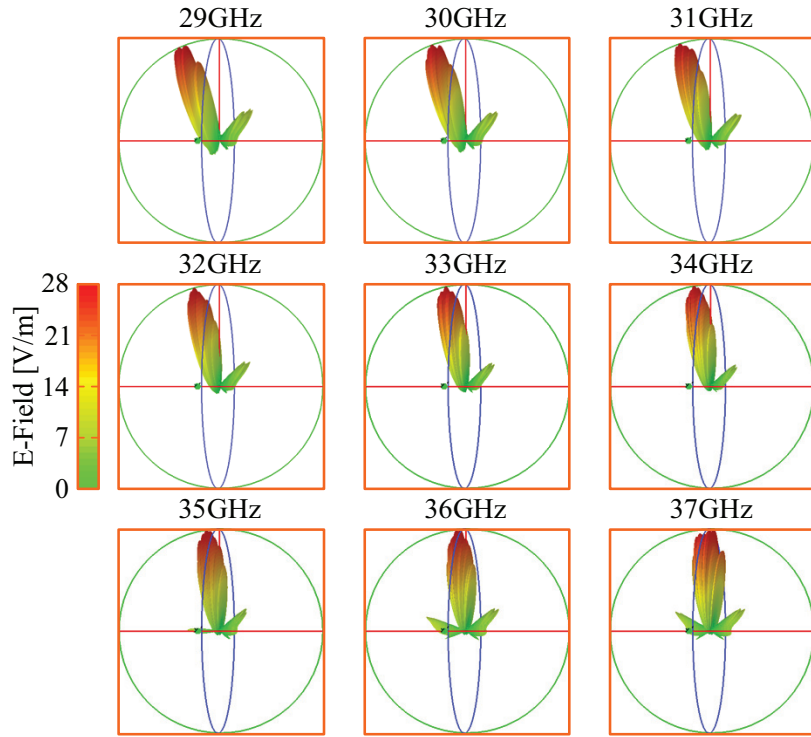
Figure 3.9: CST MWS Simulated 3D Far-Field Patterns

The antenna is constructed out of a length of WR-28 waveguide [33], with specifications presented in Table 3.4. Square WR-28 flanges (QuinStar QFF-AB599) [33] are soldered onto the waveguide to connect to the matched load at the end near slot 110 and the mixer at the end near slot 1.

Table 3.4: QuinStar QWR-A20000 Waveguide Specifications

Parameter	Value	Parameter	Value
Inner Broad Wall	7.112mm	Inner Narrow Wall	3.556mm
Outer Broad Wall	9.144mm	Outer Narrow Wall	5.588mm

The antenna is connected to waveguide to 2.4mm coaxial adapters (QWA-28S24F) [33] to perform measurements on a network analyser [43], as depicted in Figure 3.10, with far-field measurements described in Section 3.4. The antenna is well matched over the frequency range, with a passband response of $S_{11} < 20$dB.
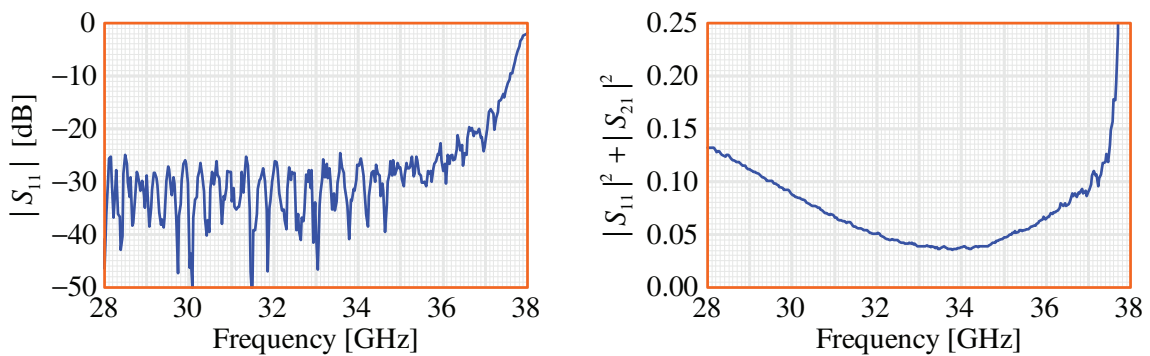
Figure 3.10: Measured Antenna Response

3.3 Reflector

While the size of the UAV precludes any form of optical or mechanical beam forming or scanning it is required for testing purposes to use an antenna with a smaller beamwidth. For this purpose, an optical reflector is designed to focus the antenna pattern along the plane of the flight path as well, resulting in a $1° \times 1°$ main beam. A second configuration to form a slightly blurred $1° \times 5°$ main beam is also designed to test the image reconstruction process for an intermediate step between the ideal case and the final design.

The cross-section of the reflector determines the existence of a focal region of the incident waves [44, 37], as depicted in Figure 3.11. Corner cross-sections have no focal point, with the reflected wave directed back in the direction of the incident wave. Spherical cross-sections have paraxial focal points, with the height of the focal point dependent on the offset of the incident wave to the centre of the reflector. Parabolic cross-sections have unique focal points, with all incident wave converging at a singular point.
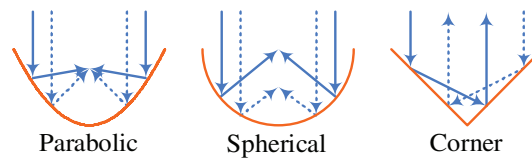
Figure 3.11: Reflector Cross-Section

The shape of the reflector determines the focal region of the incident waves [44, 37], as depicted in Figure 3.12. The circular form of a paraboloid collimates the incident waves into a focal point in the centre of the paraboloid. Paraboloid are designed to work with point sources. The cylindrical form of a parabolic cylinder collimates the incident waves into a focal plane along a line parallel to the axis of the parabolic cylinder. Parabolic cylinders are designed to work with line sources.
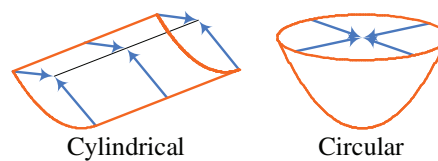
Figure 3.12: Reflector Shape

The feed of the reflector determines the amount of aperture blockage [44, 37], as depicted in Figure 3.13. Offset feeds have the least aperture blockage, but cross-polarisation is introduced due to the asymmetry of the reflector. Back feed is the most compact in being able to obtain a focal length greater than the physical size, but requires a second reflector that causes significant aperture blockage and leads to a complex design. Front feed is normally used being the simplest design and the one-dimensional array causes minimal aperture blockage.
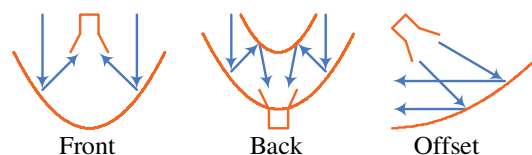
Figure 3.13: Parabolic Reflector Feed Configurations

The reflector for this work is a front-fed, parabolic, cylindrical reflector with surface parallel to the antenna and cross-section surface of $y = \frac{x^2}{4f}$, where f is the focal length and $-\frac{w}{2} \leq x \leq \frac{w}{2}$, as depicted in Figure 3.14. The reflector is constructed out of a copper sheet with thickness of 0.508mm supported by five 50mm ribs water-jet cut out of polystyrene-foam into a parabolic profile. Two further 50mm ribs of polystyrene-foam are placed along the breadth of the reflector to support the antenna at the focal length.
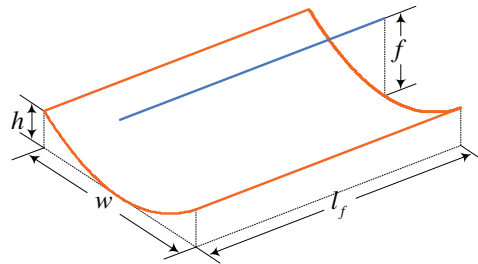
Figure 3.14: Parabolic Cylindrical Reflector

The design specifications of the reflector are presented in Table 3.5. The reflector length is calculated to support the scan angle θ_L to θ_H of the antenna, the reflector width and height and the focal length are calculated to obtain the desired 3dB beamwidth and spill-over of the main beam for the two test configurations and the amount of absorbing material required to absorb the cross polarisation is calculated, with the positioning of the support structure of polystyrene-foam calculated to prevent aperture blockage.

Table 3.5: Parabolic Cylindrical Reflector Specifications

Parameter	Value
Scan Angle (θ_L to θ_H)	25° to 2°
3dB Beamwidth	1°/5°
Cross Polarisation Suppression	20dB

The focal length and the reflector width required to obtain the desired 3dB beamwidth is determined using EMSS FEKO [45] simulations of the reflector and antenna at 33GHz based on the CST MWS [42] simulations of the antenna. With the focal length set at 225mm, a 3dB beamwidth of 1° is obtained with a reflector width of 625mm and a 3dB beamwidth of 5° is obtained with a reflector width of 87.5mm, as depicted in Figure 3.15.
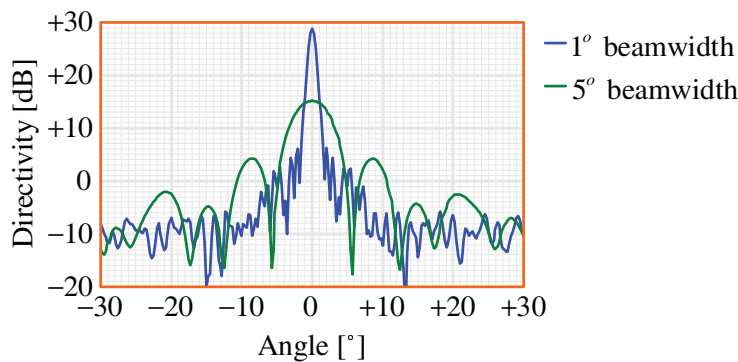
Figure 3.15: Reflector Directivity for Different Beamwidth

To mimimise costs and set-up time, it is desirable to use a singular reflector to obtain the two 3dB beam-widths. The 3dB beamwidth of $1°$ is obtained using a copper sheet with width of 672.1mm folded to a parabolic profile and the 3dB beamwidth of $5°$ is obtained by covering the outer regions of the copper sheet with absorbing material [46], with specifications presented in Table 3.6.

Table 3.6: Eccosorb HR-10 Absorber Specifications

Parameter	Value
Thickness (t_a)	10mm
Frequency Range	12GHz to 70GHz
Reflectivity	$20dB_{min}$

The scan angle of the main beam sweeps from $\theta_H \approx 0°$ at the high end of the frequency range to $\theta_L \approx 30°$ at the low end of the frequency range in the feed direction. The reflector covers the area below the antenna and the area extending $f \tan\theta = 130$mm on the feed end, with a total length l_f of 645.6mm, as depicted in Figure 3.16. The support structure is spaced a further $f \tan\theta = 130$mm on the feed end to prevent blockage.
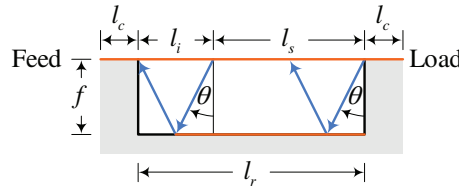
Figure 3.16: Parabolic Reflector Length

The orientation of the antenna pattern is controlled by the angle of the slots, but this tilting introduces cross-polarisation components in the antenna pattern. The cross-polarisation is minimised in the antenna design by alternating the direction of tilt, but total cancellation of cross-polarisation is not possible because the amplitude taper of the array changes the amplitude from element to element and the fields do not cancel [37].

The scan angle of the cross-polarised field sweeps from $\theta_L \approx 45°$ at the low end of the frequency range to $\theta_H \approx 55°$ at the high end of the frequency range in the load direction. Because the cross-polarised field is directed in the opposite direction as the main beam, it can be removed without affecting the main beam by simply attaching absorbing material to the support structure on the load side of antenna, as depicted in Figure 3.17, with the height h of the absorber of $\frac{l_s}{\tan\theta} - f = 291$mm.
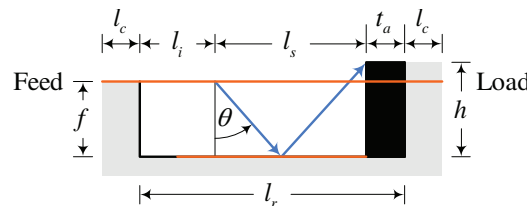
Figure 3.17: Parabolic Reflector Absorber Height

The antenna is positioned in the centre of the parabola and clamped in place using a Perspex section and nylon nuts and bolts. Technical drawings of the antenna and reflector are shown in Appendix A.2.

3.4 Measurements

Measurements of the radiation characteristics of the antenna play a significant role in this work. Obviously the ability of the antenna to couple MMW emissions to the rest of the system must be verified, but more importantly these measurements are required by the image reconstruction algorithm to reconstruct the target area from the blurred images.

The space surrounding an antenna is divided into regions according to field structure, as depicted in Figure 3.18. In the reactive near-field region the reactive field predominates. In the radiating near-field region, or Fresnel region, radiating fields predominate with the angular field distribution dependent upon the distance from the antenna. In the far-field region, or Fraunhofer region, radiating fields predominate with the angular field distribution independent of the distance from the antenna.
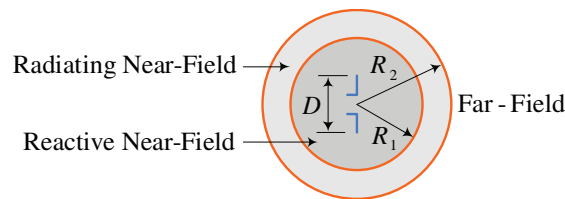
Figure 3.18: Antenna Field Regions

The ideal condition for measuring far-field radiation characteristics is the illumination of the antenna by uniform plane waves. Although this ideal condition is not achievable, it can be approximated by separating the antenna from the illumination source by a distance $r > R_2$. At large radii the curvature of the spherical phase front produced by the source antenna is small over the antenna aperture, where the maximum phase error of the incident field from an ideal plane wave is about $22.5°$ when the distance $r = R_2$.

While there are no abrupt changes in the field configurations as the boundaries are crossed, the established criteria used to separate the regions are

$$
\begin{aligned}
R_1 &= 0.62\sqrt{D^3/\lambda} \\
R_2 &= 2D^2/\lambda
\end{aligned}
\tag{3.4.1}
$$

where D is the largest dimension of the antenna aperture. The maximum values for the boundaries for both antenna configurations, with and without reflector, are obtained at $f = 37\,\text{GHz}$ and are presented in Table 3.7.

Table 3.7: Boundaries of Field Regions of Antenna

Configuration	D	R_1	R_2
With Reflector	625mm	3.4m	96.4m
Without Reflector	515.6mm	2.5m	65.6m

At such large distances it becomes difficult to keep unwanted reflections from the ground and the surrounding objects below acceptable levels. In using a frequency-scanned array the time required to measure the necessary characteristics is extensive. Outdoor ranges are not protected from environmental conditions and do not possess all-weather capabilities. These shortcomings are overcome by using special techniques such as far-field pattern prediction from near-field measurements.

3.4.1 Near-Field Measurements

To provide a controlled environment and to minimise electromagnetic interference measurements are made in the near-field in anechoic chambers with walls covered with absorbing material. The reduced distance results in time and cost effective measurements. Fourier transform methods are used to compute the far-field radiation characteristics from these measurements that are as accurate as those measured in a far-field range [47].

The magnitude and phase distributions of the tangential electric field components radiated by the antenna are measured at regular intervals by a field probe over a planar surface in the near-field. The sampled data is used to determine the amplitude and phase of an angular spectrum of plane waves by using the principle of modal expansion [36]. By expressing the total field of the antenna in terms of a modal expansion the field at any distance can be calculated. Solving for the fields at an infinite distance results in the far-field pattern.

The antenna is aligned with its maximum radiation along the z axis, while a mechanical controller scans a probe at a distance $z_0 = 50\text{mm} > 3\lambda$ from the antenna over the planar surface, where $3\lambda = 31\text{mm}$ at 29GHz places the probe outside of the reactive near-field region of the antenna. The $a \times b$ planar surface is divided into a rectangular grid of $M \times N$ points spaced Δx and Δy apart, as depicted in Figure 3.19. The Nyquist sampling criterion of $\Delta x, \Delta y < \lambda/2$ is satisfied by setting both Δx and Δy to 3mm, where $\lambda/2 = 4.05\text{mm}$ at $f = 37\text{GHz}$.
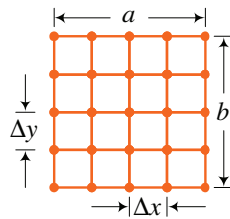
Figure 3.19: Near-Field Planar Measurement Surface

The measurement plane parameters for the both antenna configurations are presented in Table 3.8.

Table 3.8: Measurement Surface Parameters

Configuration	a	b	M	N
With Reflector	996mm	876mm	333	293
Without Reflector	816mm	300mm	273	101

The probe is a 95mm section of open-ended WR28 waveguide [33], with specifications presented in Table 3.4. Both co-polarisation and cross-polarisation measurements are acquired by rotating the waveguide probe 90° about its longitudinal axis. The orientation of the probe to the antenna changes as the probe location varies, as depicted in Figure 3.20. Probe compensation methods couple the far-field of the antenna to those of the measuring probe to compensate for the directivity and polarisation of the probe.
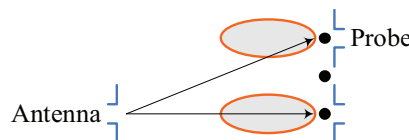
Figure 3.20: Probe Compensation of Near-Field Measurements

The probe measures the field radiated by the antenna in the plane $z = 0$, as depicted in Figure 3.21. In the source free region, where $z > 0$, the field $\mathbf{E}(x, y, z)$ of a monochromatic wave radiated by the antenna is written as a superposition of plane waves of the form $\mathbf{f}(k_x, k_y) \exp(-j\mathbf{k} \cdot \mathbf{r})$ with different amplitudes travelling in different directions but of the same frequency. The objective of the plane wave expansion is to determine the unknown amplitudes $\mathbf{f}(k_x, k_y)$ and direction of propagation of the plane waves.
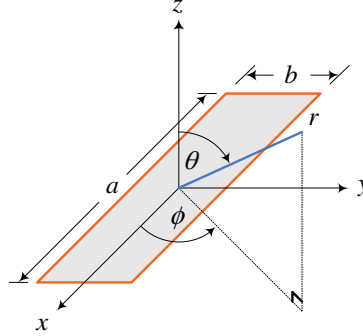
Figure 3.21: Near-Field Measurement Region

The field $\mathbf{E}(x, y, z)$ is written as

$$\mathbf{E}(x, y, z) = \frac{1}{4\pi^2} \int_{-\infty}^{+\infty} \int_{-\infty}^{+\infty} \mathbf{f}(k_x, k_y) \exp(-j\mathbf{k} \cdot \mathbf{r}) \, dk_x dk_y \tag{3.4.2}$$

or

$$\mathbf{E}(x, y, z) = \frac{1}{4\pi^2} \int_{-\infty}^{+\infty} \int_{-\infty}^{+\infty} \mathscr{E}(k_x, k_y, z) \exp[-j(k_x x + k_y y)] \, dk_x dk_y \tag{3.4.3}$$

with transform field $\mathscr{E}(k_x, k_y, z)$

$$\mathscr{E}(k_x, k_y, z) = \int_{-\infty}^{+\infty} \int_{-\infty}^{+\infty} \mathbf{E}(x, y, z) \exp[+j(k_x x + k_y y)] \, dx dy \tag{3.4.4}$$

where

$$\begin{aligned}
\mathscr{E}(k_x, k_y, z) &= \mathbf{f}(k_x, k_y) \exp(-jk_z z) \\
\mathbf{f}(k_x, k_y) &= \hat{\mathbf{a}}_x f_x(k_x, k_y) + \hat{\mathbf{a}}_y f_y(k_x, k_y) + \hat{\mathbf{a}}_z f_z(k_x, k_y) \\
\mathbf{k} &= \hat{\mathbf{a}}_x k_x + \hat{\mathbf{a}}_y k_y + \hat{\mathbf{a}}_z k_z \\
\mathbf{r} &= \hat{\mathbf{a}}_x x + \hat{\mathbf{a}}_y y + \hat{\mathbf{a}}_z z
\end{aligned} \tag{3.4.5}$$

where $k_x = k \sin\theta \cos\phi$, $k_y = k \sin\theta \sin\phi$ and $k_z = k \cos\theta$ are the spectral frequencies that extend over the entire frequency spectrum, $k = 2\pi/\lambda$ is the free-space wavenumber, $\mathbf{k}$ is the vector wavenumber and $\mathbf{r}$ is the position vector.

In making measurements at $z = 0$ the transform field $\mathscr{E}(k_x, k_y, z)$ reduces to $\mathscr{E}(k_x, k_y, z = 0) = \mathbf{f}(k_x, k_y)$ and the tangential components f_x and f_y of the plane wave spectrum $\mathbf{f}(k_x, k_y)$ are obtained from these measurements

$$\begin{aligned}
f_x(k_x, k_y) &= \int_{-b/2}^{+b/2} \int_{-a/2}^{+a/2} E_{xa}(x', y', z' = 0) \exp[+j(k_x x' + k_y y')] \, dx' dy' \\
f_y(k_x, k_y) &= \int_{-b/2}^{+b/2} \int_{-a/2}^{+a/2} E_{ya}(x', y', z' = 0) \exp[+j(k_x x' + k_y y')] \, dx' dy'
\end{aligned} \tag{3.4.6}$$

where E_{xa} is measured by the horizontally-polarised probe and E_{ya} is measure by the vertically-polarised probe.

The parallel component f_z of the plane wave spectrum $\mathbf{f}(k_x, k_y)$ is obtained by manipulating the solenoidal nature of the field $\mathbf{E}(x, y, z)$, $\nabla \cdot \mathbf{E}(x, y, z) = 0$

$$f_z = -\frac{f_x k_x + f_y k_y}{k_z} \tag{3.4.7}$$

The three components E_x, E_y and E_z of the field $\mathbf{E}(x,y,z)$ can be obtained at any distance $z > 0$

$$
\begin{aligned}
E_x(x,y,z) &= \int_{-\infty}^{+\infty}\int_{-\infty}^{+\infty} f_x(k_x,k_y)\exp\left[-j(k_x x + k_y y + k_z z)\right]dk_x dk_y \\
E_y(x,y,z) &= \int_{-\infty}^{+\infty}\int_{-\infty}^{+\infty} f_y(k_x,k_y)\exp\left[-j(k_x x + k_y y + k_z z)\right]dk_x dk_y \\
E_z(x,y,z) &= \int_{-\infty}^{+\infty}\int_{-\infty}^{+\infty} f_z(k_x,k_y)\exp\left[-j(k_x x + k_y y + k_z z)\right]dk_x dk_y
\end{aligned}
\tag{3.4.8}
$$

The far-field radiation characteristics are obtained by solving the field $\mathbf{E}(x,y,z)$ for a distance $z \to \infty$ in Cartesian form

$$
\begin{aligned}
E_x(x,y,z) &= j\frac{k\exp(-jkr)}{2\pi r} f_x \cos\theta \\
E_y(x,y,z) &= j\frac{k\exp(-jkr)}{2\pi r} f_y \cos\theta \\
E_z(x,y,z) &= j\frac{k\exp(-jkr)}{2\pi r}\left(-f_x \sin\theta\cos\phi - f_x \sin\theta\sin\phi\right)
\end{aligned}
\tag{3.4.9}
$$

and in spherical form

$$
\begin{aligned}
E_\theta(r,\theta,\phi) &= j\frac{k\exp(-jkr)}{2\pi r}\left(f_x \cos\phi + f_y \sin\phi\right) \\
E_\phi(r,\theta,\phi) &= j\frac{k\exp(-jkr)}{2\pi r}\cos\theta\left(-f_x \sin\phi + f_y \cos\phi\right)
\end{aligned}
\tag{3.4.10}
$$

3.4.2 Far-Field Computations

A network analyser [48] is used to measure the magnitude and phase of the transmission between the antenna and the probe. The analyser is initialised with a through calibration performed between waveguide flanges, which takes into account the cables from the analyser to the antenna and the probe and the waveguide to 2.4mm coaxial adapters (QWA-28S24F) [33] used to connect the antenna and the probe to the cables. The measurements are performed with an averaging factor of 256.

The tangential field components E_{xa} and E_{ya} are recorded over the aperture at grid points with spacings of $\Delta x = \frac{\pi}{k_{xo}}$ and $\Delta y = \frac{\pi}{k_{yo}}$, where k_{xo} and k_{yo} are real numbers that represent the largest magnitudes of k_x and k_y so $\mathbf{f}(k_x,k_y) \simeq 0$ for $|k_x| > k_{xo}$ or $|k_y| > k_{yo}$. The tangential components f_x and f_y of the plane wave spectrum are obtained by performing a discrete Fourier transform algorithm at the set of wavenumbers explicitly defined by

$$
\begin{aligned}
k_x &= \frac{2m\pi}{M\Delta x}, & -\frac{M}{2} \le m \le \frac{M}{2}-1 \\
k_y &= \frac{2n\pi}{N\Delta y}, & -\frac{N}{2} \le n \le \frac{N}{2}-1 \\
k_z &= \begin{cases} \sqrt{k^2-\left(k_x^2+k_y^2\right)}, & k^2 \ge k_x^2+k_y^2 \\ -j\sqrt{\left(k_x^2+k_y^2\right)-k^2}, & k^2 < k_x^2+k_y^2 \end{cases}
\end{aligned}
\tag{3.4.11}
$$

where the $k^2 \ge k_x^2+k_y^2$ form of k_z contributes to the propagating waves and the $k^2 < k_x^2+k_y^2$ form contributes to the evanescent waves.

The resolution of the far-field pattern is determined by the number of wavenumber spectrum points, which are equal to the number of points in the near-field distribution. However, the resolution of the far-field pattern is not improved by decreasing the sampling spacing to increase the number of the near-field sample points as the decreased sample spacing will increase the limits of the wavenumber spectrum points, which are in the large evanescent mode region and do not contribute to improved resolution of the far-field pattern.

An improvement to the resolution of the far-field pattern is obtained by artificially adding data sampling points with zero value at the outer extremities of the near-field distribution. This artificially increases the number of sample points without decreasing the sample spacing. As the sample spacing remains fixed the limits of the wavenumber spectrum points remain fixed. With the additional wavenumber spectrum points within the original wavenumber limits the resolution in the computed far-field patterns is improved.

The near-field measurements of the three configurations of the antenna are transformed to far-field patterns at a planar surface at a fixed distance away from the antenna, with the orientation of the main beam of the antenna pattern as a function of frequency depicted in Figure 3.22. There is a near-perfect comparison between the theoretical values and the computations, with good comparison with the CST MWS simulations.
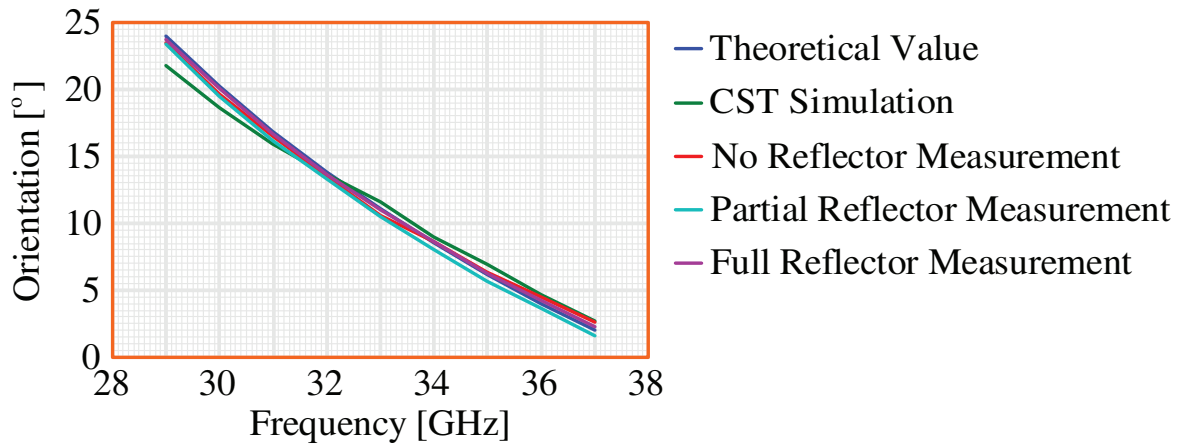
Figure 3.22: Computed and Measured Orientation of Main Beam of Far-Field Pattern

The 2D far-field patterns for these three configurations are depicted in Figure 3.23, Figure 3.24 and Figure 3.25. For all three configurations the narrow, high gain, frequency-scanned beam along the plane perpendicular to the flight path is clearly displayed. In the configuration of the antenna without a reflector the very broad beam along the plane of the flight path, as well as the large sidelobe, is evident.
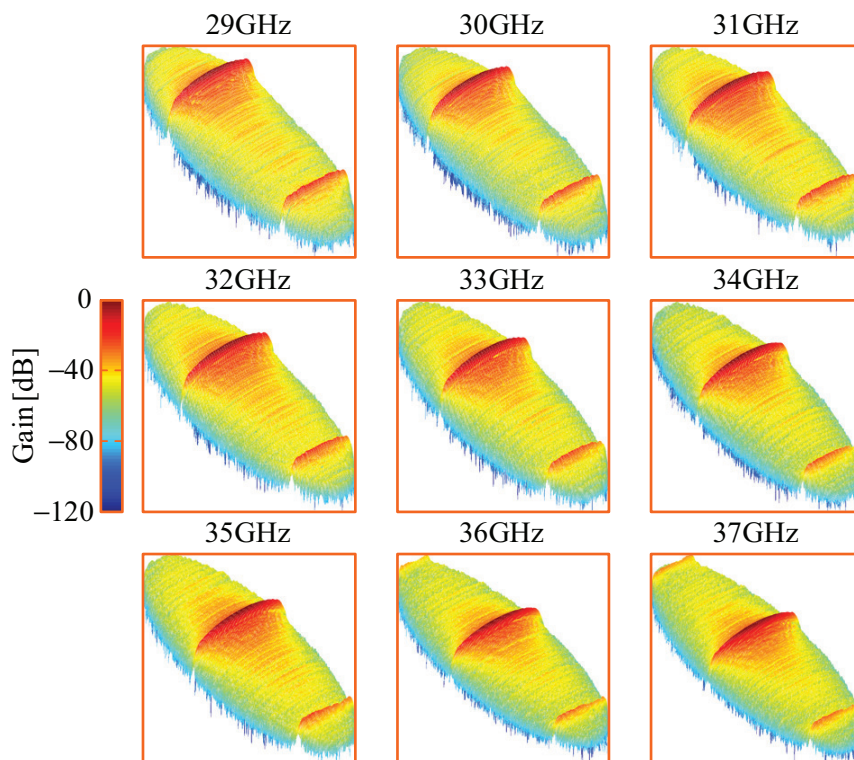
Figure 3.23: Computed Far-Field Patterns of Antenna without Reflector
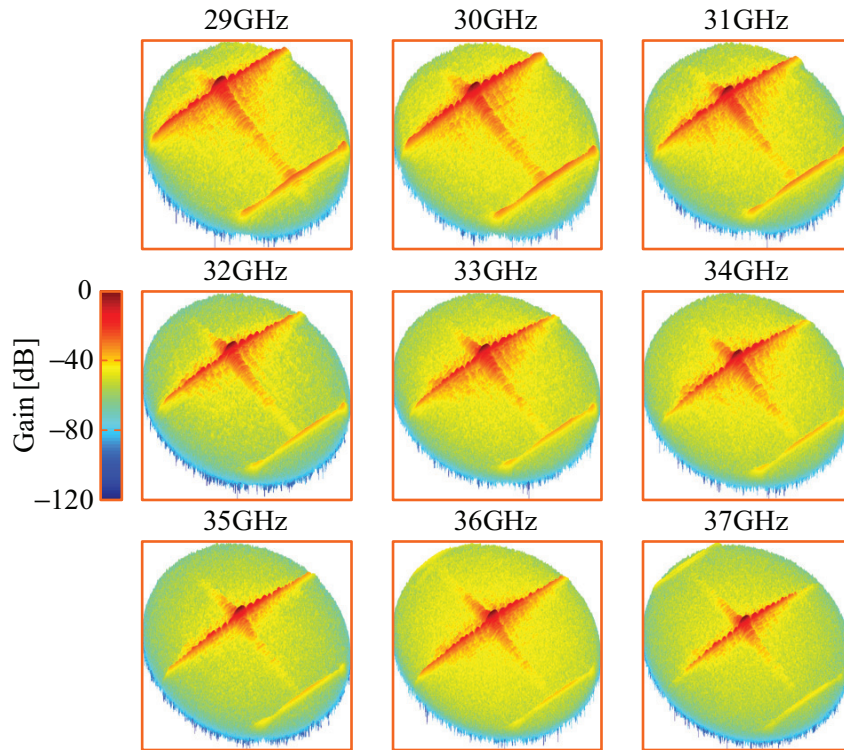
Figure 3.24: Computed Far-Field Patterns of Antenna with Partial Reflector

In the configuration of the antenna with a reflector the focusing effect of the reflector on the main beam, as well as on the sidelobe, is evident.
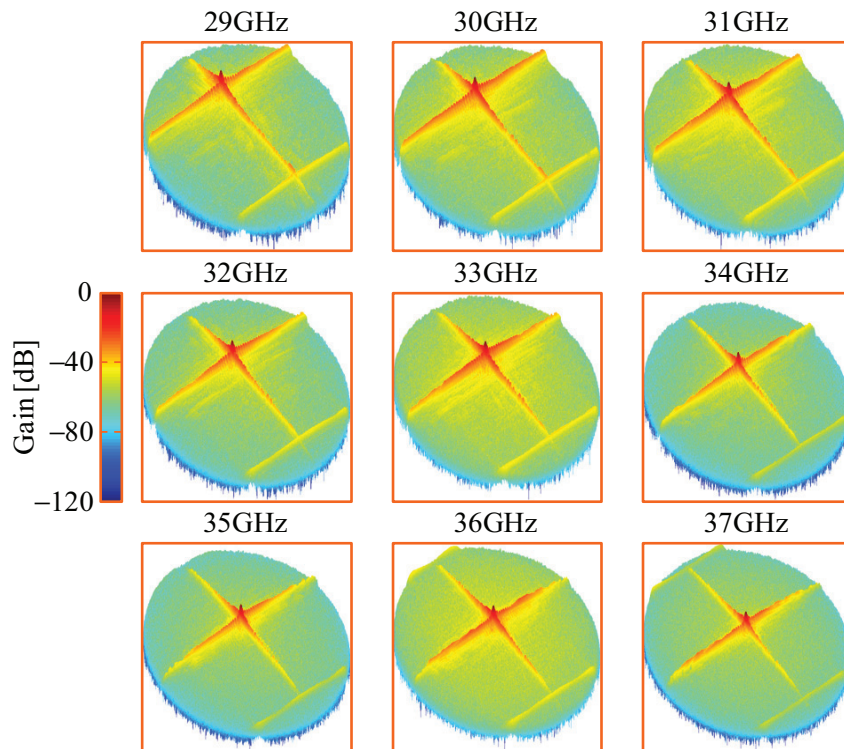
Figure 3.25: Computed Far-Field Patterns of Antenna with Full Reflector

3.4.3 Near-Field Computations

From the figures within Section 3.4.2 it is evident that the configuration of the antenna with a full reflector can be used directly to form focused images of a target area. However, to form images from measurements taken using the configurations of the antenna with a partial reflector and without a reflector would required the measured data to first pass through a post processor.

While still in the initial stages of the development of the system a controlled target area is used to test the post processor. As the start of the far-field region of the antenna is approximately 100m from the antenna, it is virtually impossible to set-up a controlled environment around the antenna at such a large distance, and this is why the far-field characteristics of the antenna are computed from measurements taken in the near-field.

A main obstacle associated with far-field measurements of antennae with beam-scanning functionality is that the measurement device has to cover a large two-dimensional grid at the large distance away from the antenna. These measurements would required a large amount of precision machinery to position the measurement device and would take a long time to perform. By reducing the space between the antenna and the device, the grid that the device traverses is significantly reduced, which leads to a saving in machinery, time and cost.

A similar strategy is followed to perform measurements of the imaging system within the controlled environment of an anechoic chamber. In order for this to be a valid test of the imaging system, the spacing between the source and the antenna must be sufficiently large enough for the far-field characteristics of the antenna pattern to start forming. In other words, the main beam of the antenna pattern must sweep the target area as a function of frequency, even if the expected orientation or directivity of the far-field is not yet formed.

The near-field measurements described in Section 3.4.1 are used to compute the antenna patterns at a distance $z = 2.5$m from the antenna. The tangential components f_x and f_y of the plane wave spectrum are computed from the near-field measurements using Equation 3.4.6 and the parallel component f_z of the plane wave spectrum is computed using Equation 3.4.7. The parallel component is required because the measurement plane is displaced 2.5m along the z-axis. Finally, the fields at $z = 2.5$m are computed using Equation 3.4.8.

While this might sound trivial, a few key manipulations of the data is required to obtain the correct antenna pattern. The following applies to MATLAB [49], and differs from application to application. These manipulations only rearrange the indexing of the values within the matrices to synchronise the measurement plane of the near-field measurements with the algorithms of MATLAB, with no adjustments to the values within the matrices.

The discrete Fourier transforms function with their centre frequency at the first cell of the matrices and the rest of the cells at frequencies greater than the centre frequency, while the near-field measurements were performed over a grid centred around the antenna, with the centre of the matrix at the centre frequency and the other cells at frequencies above and below the centre frequency, as depicted in Figure 3.26. Therefore, matrix transformations shift the measurement plane data to the input expected by the transform algorithms.
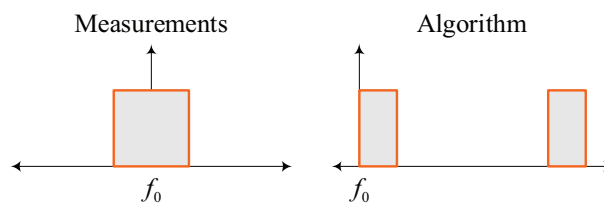
Figure 3.26: Synchronisation between Measurement Data and Transform Algorithms

Secondly, the resolution of the fields is improved by artificially adding zeros to the extremities of the measured data before being passed to the transform algorithms. This too needs matrix transformations to synchronise the input expected by the transform algorithm and the measurements, as depicted in Figure 3.27.
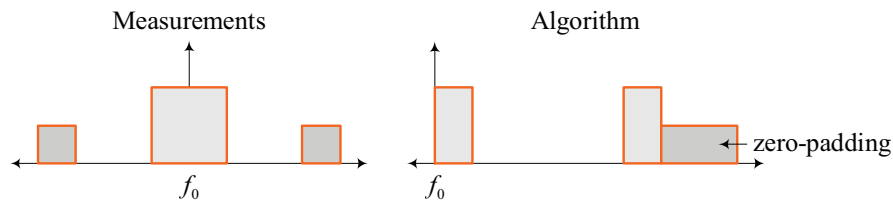
Figure 3.27: Synchronisation between Zero-Padding and Transform Algorithms

The built-in function of the transform algorithm would zero-pad the input data by extending the input matrix size at cell locations at the greatest distance from the centre frequency of the transforms, being the first cell, which leads to the wrong computation. Instead, the padding should be done by extending the input matrix size at cell locations at the greatest distance from the centre frequency of the measured data. Only then should this matrix be transformed to the expected input arrangement of the transform algorithm.

Thirdly, a large amount of zero-padding is required to ensure that the main beam of the antenna pattern is in the measurement plane. The orientation of the main beam of the antenna pattern at 29GHz is 24.0°, which is 1.1m away the centroid of the antenna. As the near-field measurement plane only extends 0.5m in any direction, by zero-padding the measurements, the measurement plane is extended along the *xy*-plane and the main beam of the 29GHz antenna pattern is placed in the measurement plane, as depicted in Figure 3.28.
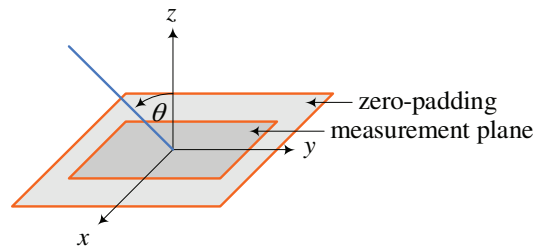
Figure 3.28: Zero-Padding to Position Main Beam within Measurement

Using the described strategy the near-field measurements of the full reflector antenna configuration are transformed to fields at a distance of 2.5m. This is the maximum distance that the source can be displaced from the antenna whereby the orientation of the 29GHz main beam is still bound within the physical confines of the anechoic chamber. The near-field measurement plane matrices are zero-padded to form matrices 64 times larger than the originals to ensure that the scan angle of antenna pattern is within the measurement plane.

The 2D far-field patterns for the antenna configuration with the full reflector is depicted in Figure 3.29. While the expected frequency scan is clearly seen, as well as the focus of the main beam of the antenna pattern in both direction due to being connected to the reflector, the fields have not propagated a sufficient distance to form the high gain beam of the computed far-field patterns described in Section 3.4.2. However, the fields are sufficiently formed at 2.5m to test the ability of the system at the multiplexer stage in Chapter 5, as well as to validate the simulated target areas used to test the post-processor in Chapter 6.
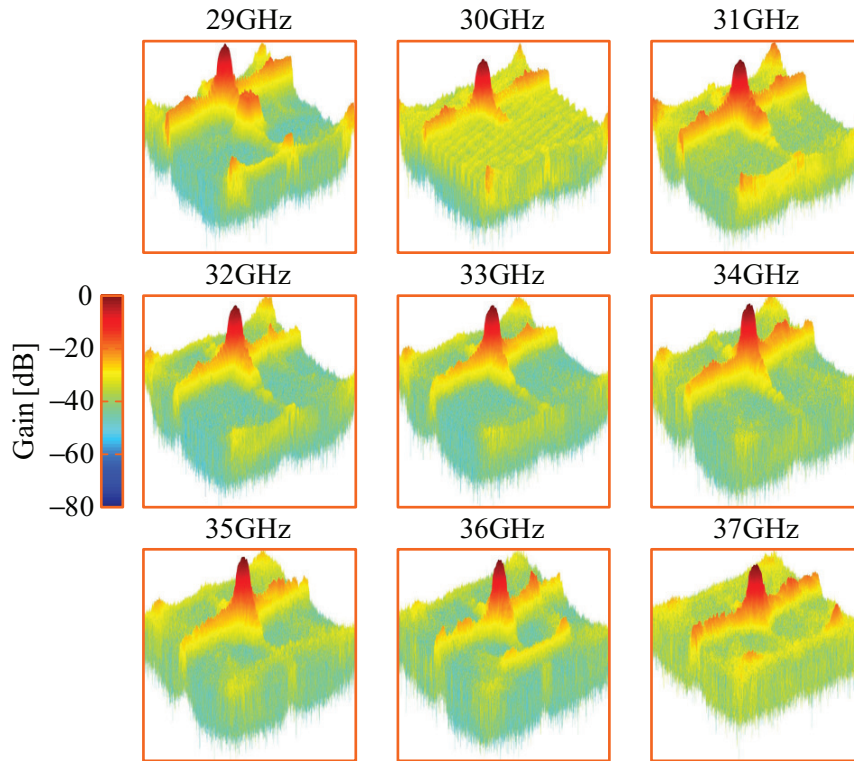
Figure 3.29: Computed Near-Field Patterns of Antenna with Full Reflector

3.4.4   Far-Field Measurements

The antenna has a narrow, high gain, frequency-scanned beam along the plane perpendicular to the flight path, but a very broad beam along the plane of the flight path blurs the image, making it difficult to accurately determine the position of an object or to differentiate between objects situated along the plane of the flight path.

While the size of the UAV precludes optical and mechanical scanning, the ability of the antenna to capture MMW emissions is tested by attaching the antenna to a reflector that focuses the antenna pattern along the plane of the flight path, resulting in a beam with 3dB beamwidth of $1° \times 1°$. The system is depicted in Figure 3.30, with the Low-Noise Amplifier (LNA), Local Oscillator (LO) and mixer seen at the right of the image.
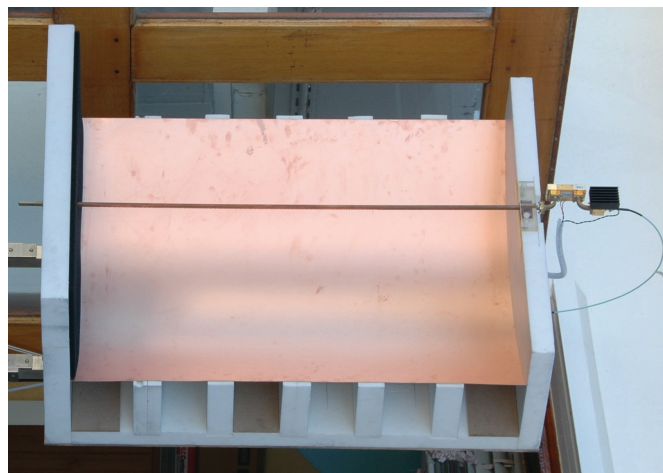
Figure 3.30: Antenna with Reflector Set-Up

The reflector is attached to a rotator on the roof of the Engineering Faculty of Stellenbosch University to take measurements of the surrounding mountains, as depicted in Figure 3.31. The captured MMW emissions over the whole frequency range are measured by a spectrum analyser [50].

Figure 3.31: Far-Field Measurement Set-Up

Optical and MMW images were taken of a mountainside in clear weather during the day and at night, as depicted in Figure 3.32. While there is a sharp contrast in the optical images, with a flash required for the night image, the sun's illumination is not essential to the MMW images as there is great similarity in the MMW images. The increase in sky illumination from the zenith to the horizon is evident within the MMW images.
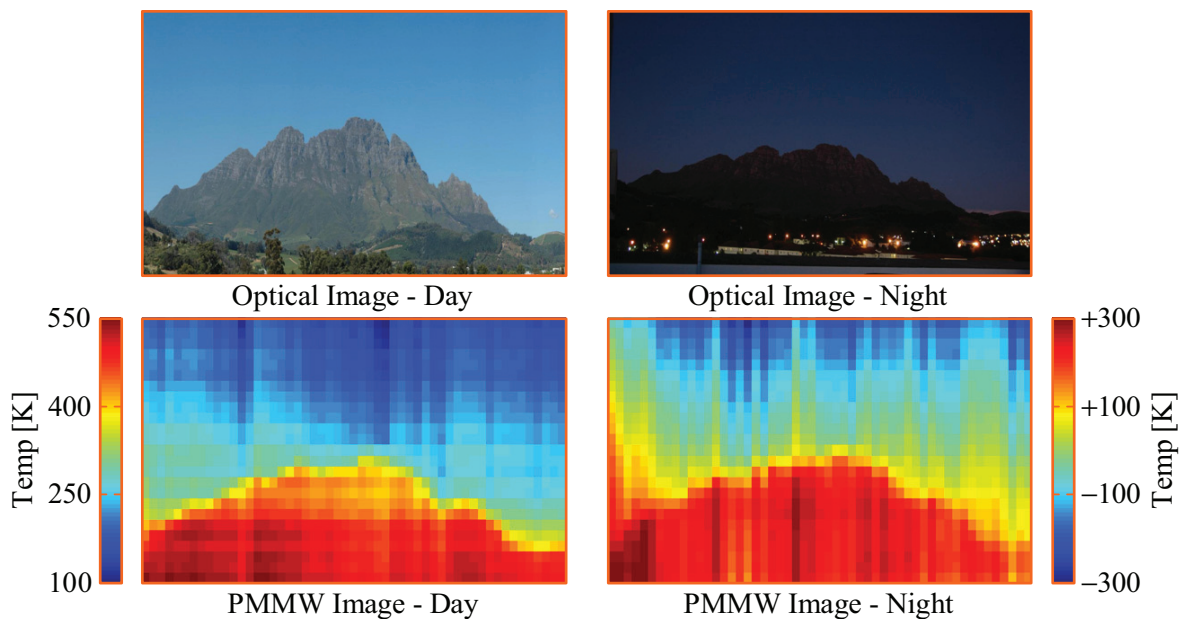
Figure 3.32: Comparison of MMW Images and Optical Images under Different Visibility Conditions

3.5   Conclusion

In this chapter the antenna design is described. The UAV places severe restrictions on the possible implementations, with no form of mechanical or optical technique a viable option. The chosen design is a a slotted-waveguide array that scans along the plane perpendicular to the flight of the UAV as a function of frequency and uses the flight of the UAV to expand the FOV into a two-dimensional target area.

Owing to the linear structure of the antenna, the antenna pattern has a very broad beam along the plane of the flight path that cannot be focused using a lens, mirror or reflector because these components are too large to be fitted under the wing of a small UAV. Therefore, the measurements made in this chapter are used by the post processor described in Chapter 6 to reconstruct an image of the target area.

However, in order to test the ability of the antenna to couple MMW emissions to the rest of the system, a reflector is designed that focuses the antenna pattern along the plane of the flight path as well. From the far-field measurements of the antenna, it can be seen that the antenna is able to capture incident MMW emissions that are consistent between favourable and poor visibility conditions.

Chapter 4

Multiplexer

4.1 Introduction

When using a frequency-scanned array for the antenna the captured Millimetre-Wave (MMW) emissions have to be split up into different frequency bands before detection to use the space-to-frequency mapping property of the antenna to form the images. This is done by means of a multiplexer following the second Intermediate Frequency (IF) amplifier, with each channel terminated in a detector, as depicted in Figure 4.1.
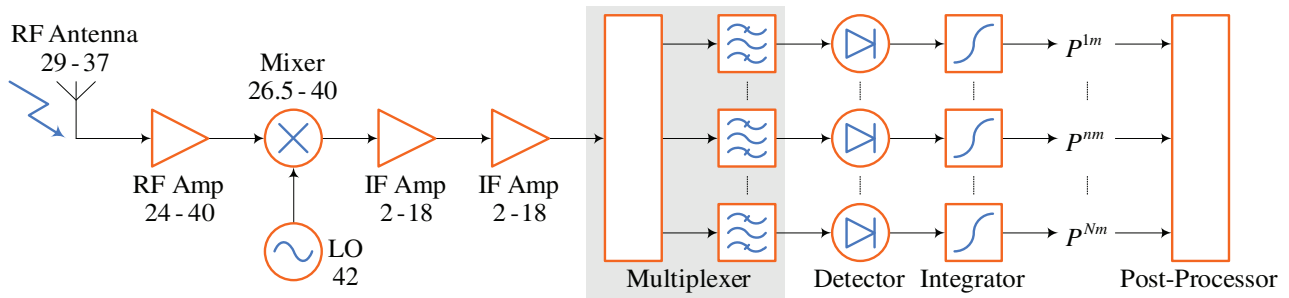
Figure 4.1: Radiometer with Multiplexer Stage Highlighted

The image is built up line by line as the antenna concurrently scans the target area along the plane perpendicular to the flight path, with each orientation θ_0^m scanned by a beam centred at frequency f_0^m. The multiplexer divides the frequency range f_L to f_H into M equal-sized contiguous bandwidths B of size $\frac{f_H - f_L}{M}$ each assigned to a different pixel column P^m separating the target area into bands. The image resolution is equivalent to the number of channels the multiplexer is able to support.

In covering a frequency range of 1.6 octaves at the IF range the bandwidth of the multiplexer is too wide for a waveguide solution, thereby limiting the design to realisation in microstrip or stripline. A stripline design is chosen, with a transition from the SMA connector output of the second IF amplifier, as it is a compact solution well suited to work with the available space on the Unmanned Aerial Vehicle (UAV).

Due to the wide bandwidth of the multiplexer, the harmonic passbands of the bandpass filters in the lower half of the frequency range overlap with the passbands of the bandpass filters in the upper half of the frequency range. To solve this problem a bandpass filter is incorporated in the multiplexer design to suppress the higher-order passbands of the bandpass filters in the lower half of the frequency range.

4.2   Multiplexer Overview

The role of the multiplexer is to separate the wideband signal at the common port into individual channels, with each channel isolated from the other channels. The stopband response of the reflection of filters is a susceptance that varies with frequency that will seriously affect the performance of closely-spaced filters. Various multiplexer solutions that minimise this effect exist in the literature, with a short summary given here.

The simplest design to obtain M channels is to continually split the common port frequency band in half in $\log_2(M)$ stages using $M-1$ diplexers, as depicted in Figure 4.2. As contiguous channels of moderate bandwidth are required, the $M-1$ filter pairs of the diplexers are designed using the methods described in [51, 52] to minimise the effects of the input admittance of a filter in the stopband of the complementary filter.
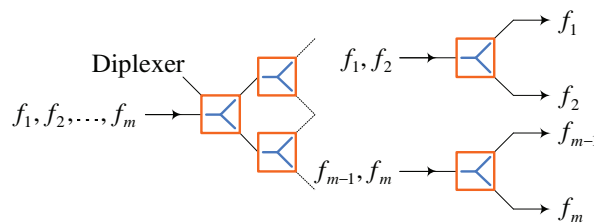
Figure 4.2: Splitter Multiplexer

While simple to design, the splitter multiplexer configuration requires a large number of filters for the desired number of channels and can be more lossy than other configurations due to the path length of the signal through the cascaded stages. In contrast, the channels can all be concurrently connected to the common port, as depicted in Figure 4.3. Only one filter is required per channel, with minimal loss along the path lengths.
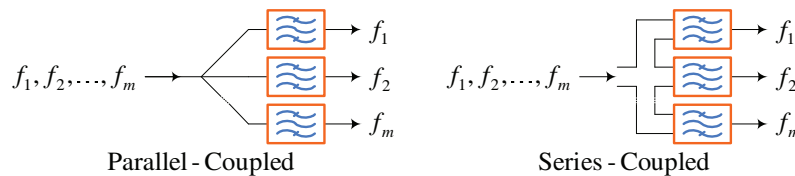
Figure 4.3: Common-Junction Multiplexer

The majority of common-junction multiplexer designs begin with filters individually designed for a given transmission response, with various techniques employed to match these filters to the much larger passband of the multiplexer. The techniques of [53, 54, 55] have been developed for doubly-terminated filters, while the techniques of [56, 57, 58] have been developed for singly-terminated filters.

All these techniques include compensation in the form of formulae developed to modify the filter parameters. In [53] additional compensation is required in the form of dummy channels at frequencies bordering the lower and upper limits of the multiplexer passband. In [56, 58] additional compensation is required in the form of immittance compensation-annulling networks.

The realisation of common-junction multiplexers for a large number of channels is difficult. The parallel-connected configuration suffers from the complexity of connecting M filters in parallel, specifically with regards to the response of the junction at the common port. The series-connected configuration suffers from the complexity of isolating M ground-planes from each other.

The realisation of a multiplexer can be simplified by connecting the channels to the common port in sequential order, as depicted in Figure 4.4. This configuration offers a simple, compact design for a large number of channels, with the main disadvantages the loss in latter channels incurred by travelling down the long transmission path from the common port and the interactions between the channels through the common port.
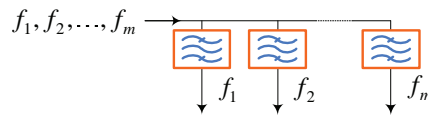
Figure 4.4: Cascade Multiplexer

The use of directional components to minimise the interaction between the channel filters has been investigated [59, 60]. As directional components prevent interaction between channel filters, additional channels can be appended without disrupting the existing multiplexer design. In addition, directional components ease design, assembly and tuning of the multiplexer as each channel is operating in isolation. While active components could provide isolation, only passive devices are investigated to minimise the system's power consumption.

The simplest design is to place a circulator at the connection of each channel to the common port [59, 60], as depicted in Figure 4.5. The channels are isolated from each other in the circulators only allowing incident power to travel in one direction. However, circulators are unable to operate over the whole frequency range and relatively high losses are present in latter channels due to the accumulated insertion loss of the circulators.
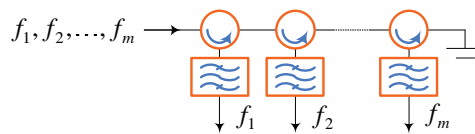
Figure 4.5: Circulator-Coupled Multiplexer

Instead of using circulators, the multiplexer can be formed by connecting directional filters in series [59, 60], as depicted in Figure 4.6. A directional filter is a four-port device, with three of the ports mimicking a circulator connected to a filter and the fourth port terminated in a load. In-band power incident at the common junction port emerges at the channel output port, with the reflected power terminated at the load port. Out-band power incident at the common junction port passes on unimpeded to the subsequent channels.
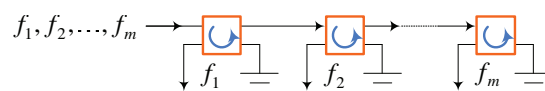
Figure 4.6: Directional-Coupled Multiplexer

In [61] the directional filters are realised in stripline as one-wavelength ring resonators coupled to one another and two transmission lines, with one transmission line connecting the common port to subsequent channels and the other connecting the channel output port to the load port. In [62] the filter parameters are designed to place the cross-over point between adjacent channels at the half-power points. Directional filters are limited to narrow-band applications as it is difficult to realise bandwidths greater than 1%.

Another implementation of passive components that mimics a circulator, yet with wider realisable bandwidths, makes use of two identical filters and two identical 90° hybrids for each channel of the multiplexer [59, 60], as depicted in Figure 4.7. This configuration results in in-band power adding constructively at the channel output, with isolation between channels achieved as out-band power adds destructively.
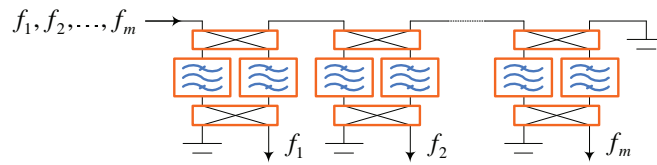
Figure 4.7: Hybrid-Coupled Multiplexer

This configuration is primarily used in high-power applications as the hybrids split the incident power between the two filters, thereby increasing power handling and reducing susceptibility to voltage breakdown. Tight fabrication tolerances are required to minimise phase deviation between the two paths and preserve directivity. The physical size and weight is larger than other approaches because of the duplication of components.

Directional multiplexers are attractive because the channels are isolated from each other, but none meet the requirements for this work. Hybrid-coupled multiplexers are not compact enough, directional-coupled multiplexers and circulator-coupled multiplexers cannot realise the required bandwidth. Therefore for the purposes of this work non-directional components are investigated, wherein the parameters of the multiplexer are designed as a whole to counteract channel interactions as the channels are electrically connected to each other.

The wideband signal of the common port can be selectively split-up using a complementary highpass and lowpass filter pair for each channel, as depicted in Figure 4.8. The highpass filter sets the lower cut-off frequency of the channel, with the lowpass filter setting the upper cut-off frequency of the channel. In [63] the filter parameters of the individual filters are modified so that the resulting passband of the diplexer is optimal.
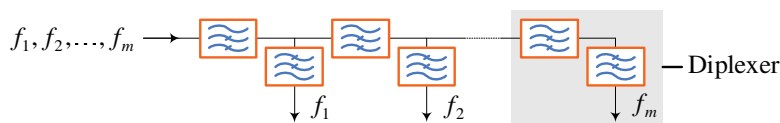
Figure 4.8: Diplexer-Based Multiplexer

As diplexer-based multiplexers do not make use of passband filters there are no higher-order passbands of filters in the lower half of the frequency range to fall within the passbands of filters in the upper half of the frequency range. However, a large number of filters is required for the desired number of channels, resulting in a physically larger design than that of other approaches. Instead the multiplexer can be designed by connecting passband filters sequentially to the common port through a series of junctions, as depicted in Figure 4.9.
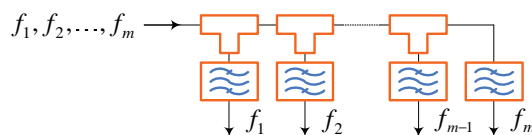
Figure 4.9: Manifold-Coupled Multiplexer

4.3   Multiplexer Design

The manifold-coupled multiplexer is the chosen design for this work because this approach offers an optimum choice with regards to size and insertion loss, with the size further reduced by placing filters on both sides of the manifold. The filters, junctions and spacings between junctions and filters are designed to minimise the interactions between channels, implying that this configuration is not amenable a modular concept and any change in the allocation of channels will require a new multiplexer design.

In [64] formulae modify filter prototypes to properly interact with other filters and function as if operating into a matched termination. However, the total bandwidth and number of channels is limited. With the advent of powerful computational and simulation software, analytical techniques have been superceded by optimisation methods that can combine an arbitrary number of channels, regardless of bandwidths and channel separation, however the implementation becomes more difficult as the number of channels increase.

In [65, 60] the multiplexer is modelled as a cascade of 2-port and 3-port matrices that mimic the desired practical implementation, with the parameters of these models determined using algorithms designed to optimise large systems [66]. The optimisation process is further sped up by initially decreasing the number of parameters by replacing the filters with equivalents network prototypes [67, 68] or fictitious reactive loads that simulate the out-band phase response of the channels [69], before performing a full-wave analysis.

Segmentation techniques minimise the number of parameters that must be handled simultaneously to reduce the optimisation time and avoid local minima traps. In [70, 71] the multiplexer is modelled as a series of diplexers, with the junctions designed to meet certain criteria and the connections between filters and junctions made according to formulae derived for ideal diplexer behaviour at the midband frequencies of the filters [72].

This analytical model is developed on the basis of just fundamental mode interaction between junction and filters. In cases where optimum distances are so short that higher modes may cause interaction, the single mode result is an excellent starting point for an optimisation routine. These criteria are of general application and independent of the technology adopted as the analysis is based on the S-parameters of the junction.

The junction criteria are derived from the properties of the S-parameters of a lossless reciprocal three-port junction with port 1 connected to filter F_1 with passband b_1 located at a distance l_1 away and port 2 connected to filter F_2 with passband b_2 located at a distance l_2 away, as depicted in Figure 4.10. These criteria involve just the S-parameters of the junction, and are independent of the filters and of their spacings from the junction.
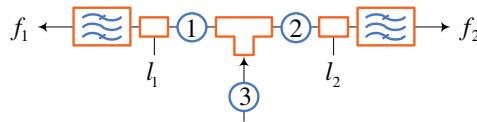
Figure 4.10: Diplexer

When filter F_1 is terminated by a matched load the resulting two-port junction between port 2 and port 3 is

$$\begin{bmatrix} S_{22} & S_{23} \\ S_{23} & S_{33} \end{bmatrix} = \begin{bmatrix} S_{Y22} & S_{Y23} \\ S_{Y23} & S_{Y33} \end{bmatrix} + \left[\frac{1}{S_{F_1 11}\exp(-2j\beta l_1)} - S_{Y11} \right]^{-1} \times \begin{bmatrix} S_{Y12}^2 & S_{Y12}S_{Y13} \\ S_{Y12}S_{Y13} & S_{Y13}^2 \end{bmatrix} \qquad (4.3.1)$$

where S_{Yij} are the S-parameters of the junction, $S_{F_1 11}$ is the reflection coefficient of filter F_1 and β is the propagation constant of the fundamental mode. A similar two-port junction between port 1 and port 3 is obtained when filter F_2 is terminated by a matched load.

The first criterion that must be satisfied ensures that the transmission between port 3 and port 2 over the band b_2 is perfect and that the transmission between port 3 and port 1 over the band b_1 is perfect. This criterion is satisfied when the two-port junction of Equation 4.3.1 is perfectly matched and lossless over the band b_2, and when the two-port junction between port 1 and port 3 is perfectly matched and lossless over the band b_1.

As $S_{22} = 0$ of the two-port junction of Equation 4.3.1 over the band b_2 to meet the first criteria

$$S_{F_1 11} \exp\left(-2j\beta l_1\right) = \frac{S_{Y22}}{S_{Y11}S_{Y22} - S_{Y12}^2} = \frac{S_{Y22}}{\Delta S_Y S_{Y33}^*} \tag{4.3.2}$$

where ΔS_Y is the determinant of port 3 and port 2 of the junction and $S_{Y33}^* = \frac{S_{Y11}S_{Y22} - S_{Y12}^2}{\Delta S_Y}$ because the junction is lossless. This is only true when $|S_{Y22}| = |S_{Y33}|$ over the band b_2, as filter F_1 is in its stopband over band b_2 $|S_{F_1 11}| \approx 1$ over band b_2 and as the junction is lossless $|\Delta S_Y| = 1$. Similarly, $|S_{Y22}| = |S_{Y33}|$ over the band b_1 is required to obtain perfect transmission between port 3 and port 1 over the band b_1.

When symmetrical junctions are used $|S_{Y11}| = |S_{Y22}|$ and the first criteria is obtained, namely that

$$|S_{Y11}| = |S_{Y22}| \cong |S_{Y33}| \tag{4.3.3}$$

over the bands b_1 and b_2.

A second criterion ensures that optimum junction behaviour for the purpose of realising a diplexer is achieved. As the junction is lossless

$$S_{Y33} = \frac{S_{Y13}}{S_{Y13}^*}\left(S_{Y11}^* + S_{Y12}^*\right) = S_{Y11}^* + S_{Y12}^* \tag{4.3.4}$$

where $S_{Y11} = \frac{\Gamma_e + \Gamma_o}{2}$, $S_{Y12} = \frac{\Gamma_e - \Gamma_o}{2}$, Γ_e is the reflection coefficients at port 1 corresponding to an even excitation and Γ_o is the reflection coefficients at port 1 corresponding to an odd excitation.

As $|\Gamma_e| = \left|\frac{\Gamma_e + \Gamma_o}{2}\right|$ over band b_2 to satisfy the first criteria, as the junction is symmetrical the amplitude of the wave transmitted to port 3 in the odd excitation case is 0, hence $|\Gamma_o| = 1$, and because the minimum of S_{Y11} is obtained when Γ_e and Γ_o have opposite phases, the second criteria is obtained, namely that

$$|S_{Y33}| \geq 1/3 \tag{4.3.5}$$

which is different from the criteria required for ideal behaviour as a matched power splitter, where $|S_{Y33}| = 0$.

The third criteria ensures that the maximum bandwidth is achieved for a given reflection ε of the two-port junction of Equation 4.3.1. This criteria is satisfied when $|S_{22}| < \varepsilon$ over the band Δf. By differentiating the reflection coefficient S_{22} of the two-port junction of Equation 4.3.1 with respect to f

$$\frac{d}{df}S_{22} = S_{Y22}' + \frac{2S_{Y12}'S_{Y12}}{\frac{1}{S_{F_1 11}\exp(-2j\beta_2 l_1)} - S_{Y11}} + S_{Y12}^2 \frac{-2j\frac{l_1}{S_{F_1 11}}\exp(+2j\beta_2 l_1) + \frac{S_{F_1 11}'}{S_{F_1 11}^2}\exp(+2j\beta_2 l_1) + S_{Y11}'}{\left(\frac{1}{S_{F_1 11}\exp(-2j\beta_2 l_1)} - S_{Y11}\right)^2} \tag{4.3.6}$$

the maximum bandwidth is obtained when the parameters of the junction do not depend on frequency. This results in the third criteria, namely that

$$S_{Y11}' \cong S_{Y12}' \cong S_{Y22}' \cong 0 \tag{4.3.7}$$

over the bands b_1 and b_2.

The minimum reflection at a given frequency obtained by terminating port 3 on a filter is zero, since $S_{Y11} = S_{Y22}$ at any frequency, provided that the filter is in its outband. Conversely, the minimum reflection obtained by terminating port 2 on a filter is non zero, since $S_{Y11} \neq S_{Y33}$. Therefore, the diplexer performance will be better at the midband frequency of the filter at port 2 than at the midband frequency of the filter at port 3.

The M filters F_i with scattering parameters S_{F_i} and $M-1$ T-junctions with scattering parameters S_Y, where $i = 1, \ldots, M$, are connected as depicted in Figure 4.11. The filters are ordered in such a way that $f_i < f_{i+1}$, where f_i is the midband frequency of F_i.
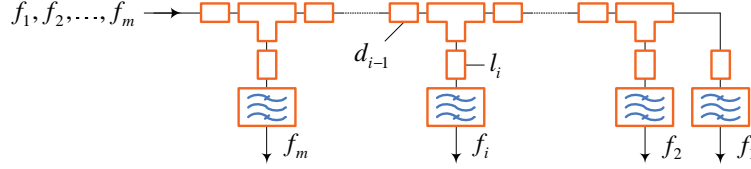
Figure 4.11: Manifold-Coupled Multiplexer Design

The first module, with 3×3 scattering parameters S^1_{jun}, is built by connecting filter F_1 to port 1 of the T-junction at distance l_1 and by by connecting filter F_2 to port 2 of the T-junction at distance l_2

$$
\begin{aligned}
l_1\big|_{f=f_2} &= \tfrac{1}{2j\beta} \ln\left(\frac{S_{Y22}}{\Delta S_Y S^*_{Y33} S_{F_1 11}}\right) \\
l_2\big|_{f=f_1} &= \tfrac{1}{2j\beta} \ln\left(\frac{S_{Y11}}{\Delta S_Y S^*_{Y33} S_{F_2 11}}\right)
\end{aligned}
\tag{4.3.8}
$$

where ΔS_Y is the determinant of S_Y and β is the propagation constant of the fundamental mode.

$N-2$ modules, with 3×3 scattering parameters S^{i-1}_{jun}, are built by connecting filter F_i to port 3 of a T-junction at distance l_i

$$
l_i\big|_{f=f^i_M} = \tfrac{1}{2j\beta} \ln\left(\frac{S_{Y22}}{\Delta S_Y S^*_{Y11} S_{F_i 11}}\right)
\tag{4.3.9}
$$

where

$$
f^i_M = \tfrac{1}{i-1} \sum_{k=1}^{i-1} f_k
\tag{4.3.10}
$$

is the midband frequency of the $(i-1)$ channel multiplexer and $i = 3, \ldots, N$.

The 4-port multiplexer is obtained by connecting port 2 of S^2_{jun} to port 3 of S^1_{jun} at distance d_1

$$
d_1\big|_{f=f_3} = \tfrac{1}{2j\beta} \ln\left(\frac{S_{Y33}}{\Delta S_Y S^*_{Y11} S^1_{33}}\right)
\tag{4.3.11}
$$

where S^1_{33} is the reflection coefficient at port 3 of S^1_{jun}.

The N-port multiplexer is obtained by connecting port 2 of S^{i+1}_{jun} to port 1 of S^i_{jun} at distance d_i

$$
d_i\big|_{f=f_{i+2}} = \tfrac{1}{2j\beta} \ln\left(\frac{S_{Y33}}{\Delta S_Y S^*_{Y11} S^i_{11}}\right)
\tag{4.3.12}
$$

where S^i_{11} is the reflection coefficient at port 1 of the multiplexer containing i modules and $i = 2, \ldots, N-2$.

The multiplexer is constructed out of two substrates [73] held together by mechanical stress, with specifications presented in Table 4.1. Before the multiplexer is implemented, the filters need to be designed.

Table 4.1: Rogers RO4003C Substrate Specifications

Parameter	Value
Dielectric Constant (ε_r)	3.38
Dissipation Factor ($\tan\delta$)	0.0027
Substrate Height (H)	0.508mm
Etching (Copper) Thickness (T)	35μm

4.4 Channel Filters

As the channel filters are connected together through a manifold, with no form of isolation between the filters, the filters will interact with each other. In the stopband of a filter the input admittance response is a susceptance that varies with frequency, with the greatest variation in the stopband region closest to the passband.

Doubly-terminated filters are not suitable for the design of contiguous multiplexers because their large and rapidly varying input admittance response is not easily compensated for. Conversely, singly terminated filters have a reduced variation in the input admittance response [69] and for this reason this configuration is chosen.

Ten singly-terminated bandpass filters are connected to the multiplexer to divide the signal into equal-sized contiguous channels, while minimising interactions between channels. The filters are realised in stripline using half-wavelength staggered resonators [74], as depicted in Figure 4.12. Staggered resonator filters are compact, with resonators stacked together in a parallel array, and are capable of achieving the desired bandwidth.
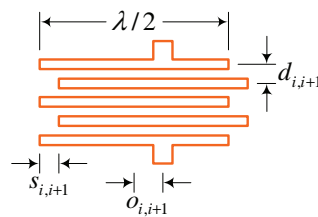
Figure 4.12: Staggered-Resonator Filter

The design specifications of the filters are presented in Table 4.2. The lengths of the resonators determine the centre frequency f_0 of the filter, the spacing $d_{i,i+1}$ between resonators and the stagger $s_{i,i+1}$ between resonators determine the bandwidth B and the offset $o_{i,i+1}$ between the tap locations to the terminations and the mid-point of the outer resonators determine the input and output coupling.

Table 4.2: Stripline Filter Specifications

Parameter	Value
Centre Frequency (f_0)	5.4GHz to 12.6GHz
Bandwidth (B)	800MHz
Passband Response (S_{11})	-15dB

The filter is designed using the insertion loss method, which has a high degree of control over the frequency response of the filter. This method begins with a low-pass filter prototype of lumped elements with normalised impedances at a normalised frequency. Singly-terminated filters have a resistor termination at one end and an infinite-impedance current-generator at the other end, as depicted in Figure 4.13.
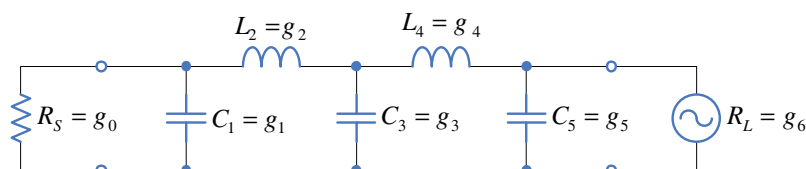
Figure 4.13: Fifth-Order Singly-Terminated Prototype Filter

A filter order of $n = 5$ is chosen as a compromise between a low order to facilitate a compact design and a high order to facilitate a sharp cut-off rate in the passband of adjacent filters. This choice of n results in an adjacent channel attenuation of 35dB at the centre of said channel. A $L_{Ar} = 0.1$dB Chebyshev response is chosen to maximise the passband and facilitate a sharp cut-off rate. The lumped-element values obtained from [75] are presented in Table 4.3, where $g_0 = 1.0000$ and $\omega'_1 = 1$.

Table 4.3: Stripline Filter Element Values

Parameter	Value	Parameter	Value
g_1	0.5734	g_4	1.5924
g_2	1.2490	g_5	1.3759
g_3	1.5562	g_6	∞

For practical implementation the load's infinite-impedance current-generator $R_L = g_6 = \infty$ is replaced by the finite-impedance generator g'_6 of 1.0116 using [75]

$$\frac{1}{R'_6} = \frac{1}{g'_6} = g_0 \text{antilog}_{10}\left(\frac{-L_{Ar}}{20}\right) \tag{4.4.1}$$

The filter bandwidths are readjusted to ensure that adjacent filters cross over at their 3dB points. The optimal fractional bandwidth is calculated as [75]

$$w = 2\left(\frac{f_b - f_0}{f_0}\right) / \left(\frac{\omega'}{\omega'_1}\right) \tag{4.4.2}$$

where f_a and $f_b > f_a$ are the desired cross-over points

$$
\begin{aligned}
f_0 &= \frac{f_a + f_b}{2} \\
\frac{\omega'}{\omega'_1} &= \cosh\left[\frac{1}{n}\cosh^{-1}\sqrt{\frac{1}{\varepsilon}\left(\frac{g_0}{ReY'_k} - 1\right)}\right] \\
\varepsilon &= \left[\text{antilog}_{10}\left(\frac{L_{AR}}{10}\right)\right] - 1
\end{aligned}
\tag{4.4.3}
$$

and $ReY'_k = \log_{10} 3$ is the 3dB point. The optimal bandwidth is adjusted from 800MHz to 702MHz.

The advantage of using singly-terminated filters is highlighted by comparing the phase variation of the reflection coefficient of the filter with a centre frequency of 6.2GHz with that of an equivalent doubly-terminated filter, as depicted in Figure 4.14. As can be seen, there is a large phase variation in the passbands of the two adjacent filters, with a reduced variation in the singly-terminated configuration.
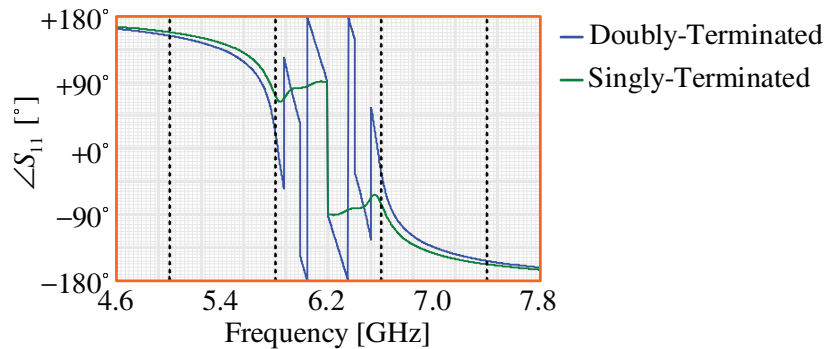
Figure 4.14: Phase Variation Comparison between Doubly-Terminated and Singly-Terminated Filters

Lumped-circuit elements are difficult to construct at microwave frequencies, therefore transformations are applied to convert the lumped-element prototype to distributed-element form at the desired frequency range and impedance level [75]. The stagger between resonators are modelled as impedance-inverters and the half-wavelength resonators are modelled as series resonators, as depicted in Figure 4.15.
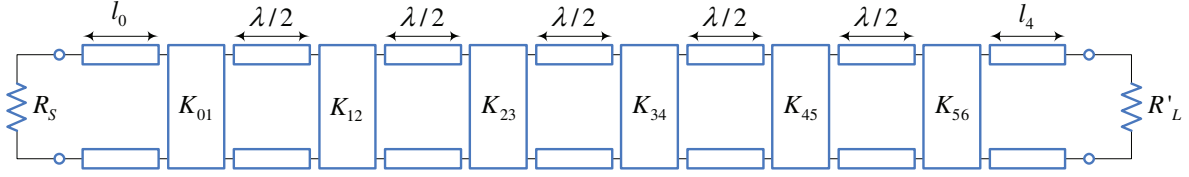
Figure 4.15: Fifth-Order Distributed-Element Filter

The values for the impedance-inverters are calculated as

$$
\begin{aligned}
K_{01} &= \sqrt{\frac{R_S x_1 B}{g_0 g_1 f_0}} \\
K_{i,i+1}\big|_{i=1,\ldots,4} &= \frac{B}{f_0}\sqrt{\frac{x_i x_{i+1}}{g_i g_{i+1}}} \\
K_{56} &= \sqrt{\frac{R'_L x_5 B}{g_5 g'_6 f_0}}
\end{aligned}
\tag{4.4.4}
$$

where $R_S = Z_0$ is the source impedance, $R'_L = Z_0 g'_6$ is the load impedance, $Z_0 = 50\Omega$ is the characteristic impedance and x_i is the reactance slope parameter of the series resonators

$$
x_i\big|_{i=1,\ldots,5} = \frac{\omega_0}{2}\frac{dX_i(\omega)}{d\omega}\bigg|_{\omega=\omega_0}
\tag{4.4.5}
$$

where ω_0 is the resonant frequency and X_i is the reactance. Half-wavelength resonators reduce x_i to $\frac{\pi}{2}$.

The inner impedance-inverters $K_{i,i+1}$ are realised by the degree of stagger $s_{i,i+1}$ between adjacent resonators

$$
k_{i,i+1}\big|_{i=1,\ldots,4} = \frac{K_{i,i+1}}{\sqrt{x_i x_{i+1}}}
\tag{4.4.6}
$$

where $k_{i,i+1}$ is the coupling strength between resonator i and resonator $i+1$, and the outer impedance-inverters K_{01} and K_{56} are realised by the degree of offset $o_{0,1}$ and $o_{5,6}$, which determines the external Q factor

$$
\begin{aligned}
(Q_e)_S &= \frac{g_0 g_1 f_0}{B} \\
(Q_e)_L &= \frac{g_5 g'_6 f_0}{B}
\end{aligned}
\tag{4.4.7}
$$

where $(Q_e)_S$ is the Q factor at the termination R_S and $(Q_e)_L$ is the Q factor at termination R'_L.

The filters are designed in CST MWS [42] using a lossless version of the substrate to speed up the simulations, with a minimal loss of accuracy as resonance frequencies are independent of conductivity. As the passband is affected by the loss of the substrate, a lossy simulation is run to verify the results. The filters are designed to meet the restrictions presented in Table 4.4 imposed by available manufacturing processes.

Table 4.4: Multiplexer Design Restrictions

Parameter	Minimum Value
Etching Width (W)	0.3mm
Etching Spacing (D)	0.2mm

The stagger between adjacent resonators are determined by running eigen-mode analyses in CST MWS. Two adjacent resonators are constructing in CST MWS, as depicted in Figure 4.16, with the eigenmode solver calculating the electric and magnetic resonant frequencies of the structure as the stagger and spacing is varied.

Figure 4.16: CST MWS Eigenmode Solver Setup for Stripline Filters

These resonant frequencies can be used to calculate the resultant coupling strength

$$k \quad = \quad \frac{f_e^2 - f_m^2}{f_e^2 + f_m^2} \tag{4.4.8}$$

where f_e is the electric resonant frequency and f_m is the magnetic resonant frequency. This is used to determine the spacing and stagger between resonators required to obtain the coupling strength calculated using Equation 4.4.6.

The offset between the tap locations to the terminations and the mid-point of the outer resonators are determined by running frequency domain analyses in CST MWS. By constructing a resonator and tap location connected to a port in CST MWS and sweeping the offset between them, as depicted in Figure 4.17, the frequency-domain solver is used to calculate the loaded Q factor of the structure. This is used to determine the offset between the resonator and the port required to obtain the Q factor calculated using Equation 4.4.7.
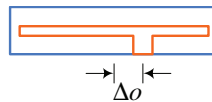
Figure 4.17: CST MWS Frequency Domain Solver Setup Stripline Filters

Once all the required parameters of the filter have been calculated, the filter can be constructed in CST MWS, with frequency-domain analyses performed to optimise the design. One reason why the individually calculated parameters do not immediately match up to a finished design, it that as stagger is introduced between two resonators the resonant frequency of the structure is changed as given by the relationship

$$f_0 \quad = \quad \sqrt{f_e f_m} \tag{4.4.9}$$

where f_0 is the resonant frequency of the structure.

By adjusting the length of resonators i and $i+1$ to compensate for the shift in resonant frequency between them, while still maintaining the coupling factor $k_{i,i+1}$, the coupling between resonators $i+1$ and $i+2$ is altered and needs to be adjusted. But, the length of resonators $i+1$ and $i+2$ need to be adjusted to compensate for the shift in resonant frequency between them, while still maintaining the coupling factor $k_{i+1,i+2}$.

Optimisation is required to find the best solution for these opposing adjustments. Initially, manual adjustments are made to the parameters by noting that the resonator lengths determine the resonant frequency, the resonator spacing determine the bandwidth and the tap locations determine the reflection coefficient, with the bulk of the optimiation performed using the built-in optimiser.

These optimisation processes are very time consuming, with five resonator lengths, five resonator widths, four inter-resonator spacings, four inter-resonator staggers and two termination offsets as inputs, and very computationally intensive, with the structure of each of the ten filters divided into $\approx 300,000$ mesh cells. The optimisation goals have very tight constraints, with the filters not allowed to exceed their bandwidths in order to have the cross-over point between adjacent channels at the half-power points.

The CST MWS results are depicted in Figure 4.18. The top two graphs depict the reflection and transmission response of the five filters in the lower half of the frequency range, with the bottom two graphs depicting the reflection and transmission response of the five filters in the upper half of the frequency range. The reflection and transmission response are seen from port 2 as when using singly-terminated filters in a multiplexer this is the port that will be connected to the common port of the multiplexer.
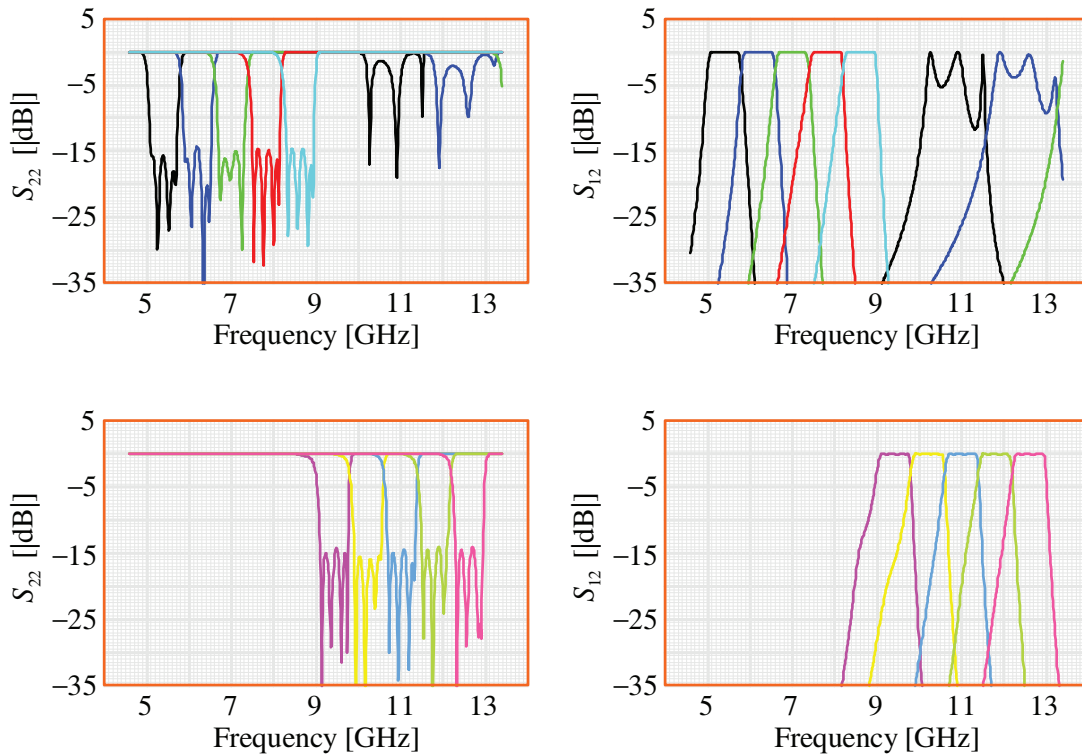
Figure 4.18: CST MWS Staggered-Resonator Filter Response

It is clear from the graphs that a significant problem is created by the second harmonic of the low-band filters, which overlap with the passbands of the high-band filters. These higher-order passbands must be suppressed before the filters can be combined to form a multiplexer. This is achieved by incorporating the bandpass filter described in Section 4.5 into the multiplexer design along the manifold at a position between the lowest three filters and the rest of the filters.

As can be seen in the graphs of Figure 4.18, all of the filters display a passband response of $S_{11} = -15$dB, with the cross-over between the filters at the half-power points. Therefore, these filters meet the design specifications and are ready to be coupled together to form a multiplexer using the technique described in Section 4.3. Technical drawings of the positioning of the filters within the multiplexer structure are shown in Appendix A.3.

4.5   Isolation Filter

One of the major problems associated with wideband multiplexers is that the higher-order passbands of the filters in the lower half of the frequency range fall within the passbands of the filters in the upper half of the frequency range. In this work it can be clearly seen in the CST MWS results depicted in Figure 4.18 that the three filters in the lower half of the frequency range have higher-order passbands that would interact with the passbands of the filters from upwards of 10GHz.

In this work the upper half of the frequency range needs to be isolated from the higher-order passbands of the the lowest three filters. A potential solution is to divide the whole frequency range at the common port into subgroups. The subgroups can then be isolated from each other using immittance compensation-annulling networks at the connections to the main group [58] or by placing a diplexer at the connection to the main group that is designed to suppress higher-order passbands [76, 77].

An alternative is to connect a bandpass filter along the manifold between the three filters in the lower half of the frequency range and the seven filters in the upper half of the frequency range. This filter will pass signals that fall within the passbands of the three filters in the lower half of the frequency range, while suppressing signals that fall within the passbands of the seven filters in the upper half of the frequency range, thereby isolating these two sets of filters from each other.

This filter can be realised in stripline using shorted half-wavelength resonators spaced quarter-wavelengths apart, as depicted in Figure 4.19. This filter is very simple to design, but did cause problems during the manufacturing process. As can be seen in the technical drawings of the multiplexer structure in Appendix A.3, the substrate of the contains two cut-outs at the ground planes of this filter, with the walls of the metal housing machined in such a way as to make contact with these ground planes.
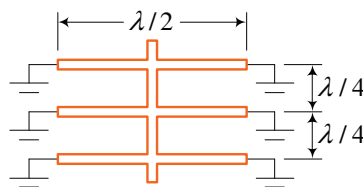
Figure 4.19: Shorted-Resonator Filter

The design specifications of the filter are presented in Table 4.5. The specified passband has been chosen so as to be well-matched over the passbands of the three filters in the lower half of the frequency range, while sufficiently suppressing their higher-order passbands. The lengths of the resonators determine the centre frequency f_0 of the filter, the spacing between resonators determine the bandwidth B and the width of the centre line of the filter determines the passband response S_{11}.

Table 4.5: Stripline Filter Specifications

Parameter	Value
Centre Frequency (f_0)	6.2GHz
Bandwidth (B)	3.6GHz
Passband Response (S_{11})	-15dB
Attenuation (S_{21})	$20\text{dB}\big|_{f>10\text{GHz}}$

The filter dimensions are first optimised using ideal stripline elements in AWR MWO [78] before being optimised using physical dimensions in CST MWS [42]. The CST MWS results are depicted in Figure 4.20. The attenuation $S_{21}|_{f>10\text{GHz}} < -20$dB in the passbands of the filters in the upper half of the frequency range is sufficient to suppress the higher-order passbands of the filters in the lower half of the frequency range.
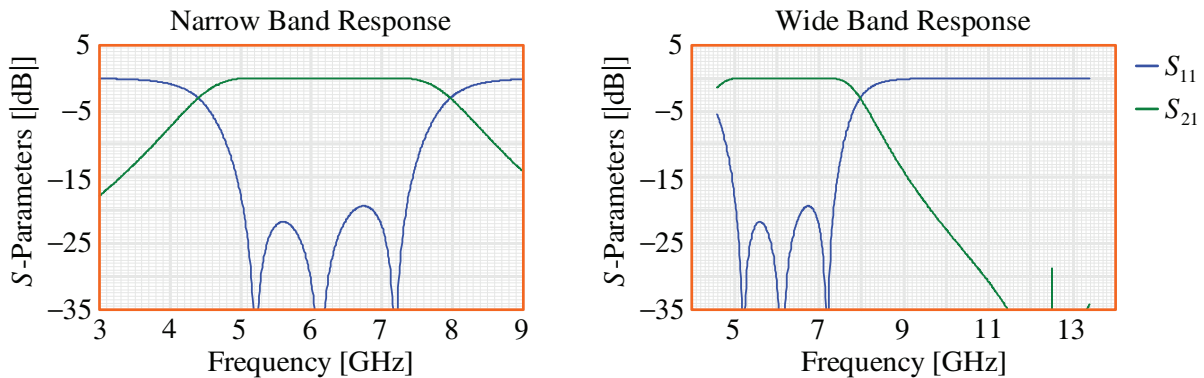
Figure 4.20: CST MWS Simulated Shorted-Resonator Filter Response

4.6 Transition

A coaxial-to-stripline transition is designed to efficiently launch energy from the second IF amplifier's SMA connector output to the stripline configuration of the multiplexer. The transition is a controlled step that minimises and compensates for the difference in dimensions between the SMA connector and the stripline circuit.

Excessive reactance is caused at the transition by the difference in the radial field distribution inside the connector and the almost rectangular field distribution inside the stripline circuit. Compensation is required to minimise the reflection caused by this reactance even if the circuit and launcher have the same characteristic impedance.

The literature contains a number of manufacturing process that would reduced this reactance. In [79] the side walls of the metal housing are positioned at the start of the transition sufficiently far away from the stripline to avoid discontinuities. In [80] a hole is drilled under the pin of the connector where it attaches to the substrate. In [81] the centre conductor and housing of the coaxial connector are modified. However, these techniques may not be suitable at high frequencies due to the extreme tolerances required.

Alternatively, when using standard connectors and conventional manufacturing processes, the design of the transition can be optimised to reduce the reactance based on a rigorous mode-matching analysis of the transition that takes into account all the geometrical details pertaining to the structure [82]. However, such an analysis is unnecessary if the connector is chosen to only support TEM mode and be mode free up to the upper frequency range limit of 13GHz, as is the case with standard SMA connectors which are mode free up to 27GHz.

In making use of standard SMA connectors the transition can be more simply modelled using equivalent circuits based just on the TEM propagation mode. Two such equivalent circuits are those of [83] and [84], in which the transition is modelled by a parallel per-unit capacitance and a series per-unit inductance that were experimentally and empirically derived. These equivalent circuits can be used to optimised the transition to reduce the reactance.

However, instead of following the arduous scheme of obtaining a model for the transition and optimising this model before realising this model in stripline, a minimal use of electromagnetic analysis software is required if care is taken in selecting the transition components [85]. Reflection at the transition is minimised by matching the dimensions of the connector and the stripline circuit, with a taper incorporated into the design to ensure there are no discontinuities at the transition, as depicted in Figure 4.21.
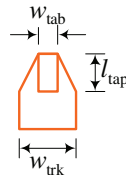
Figure 4.21: Stripline Transition

The design specifications of the transition section are presented in Table 4.6. The match in dimensions between the connector and the substrate, as well as the use of the taper, minimise the reflection at the transition. For the given dielectric constant of the substrate the width w_{trk} of the substrate track is calculated to obtain the specified impedance of the track. This is estimated to be 0.52mm using TXLINE, an add-on program of AWR MWO, and verified by performing a full-wave analysis in CST MWS.

Table 4.6: Transition Section Design Specifications

Parameter	Value
Frequency Range (f_L to f_H)	5GHz to 13GHz
Impedance	50Ω
Passband Response (S_{21})	$-30\text{dB}_{\text{min}}$

The first step in the transition design is to choose the connector dielectric so that there is a minimum in the step between the size of the radius r_{die} of the connector dielectric and the thickness t_{sub} of the substrate, as depicted in Figure 4.22. A good match in dimension between the connector and the substrate eases the manufacturing process by having the metal housing of the multiplexer matching the dimensions of the metal housing of the connectors, and reduces the discontinuity at this point substantially.
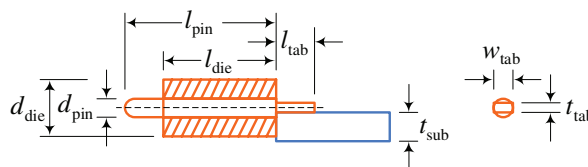
Figure 4.22: Step between Connector and Substrate

The second step in the transition design is to choose the connector launch pin so that there is a minimum in the step between the size of the width w_{tab} of the connector launch and the width w_{trk} of the substrate track. The correct choice of connector launch pin also eases the manufacturing process, as in choosing the thickness t_{tab} of the launch pin to be as thin as possible there is a minimum of obstruction to the adhesion of the top layer of the substrate to the bottom layer of the substrate.

The parameters of the chosen connector [85] are presented in Table 4.7. The step between the substrate thickness t_{sub} of 0.508mm and the connector dielectric radius r_{die} of 0.4953mm is at a minimum of 0.0127mm and the thickness t_{tab} of the flat tab launcher is 0.1016mm, as opposed to the round pin launcher with diameter $d = 0.1778$mm. The Southwest 214-11SF SMA jack [85] is chosen, as its rear socket is designed to accept the 1090-07G Pin/Tab and because its dimensions suit the rectangular shape of the multiplexer.

Table 4.7: Southwest 1090-07G Pin/Tab Parameters

Part	Parameter	Value
Dielectric	Length (l_{die})	4.7500mm
	Radius (r_{die})	0.4953mm
Pin	Length (l_{pin})	5.7150mm
	Radius (r_{pin})	0.1524mm
Tab	Length (l_{tab})	0.6350mm
	Thickness (t_{tab})	0.1016mm
	Width (w_{tab})	0.3048mm

The third step of the design is to compensate for the variance between the width of the substrate track and the connector tab. A linear taper is included that is as wide as the tab at the launch and increases to the width of the track over the optimal length of l_{tap} of 1.02mm, obtained using CST MWS [42]. The CST MWS results of the full transition are depicted in Figure 4.23. There is a passband response of $S_{11} < -30$dB over the whole range.
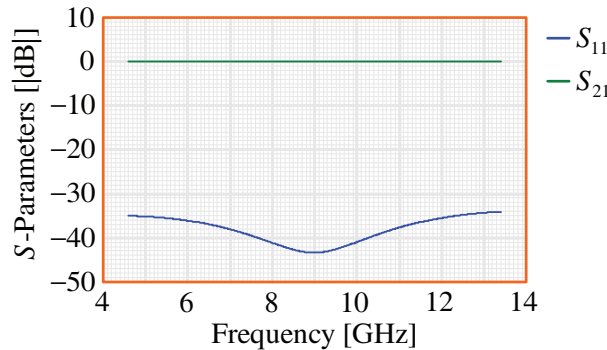
Figure 4.23: CST MWS Simulated Transition Response

4.7 Implementation

The number of filters in the multiplexer has a significant impact on the rest of the system. On a positive note the more filters there are, the higher the resolution, which would lead to a more interpretable image for the operator. However an increase in filters would result in a larger number of detectors and a larger dataset for the image reconstruction algorithm, thereby significantly increasing the cost of the system.

A number of 40 channels was originally proposed as a specification for this system. The dimensions of such a multiplexer would exceed the dimensions of the antenna if placed along a linear manifold, with the combined mass and size potentially exceeding the available space on the wing of a small UAV. Therefore a few novel implementations were investigated to reduce the size of such a multiplexer.

Firstly, four-port junctions were proposed to potentially half the length of the manifold. However, with no literature to support such a design the optimal lengths of the connections between channels and junctions would be based purely on optimisation techniques and not on mathematical formulae. Also, this option would not significantly reduce the size of the multiplexer as spacing between filters is required to prevent coupling.

Secondly, a multilayer configuration of filters was proposed instead of the making use of a single layer of substrate for the multiplexer. The connections between the layers would be achieved using slots to couple between layers [86]. Such a multiplexer would would significantly reduce the length of the multiplexer, however it is difficult to realise the required bandwidths using slots and to prevent coupling to the filters.

Even if a viable configuration was found in having 40 separate filters to connect onto a singular manifold the optimisation of the connections between the channels and junctions would involve a large number of parameters. Therefore it would be beneficial to be able to subdivide the multiplexer into sections that are isolated from each other, thereby allowing each section to be optimised using a smaller dataset of parameters. Such a multiplexer could be implemented using the technique of [87], which employs a bandstop filter per section.

However, the design of a 40 stripline filters was deemed to be too time intensive for a first iteration of the imaging system. It was decided that a scaled down system of 10 channels would be a good compromise between image resolution and the required number of components to built a working system from scratch. This could then be used as the basis for further research into any one of the various sections of the whole system.

The majority of contiguous multiplexers in the literature cover a narrow bandwidth [68, 69], with no overlap between the higher-order passbands of filters in the lower half of frequency range and the passbands of filters in the upper half of the frequency range. Also, waveguide is the medium of choice because of the much lower loss at microwave frequencies than stripline, but is not an option in this work due to the wide bandwidth.

When dealing with a narrow band multiplexer the design techniques of [70, 71] give good results as it is easy to design junctions and connections that are optimal over narrow bands, as encountered when only a few filters had been connected together as depicted in Figure 4.24. The same cannot be said for wide band applications, especially when the frequencies of the lower end of the frequency range have harmonics at wavelengths in upper half of the frequency range, as encountered when all the filters has been connected together.
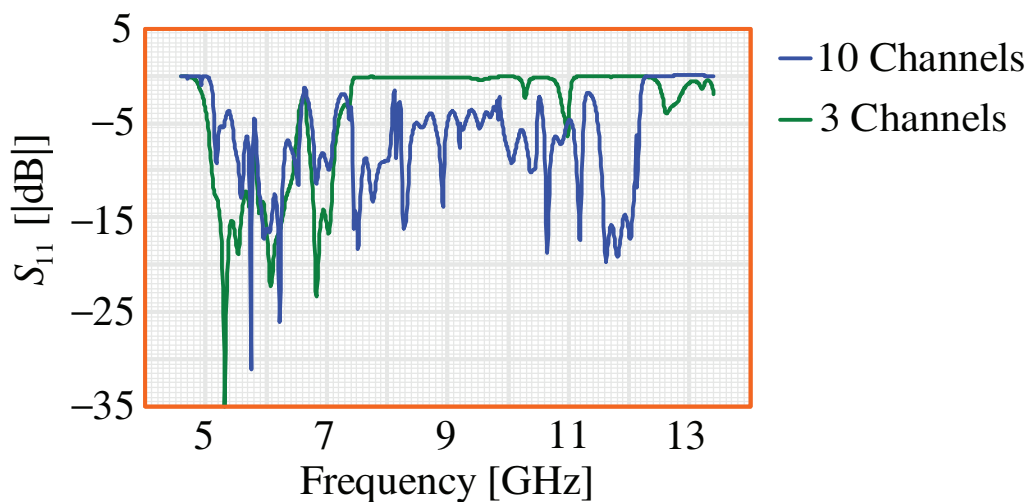
Figure 4.24: AWR MWO Simulated Multiplexer Response for Different Numbers of Channels

Therefore, intensive optimisation is required to obtain reasonable results for a contiguous wideband stripline multiplexer. However, this can not be done using full-wave analyses in CST MWS due to the large size of the multiplexer. A single pass of the multiplexer containing ≈ 2.3 million mesh cells took ≈ 24hrs to run on a 2.66GHz quad-core PC with 8GB of RAM.

The filters, junctions and transitions that were individually designed using the electromagnetic solver CST MWS [42] need to be combined into a multiplexer using the technique described in Section 4.3. This is performed in the linear solver AWR MWO [78] using models of lossy stripline elements together with the filter *S*-Parameter blocks as calculated by CST MWS to obtain the connection distances.

An optimisation routine is run after each module S_{jun}^i, where $i = 1, \ldots, N - 1$, is built to optimise all the lengths between the existing filters and junctions. After this routine has obtained an optimal response is the next filter and junction added. The optimisation process becomes very time-consuming as the number of channels increase. Technical drawings of the multiplexer are shown in Appendix A.3.

The completed multiplexer is combined in CST MWS to perform a full-wave analysis and check for any coupling between the closely-spaced filters. The AWR MWO and CST MWS results are depicted in Figure 4.25. The passband response of the individual filters is favourable, with the cross-over between the filters at the half-power points, but the passband response of the common port is poorly matched over the frequency range.
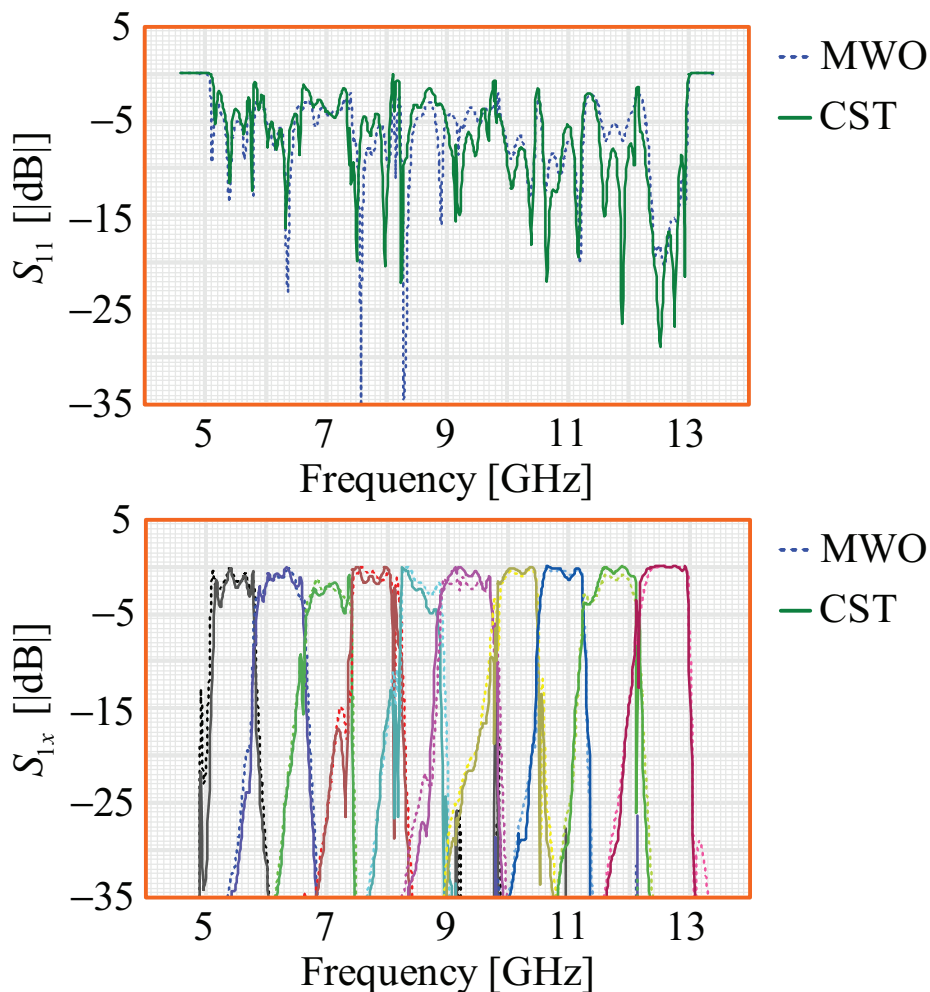
Figure 4.25: AWR MWO and CST MWS Simulated Multiplexer Response

4.8   Measurements

The multiplexer is built according to the technical drawings shown in Appendix A.3, as depicted in Figure 4.26 with the top layer of the substrate and metallic housing removed. The isolation filter is seen between the three filters in the lower half of the frequency range and the seven filters in the upper half of the frequency range.
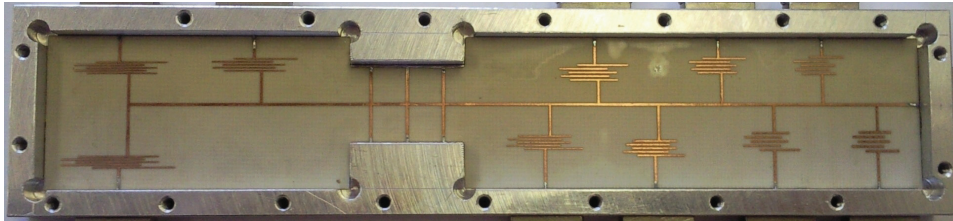
Figure 4.26: Top View of Multiplexer

Measured results for the output reflection responses of the filters using a network analyser [43] are shown in Figure 4.27. The upper graph depicts the reflection response of the 5 filters in the lower half of the frequency range. The lower graph depicts the reflection response of the 5 filters in the upper half of the frequency range.
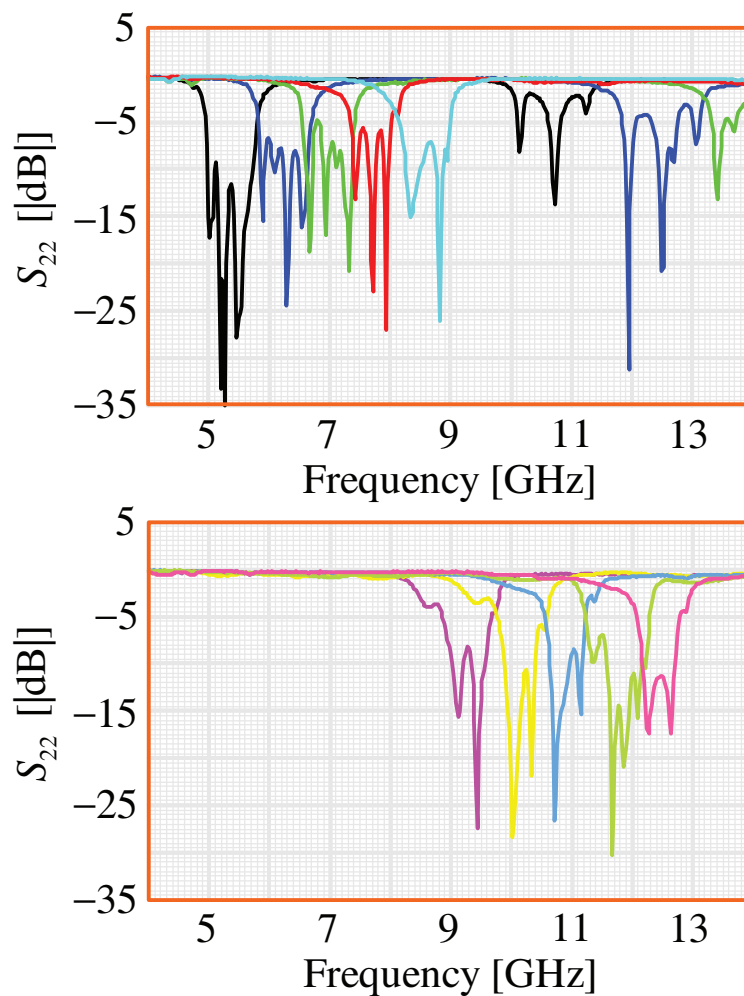
Figure 4.27: Measured Multiplexer Filter Response

This separation in the depiction of the filter response is made because the filters in the lower half of the frequency range have higher-order passbands that fall within the passbands of the filters in the upper half of the frequency range. While the three filters in the lower half of the frequency range are matched at the location of their higher-order passbands, the inclusion of the isolation filter into the multiplexer design suppresses their higher-order passbands.

Measured results for the common port response of the multiplexer using a network analyser [43] are shown in Figure 4.28. It can be seen that the isolation filter negatively affects the multiplexer over the passband of the isolation filter as the common port response of the multiplexer and the passbands of the channel filters are significantly better outside of the passband of the isolation filter. Nevertheless, good channel separation is achieved over most of the band.
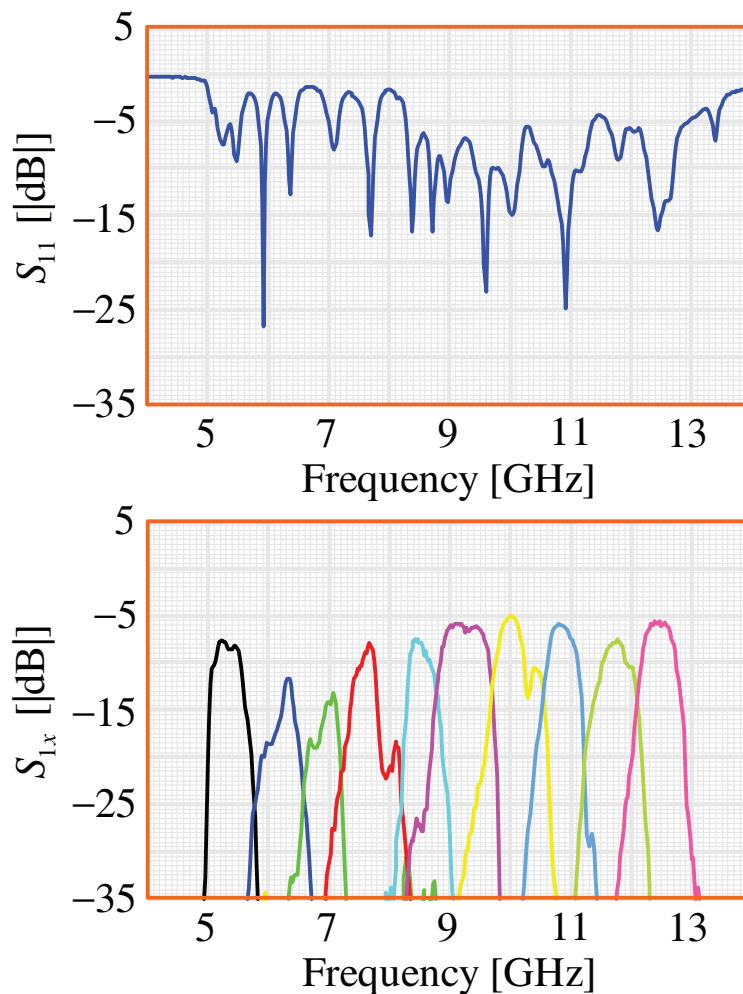
Figure 4.28: Measured Multiplexer Common Port Response

The key design characteristic of the multiplexer is to split the common port signal into ten isolated bands, which based on Figure 4.28 is a function that it clearly achieves. However, the multiplexer has a poorly matched response that decreases the signal levels at the output of the multiplexer. Also, the poorer response at the lower end of the frequency range leads to uneven signal levels between the bands. This inequality is one of the defects that the calibration process described in Chapter 5 is used to reverse.

4.9 Conclusion

In this chapter the multiplexer design is described. The wideband, contiguous nature of the multiplexer places severe restrictions on the possible implementations, with the chosen design a manifold-coupled stripline multiplexer. While a waveguide implementation would have been less lossy at microwave frequencies, the 1.6 octave bandwidth of the multiplexer cannnot be realised in waveguide.

Even for this implementation the wideband nature of the multiplexer is problematic, especially with regards to the higher-order passbands of the filters in the lower half of the frequency range that fall within the passbands of the filters in the upper half of the frequency range. These higher-order passbands are suppressed by placing an isolation filter along the manifold between the lowest three filters and the rest of the filters.

From the measurements made of the multiplexer, it can be seen that the multiplexer does divide up the frequency range into the desired channels, with no overlap between adjacent channels and no spurious passbands. However, the multiplexer is not well matched, which will lead to a large percentage of the signal being reflected back instead of being passed onto the detectors.

Chapter 5

Radiometer

5.1 Introduction

As discussed in Chapter 2, a frequency-scanned array couples the Millimetre-Wave (MMW) emissions from the target area as a function of frequency along the plane perpendicular to the flight path. A multiplexer is used to separate the captured MMW emissions into M equal-sized contiguous bandwidths to use the space-to-frequency mapping property of the antenna to form the images, as depicted in Figure 5.1.
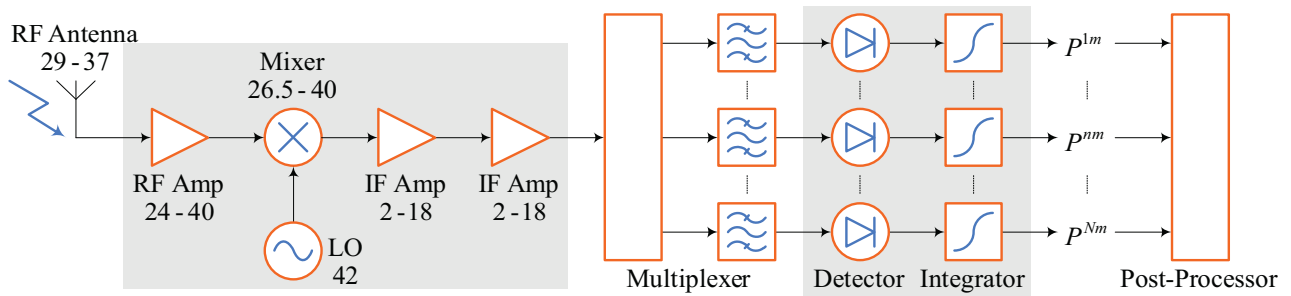
Figure 5.1: Radiometer with Analogue Stages Highlighted

In this chapter the analogue components of the radiometer are discussed. These components combine to convert the captured MMW emissions into pixels by sampling at discrete time-intervals during the flight path time-period t_0 to t_N. The combination of flight-measuring and scan-filtering maps the $w \times h$ coordinate system of the target area to the $f \times t$ coordinate system of the image of size $N \times M$, as depicted in Figure 5.2.
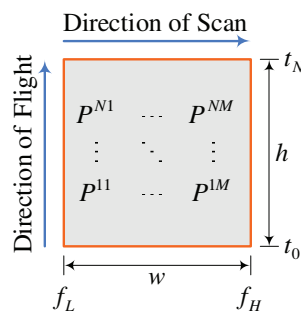
Figure 5.2: Target Area

5.2 Detectors

The two core functions of any radiometric system are the coupling of the free-space emissions to the radiometer and the conversion of the captured emissions to a format that can be formed into an image for display to the operator. The first function is performed by an antenna, with the frequency-scanned array of this implementation described in Chapter 3, and the second function is performed by logarithmic detectors, as described here.

While devices such as Monolithic Millimetre-Wave Integrated Circuits (MMICs) [14, 26] are capable of direct amplification and detection at MMW frequencies, the majority of affordable, off-the-shelf detectors are only operational up to 10GHz [27, 28, 29]. Therefore, a heterodyne system is employed to mix the captured MMW emissions down to a detectable frequency range.

The specifications of the detectors [29] used for this application are presented in Table 5.1. These detectors convert the $M = 10$ outputs of the multiplexer to decibel-scaled voltages for input to the post-processor. While the detectors are not specified to work at the upper end of the Intermediate Frequency (IF) range, limited operation is possible as the cost of a reduced dynamic range.

Table 5.1: Hittite HMC602 Logarithmic Detector Specifications

Parameter	Value
Frequency Range	1MHz to 8GHz
3dB Input Range	−60dBm to 10dBm
Output Range	0.3V to 2.0V

Because the detectors are used outside of the specified frequency ranges, measurements are performed to determine the dynamic range of the detectors over the IF range. The input of the detectors is connected directly to a frequency source [88] that sweeps the frequency over the IF range for power levels over the range of −50dBm to +0dBm. The output measured on an oscilloscope [89] is depicted in Figure 5.3.
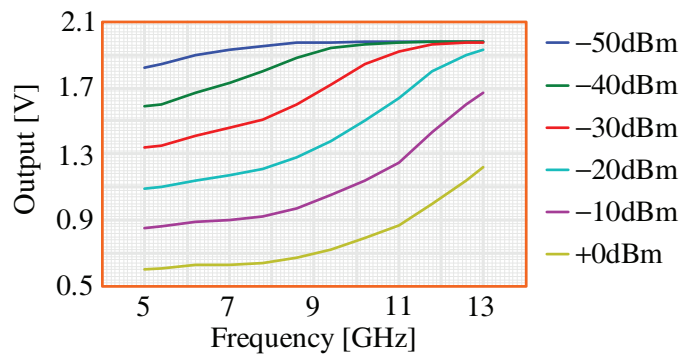
Figure 5.3: Detector Dynamic Range over whole Frequency Range

As can be seen the detectors are operational up to the upper limit of the IF range, but with a dynamic range that decreases as the frequency increases. The dynamic range decreases from a range of 50dB centred around −20dBm at 5GHz to a range of 20dB centred around −10dBm at 13GHz. Therefore, in order to achieve a consistent output range over the whole IF range, the input level to the detectors must be kept within a range of ±10dB around −10dBm.

When measuring the combined multiplexer-detector system, it should be kept in mind that, in covering a range of 1.6 octaves at the IF range the higher-order passbands of the filters in the low-band filters fall within the passbands of the high-band filters. A bandpass filter is incorporated in the multiplexer design to suppress the higher-order passbands of the filters in the lower half of the frequency range.

Measurements are performed to test that the bandpass filter sufficiently suppresses these higher-order passbands. This is done by connecting a detector to the multiplexer output of the channel centred at 6.2GHz, while a frequency source [88] connected to the common port of the multiplexer sweeps the frequency over the IF range for power levels over the range of −50dBm to +0dBm. The output measured on an oscilloscope [89] is depicted in Figure 5.4.
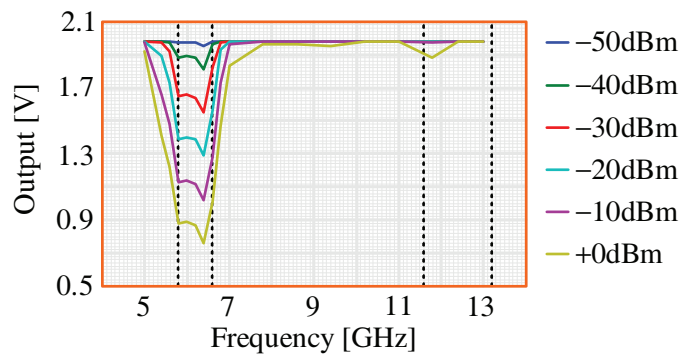
Figure 5.4: Detector Dynamic Range for Channel Two

As can be seen the output of the detector is limited to the passband of the channel, with only signals in the region of 0dBm being detected within a limited region of the higher-order passband and within a limited region adjacent to the upper cut-off frequency of the channel. Therefore, it can be safely assumed that the output of the detector is only a function of the desired range. However, it should be noted that the loss of the multiplexer has reduced the dynamic range by approximately 10dB.

5.3 Down-Converter

As the frequency ranges of affordable, commercially available detectors are lower than that of the MMW emissions, a Local Oscillator (LO)-mixer combination down-converts the Radio Frequency (RF) range f_{RF} of 29GHz to 37GHz of the MMW emissions to the lower IF range f_{IF} of 5GHz to 13GHz of the detectors.

The down-converter is a Ka-band mixer [30], with specifications presented in Table 5.2. For a given frequency, f_{RF}, at the input, the output of the mixer consists of two signal, one at $f_{LO} - f_{IF}$ and the other at $f_{LO} + f_{IF}$, where f_{LO} is the frequency of the LO. In choosing f_{LO} correctly, the whole MMW range will be down-converted to a range of frequencies given by $f_{LO} - f_{IF}$ that are measurable by the detector.

Table 5.2: Spacek MKa-8 Mixer Specifications

Parameter	Value
RF Input	26.5GHz to 40GHz
IF Output	2.0GHz to 15.5GHz
Conversion Loss	$5.0dB_{typical}$, $6.0dB_{max}$

The LO is a mechanically-tuned Gunn oscillator [31], with specifications presented in Table 5.3. With a f_{LO} of 42GHz, the desired IF range is obtained from the RF range. However, the oscillator has a spurious at 25GHz, which combines with the 42GHz signal to create spurious signals within the IF range.

Table 5.3: Spacek GKa-420 Mechanically-Tuned Gunn Oscillator Specifications

Parameter	Value
Output Frequency	42.0GHz
Output Power	12dBm

For a large input signal these spurious signals would be hidden, but in the case of noise measurements these spurious signals are the dominate signals in the IF output of the mixer. With a matched waveguide load attached to the RF input of the mixer, power measurements are performed on the IF output using a spectrum analyser [50]. The output of the mixer contains five problematic spurious signals, as depicted in Figure 5.5.
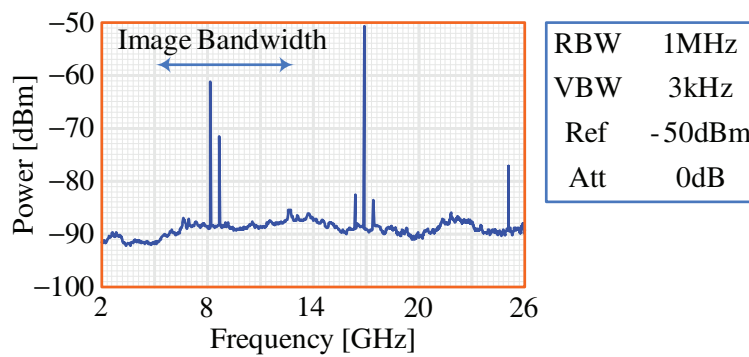
Figure 5.5: Mixer Output Spectrum

The two signals at 8.2GHz and 8.8GHz fall within the IF range causing streaks that dominate the image, saturating their frequency bins and relegating the rest of the image to a homogeneous background, as depicted in Figure 5.6. These images were measured using the full reflector configuration as described in Chapter 3. The removal of these streaks returns the contrast to the image.
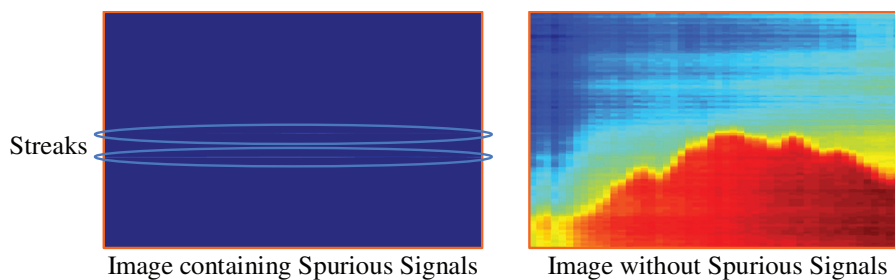
Figure 5.6: Effect of Spurious Signals on Image

The three signals at 16.3GHz, 16.9GHz and 17.6GHz fall within the 2GHz to 18GHz frequency range of the IF amplifier. Unless removed the -55dBm signal at 16.9GHz would be amplified to 13dBm by the two 32dB amplifiers, thereby saturating the second intermediate amplifier, with a 1dB compression point of 8dBm.

5.4 Waveguide Filter

A doubly-terminated bandpass filter is placed between the oscillator and the mixer to suppress the spurious signal at 25GHz, while minimising the attenuation of the 42GHz signal. The filter is realised in waveguide using coupling posts interspersed with half-wavelength spacing, as depicted in Figure 5.7.
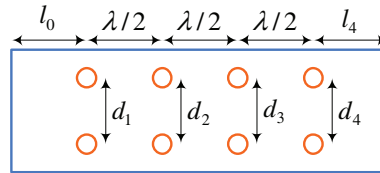
Figure 5.7: Top View of Coupling-Post Filter

The design specifications of the filter are presented in Table 5.4. The centre frequency f_0 is a function of the size of the resonant cavities spaced between the coupling posts, the bandwidth B is a function of the coupling between the posts, which is determined by the spacing d between the posts and the attenuation at the leakage signal is a function of the filter response.

Table 5.4: Waveguide Filter Specifications

Parameter	Value
Centre Frequency (f_0)	42.0GHz
Bandwidth (B)	1.6GHz
Attenuation	$50\text{dB}\big|_{f=25\text{GHz}}$

The filter is designed using the insertion loss method, which has a high degree of control over the frequency response of the filter. This method begins with a low-pass filter prototype of lumped elements with normalised impedances and terminations at a normalised frequency, as depicted in Figure 5.8.
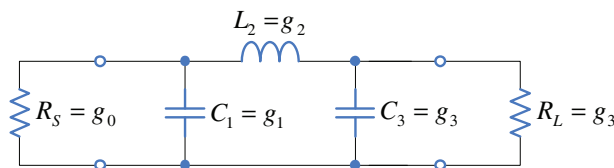
Figure 5.8: Third-Order Doubly-Terminated Prototype Filter

As the two outputs of the LO are spaced far apart, even for a low filter order of $n = 3$ the attenuation of the leakage signal is much greater than 50dB. The response of the filter is chosen as $L_{Ar} = 0.01\text{dB}$ Chebyshev. The lumped-element values obtained from [75] are presented in Table 5.5, where $g_0 = 1.0000$ and $\omega_1' = 1$.

Table 5.5: Waveguide Filter Element Values

Parameter	Value	Parameter	Value
g_1	0.6291	g_3	0.6291
g_2	0.9702	g_4	1.0000

The lumped elements of the prototype filter are difficult to implement at microwave frequencies, and must therefore by approximated with distributed elements [75]. The coupling posts are modelled as impedance-inverters and the half-wavelength spacings are modelled as series resonators, as depicted in Figure 5.9.
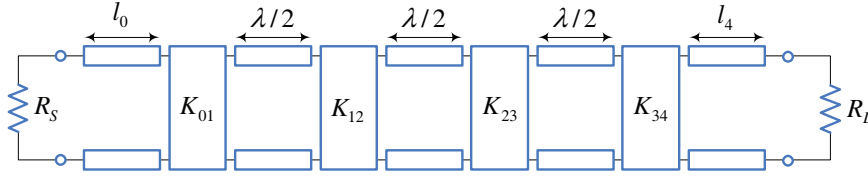
Figure 5.9: Third-Order Distributed-Element Filter

The values for the impedance-inverters are calculated as

$$
\begin{aligned}
K_{01} &= K_{34} = \sqrt{\frac{R_S x_1 B}{g_0 g_1 f_0}} \\
K_{12} &= K_{23} = \frac{B}{f_0}\sqrt{\frac{x_1 x_2}{g_1 g_2}}
\end{aligned}
\tag{5.4.1}
$$

where $R_S = Z_0$ is the source impedance, $R_L = Z_0$ is the load impedance, $Z_0 = 50\,\Omega$ is the characteristic impedance and x_i is the reactance slope parameter of the series resonators [75]

$$
x_i = \left.\frac{\omega_0}{2}\frac{dX_i(\omega)}{d\omega}\right|_{\omega=\omega_0}
\tag{5.4.2}
$$

where ω_0 is the resonant frequency and X_i is the reactance of resonator i for $i = 1, 2, 3$. The series resonators are realised by $\frac{\lambda}{2}$-lengths of waveguide reducing $x_i = \frac{\pi}{2}$, where $\lambda = \frac{c_0}{f_0}$ and c_0 is the speed of light in a vacuum.

The inner impedance-inverters $K_{12} = K_{23}$ are realised by the by the spacing $d_2 = d_3$ between the two inner inductive-post pairs, which determines the strength of the coupling between the resonators

$$
k_{12} = k_{23} = \frac{K_{12}}{\sqrt{x_1 x_2}}
\tag{5.4.3}
$$

where $k_{i,i+1}$ is the coupling strength between resonator i and resonator $i+1$.

The outer impedance-inverters $K_{01} = K_{34}$ are realised by the spacing $d_1 = d_4$ between the two outer inductive-post pairs, which determines the strength of the coupling between a resonator and a termination

$$
(Q_e)_S = (Q_e)_L = \frac{g_0 g_1 f0}{B}
\tag{5.4.4}
$$

where $(Q_e)_S$ is the Q at termination R_S and $(Q_e)_L$ is the Q at termination R_L.

The spacings between the inner sets of posts are determined by running eigen-mode analyses in CST MWS. Adjacent posts are placed between two resonant waveguide cavities in CST MWS, as depicted in Figure 5.10, with the eigenmode solver calculating the resonant frequencies as the spacing is varied.
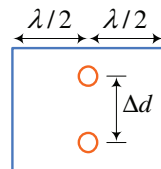
Figure 5.10: CST MWS Eigenmode Solver Setup for Waveguide Filter

These resonant frequencies can be used to calculate the resultant coupling strength

$$k \quad = \quad \frac{f_e^2 - f_m^2}{f_e^2 + f_m^2} \tag{5.4.5}$$

where f_e is the electric resonant frequency and f_m is the magnetic resonant frequency. This is used to determine the spacing between posts required to obtain the coupling strength calculated using Equation 5.4.3.

The spacings between the outer sets of posts are determined by running frequency domain analyses in CST MWS. Adjacent posts are placed in a non-resonant waveguide cavity in CST MWS, as depicted in Figure 5.11, a half-wave distance from one edge and an irregular distance from the second edge. By sweeping the spacing between the posts, the frequency-domain solver calculates the loaded Q factor at the second edge, which is used to determine the spacings between the posts required to obtain the Q factor calculated using Equation 5.4.4.
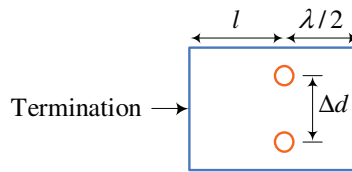
Figure 5.11: CST MWS Frequency Domain Solver Setup for Waveguide Filter

Waveguide filters are easily tuned by changing the size of the resonant cavities. This is achieved in practice by drilling screws in the middle of each of the three resonators and between the end resonators and the terminations, with the filter tuned by changing the depth of the screws into the cavities. The tuning screws are incorporated in the simulation in order to account for the whole design.

Once all the required parameters of the filter have been calculated, the filter can be constructed in CST MWS, with frequency-domain analyses performed to optimise the design. The optimisation process is simple, with few input parameters and lenient specifications. Also, the full-wave analyses are sped up by making use of the planes of symmetry of the structure along both axes.

The CST MWS results of the waveguide filter are depicted in Figure 5.12. It is seen from the narrow band result of the left graph that the filter is well matched at 42GHz to pass the wanted oscillator signal to the mixer, and from the wide band result of the right graph any unwanted signal below 35GHz would be attenuated by at least 65dB. The reflection coefficient is truncated at the theoretical cut-off frequency of the waveguide.
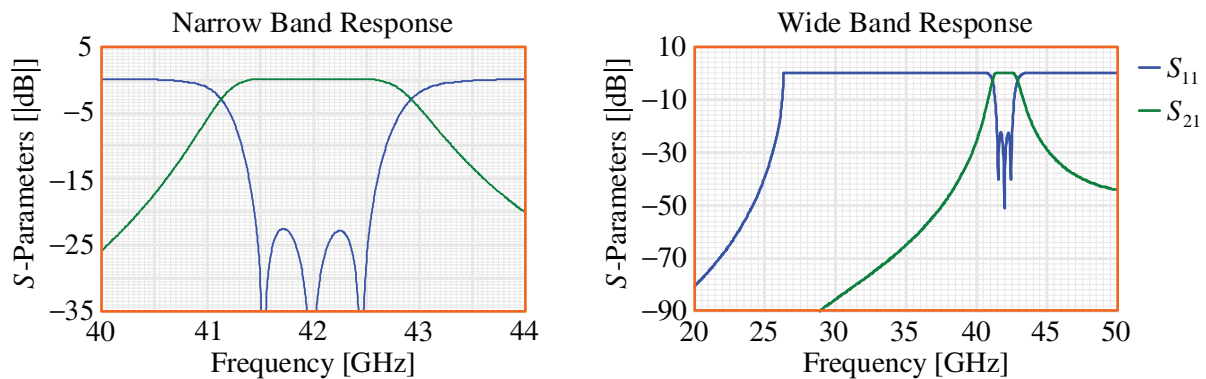
Figure 5.12: CST MWS Simulated Coupled-Post Filter Response

The filter is constructed out of a length of WR-22 waveguide [33], with specifications presented in Table 5.6. Holes are drilled into the waveguide at the appropriate distances to admit the inductive posts, with diameter 0.50mm, and the tuning screws, with diameter 1.60mm. Square WR-22 flanges (QuinStar QFF-QB599) [33] are soldered to either end of the waveguide to connect to the oscillator and mixer. Technical drawings of the waveguide filter are shown in Appendix A.4.

Table 5.6: QuinStar QWR-Q20000 Waveguide Specifications

Parameter	Value	Parameter	Value
Inner Broad Wall	5.690mm	Inner Narrow Wall	2.845mm
Outer Broad Wall	7.722mm	Outer Narrow Wall	4.877mm

The filter is connected via waveguide to 2.4mm coaxial adapters (QWA-22S24F) [33] to perform two port measurements on a network analyser [43], as depicted in Figure 5.13. The suppression of the 25GHz signal is greater than 60dB and falls below the noise floor of the network analyser, while the attenuation of the 42GHz oscillator is 4dB.
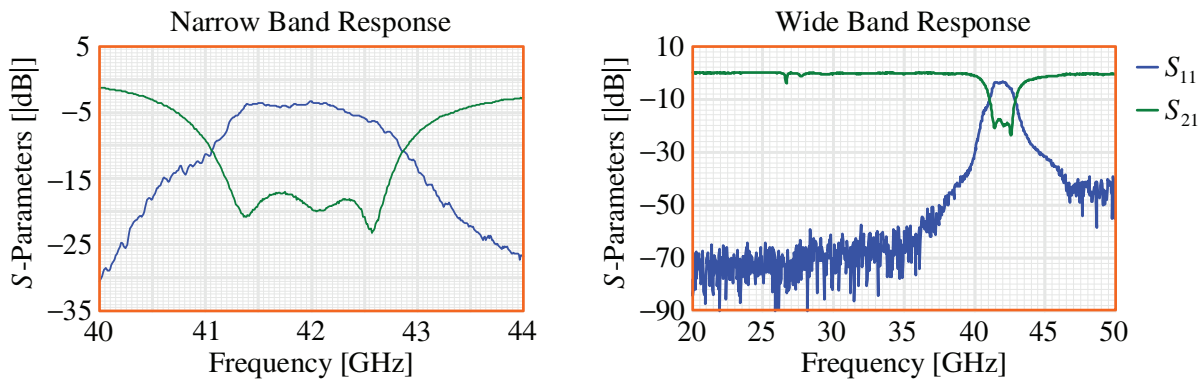
Figure 5.13: Measured Coupled-Post Filter Response

In order to test the effect of the waveguide filter, power measurements using a spectrum analyser [50] are once again performed on the down-converter. Like before, the RF input of the mixer is connected to a matched waveguide load, but this time the waveguide filter is connected between the LO and the mixer. The output of the mixer still contains spurious signals, but at reduced levels, as depicted in Figure 5.14.
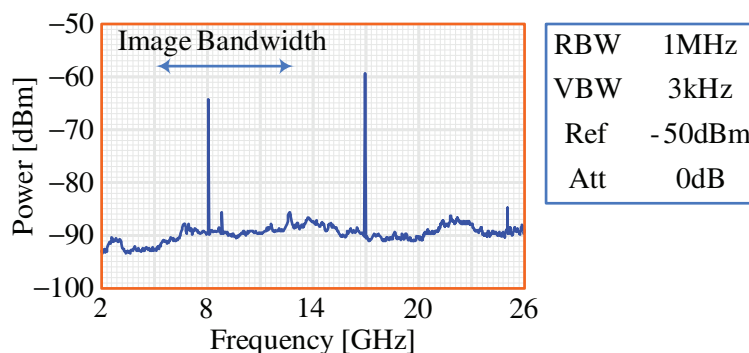
Figure 5.14: Mixer Output Spectrum with Waveguide Filter

It is clear that the spurious signal at 8.8GHz is attenuated by a significant amount, but that the signal at 8.2GHz remains almost unaffected. Clearly, this signal is cause by the interaction between the 42GHz signal and the mixer, and can therefore not be mitigated. In the system design, care should therefore be taken not to saturate the system as a result of this spurious signal.

The spurious signals that fall outside of the IF frequency range, but still fall within the frequency range of the IF amplifier, can safely be suppressed using a filter between the mixer and the IF amplifier. However, the same cannot be done for the spurious signals that fall within the IF frequency range as this would attenuate the wanted MMW emissions. The implemented solution involves calibrating out these signals, as described in Section 5.6, with little loss of data as these signals fill a small portion of the whole band of a channel.

5.5 Amplifier

As described in Section 5.2, the power level of the MMW emissions at the input to the detectors must be kept within a range of ±10dB around -10dBm. As the power level of the captured MMW emissions are very low, a significant amount of amplification is needed to meet this requirement. Assuming that the MMW emissions and the components of the radiometer are frequency independent within the specified frequency ranges, the simplified system used to calculate the required amplification per channel is depicted in Figure 5.15. The calculations are simplified by modelling the antenna as a lossless antenna followed by a lossy line.
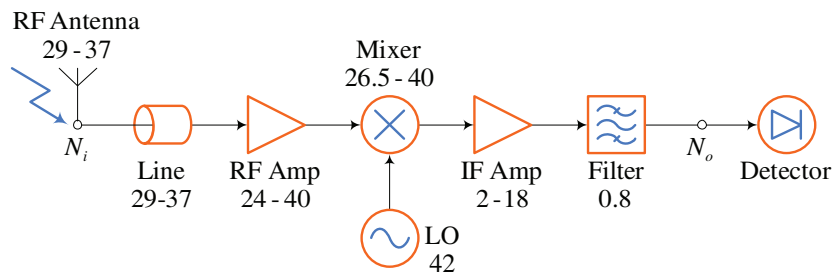
Figure 5.15: Channel Block Diagram used for Amplification Calculation

The noise characterisation parameters of the various components in the system are presented in Table 5.7, with the temperature T of each component given by $T = (F - 1)T_0$, where T_0 is the physical temperature and is approximated as 290K. As this section is dedicated to the calculation of the required amplification gain, these gain values will be determined at a later stage. However, the Noise Figure (NF) of the amplifiers can be approximated as 3dB as this is the average value for the majority of amplifiers at various frequency ranges [32, 33].

Table 5.7: Noise Characterisation Parameters of Radiometer

Component	Gain	Loss	Noise Figure	Temperature
Antenna	-1dB	1dB	1dB	75K
RF Amplifier			3dB	289K
Mixer	-6dB	6dB	6dB	864K
IF Amplifier			3dB	289K
Channel Filter	-10dB	10dB	10dB	2610K

The output noise power N_o at the input to the detector is

$$N_o \quad = \quad kB\left(T_D + T_S\right)G_s \tag{5.5.1}$$

where k is Boltzmann's constant, $B = 800\text{MHz}$ is the bandwidth of the channel, T_D is the detected temperature of the objects within the target area, T_S is the system noise temperature and G_s is the system gain.

As discussed in Chapter 2, the detected temperature of a room temperature object that fills the main beam of the antenna pattern would cover a range from $\approx 100\text{K}$ for a perfect reflector in clear weather to $\approx 300\text{K}$ for a perfect radiator or for an object separated by highly unfavourable weather conditions.

The system noise temperature is

$$T_S \quad = \quad T_1 + \frac{T_2}{G_1} + \frac{T_3}{G_1 G_2} + \dots \tag{5.5.2}$$

where T_i is the temperature of component i and G_i is the gain of component i. As the amplifier will have a large gain, the system noise temperature can be approximated by the first two terms

$$T_S \quad \approx \quad T_1 + \frac{T_2}{G_1} \quad = 438\text{K} \tag{5.5.3}$$

The system gain required to obtain at output noise power centred around -10dBm for an object with a detected temperature centred around 200K is

$$G_s \quad = \quad \frac{N_o}{kB(T_A + T_S)} \quad = \quad 71.35\text{dB} \tag{5.5.4}$$

thereby requiring an amplifier gain of 88.35dB to compensate for the loss of the antenna, mixer and multiplexer.

As this is a large amount of amplification, especially as it is required for a wide band, in this work a three-stage amplifier increases the weak detected signal, as depicted in Figure 5.1. The first stage is a Low-Noise Amplifier (LNA) [33] connected between the antenna and the mixer. This amplifier strengthens the weak detected signal at the RF range. The specifications of the low noise amplifier are presented in Table 5.8.

Table 5.8: QuinStar QLW-24403520-GG Low Noise Amplifier Specifications

Parameter	Value
Frequency Range	24GHz to 40GHz
Noise Figure	$3.5\text{dB}_{\text{max}}$
Gain	20dB

The second and third stage are ultra-broadband amplifiers [32] connected between the mixer and the multiplexer. These amplifiers strengthen the down-converted signal at the IF range. The specifications of the two IF amplifiers are presented in Table 5.9.

Table 5.9: Lucix S020180L3201 Amplifier Specifications

Parameter	Value
Frequency Range	2GHz to 18GHz
Noise Figure	$2.8\text{dB}_{\text{max}}$
Gain	32dB_{min}

5.6 Calibrations

As discussed in Section 5.5, the output noise power at the input to the detectors are a combination of the detected temperature of the objects within the target area and the noise temperature of the system

$$N_o \;=\; kB\left(T_D + T_S\right)G_s \;=\; aT_D + b \tag{5.6.1}$$

As there is a linear relationship between the output noise power and the detected temperature of the objects within the target area, the detected temperature can be extracted from the output noise power by calculating the constants a and b by calibrating the system to two known temperature sources, T_1 and T_2, as depicted in Figure 5.16.
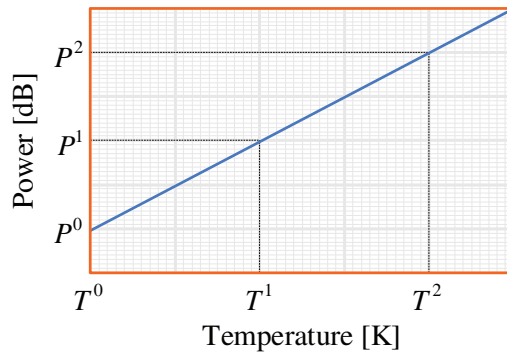
Figure 5.16: Calibration of Radiometer

The first calibration point is measured with the antenna pointed at the zenith of the sky when the sun is not in the detected range, with the Field of View (FOV) containing no land-based radiators. The first calibration temperature $T_D = T_1$ is determined from the prevailing weather conditions [90], as depicted in Figure 5.17.
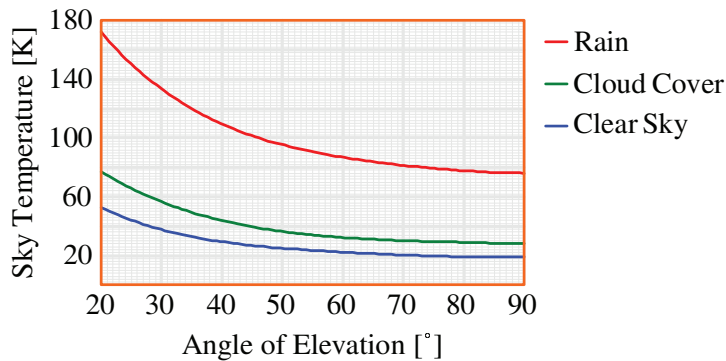
Figure 5.17: Sky Temperature at 35GHz

The depicted calculated values are for clear sky with water vapour content at sea level (7.5g/m^3), for uniform moderate cloud cover of between 900m and 1800m with a condensed water content of 0.3g/m^3 superimposed on condition one and for uniform moderate rain of between 0m and 900m with a precipitation rate of 4mm/hr superimposed on condition two, with all three at a sea-level temperature of 290K.

The second calibration point is measured with the FOV of the antenna enclosed with microwave absorbing material [46]. This sets the second calibration temperature $T_D = T_2$ to ambient temperature, which is approximated as room temperature $T_2 \approx 290K$.

From these two calibrations the constants a and b are

$$
\begin{aligned}
a &= \frac{N_1 - N_2}{T_1 - T_2} \\
b &= \frac{N_2 T_1 - N_1 T_2}{T_1 - T_2}
\end{aligned}
\tag{5.6.2}
$$

where N_1 is the power level obtained during the first calibration and N_2 is the power level obtained during the second calibration.

With the constants a and b known, the detected temperature of the objects within the target area can be extracted

$$
T_D = \frac{P - b}{a}
\tag{5.6.3}
$$

and the system gain and the system NF are calculated as

$$
\begin{aligned}
G_S &= \frac{a}{kB} \\
F_S &= \frac{b}{aT_O} + 1
\end{aligned}
\tag{5.6.4}
$$

This method is used to calibrate the imaging system for the far-field measurements performed in Chapter 3. These measurements were performed with output of the first IF amplifier directly connected to the spectrum analyser, with the second IF amplifier bypassed on account that the calculated value of the spurious signal of the LO-mixer at 16.9GHz would exceed the specified maximum RF input of the spectrum analyser.

A calibration was performed before each measurement because the two images were measured under different conditions, with the first calibration taken in the morning at an ambient temperature of 298K and the second calibration taken in the evening at an ambient temperature of 290K.

The calculated gain and noise figure are depicted in Figure 5.18. The gain is slightly less than the expected value of 45dB, and the noise figure is less than the expected 13.3dB. However, there is a good agreement between the two calibration.
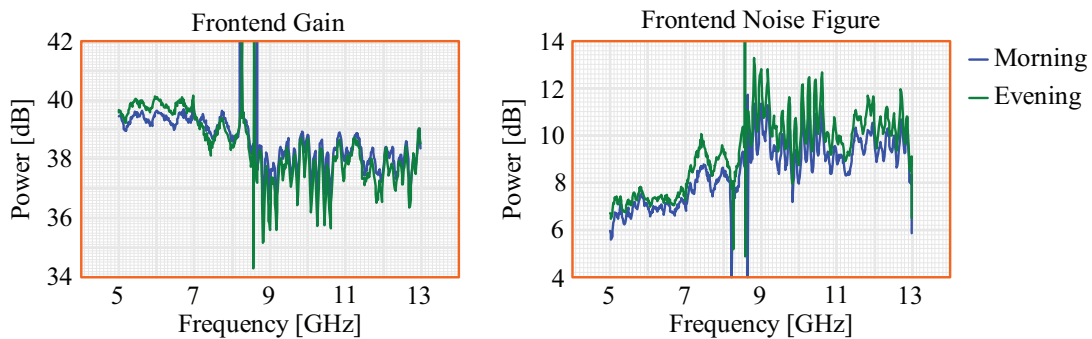
Figure 5.18: Calibration of Full Reflector Antenna Configuration

As it is assumed that the power-density spectrum of MMW emissions is approximately constant, theoretically any nonlinearity in the system can be compensated for. Therefore, the calibrated results can be used to remove the spikes at the output of the mixer and compensate for the mismatch at the common port of the multiplexer.

5.7 Measurements

As discussed in Chapter 3, the start of the far-field region of the antenna is approximately 100m from the antenna. While this poses no problem for the applications that this system is designed for, it does cause problems during the testing stages. It is virtually impossible to set-up a controlled environment around the antenna at such a large distance, and this is why the measurements of the imaging system are performed within the controlled environment of an anechoic chamber.

In Chapter 3 the antenna pattern at 2.5m from the antenna were computed to demonstrate that this distance is large enough for the far-field characteristics of the antenna pattern to start forming, that of a main beam that sweeps the target area as a function of frequency, even though the expected directivity of the far-field has not yet formed. This configuration can be used to test the imaging system.

The anechoic chamber contains two precision positioners. The one is fixed to the floor at the far end of the chamber and is capable of movings its load over a large two-dimensional grid. The other is fitted onto rails for freedom with movement along the 5m length of the chamber and is capable of rotating its load over a 360° range. By positioning the rotator at the desired distance away from the other positioner, a target area similar to that used in the simulations of Section 6.5 are realisable.

A waveguide horn [91] is used as the single frequency source of the target area. It is attached to the *xy* positioner and the antenna is loaded on the rotator, as depicted in Figure 5.19. The target area is generated by rotating the antenna, while keeping the horn fixed in the centre of the scan angle of the antenna and at a height in the centre of the bandwidth of the channel being measured and the source set to the centre frequency of the channel being measured.
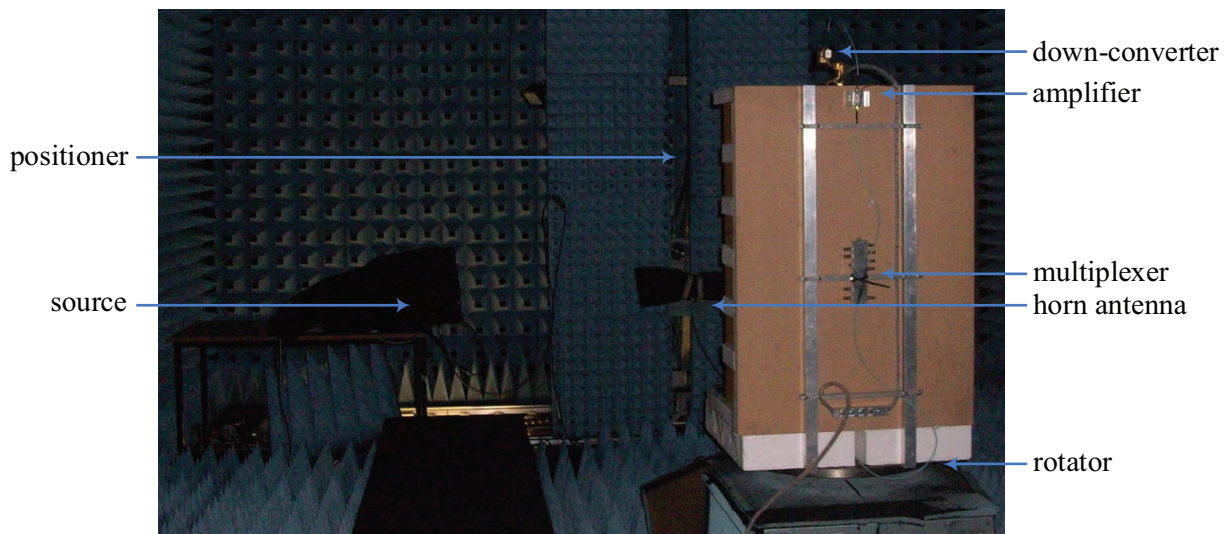
Figure 5.19: Near-Field Measurement Set-Up

As a source capable of supplying a frequency within the MMW region was not available, the source frequency was created using a source [88] operational at a lower frequency range that is amplified [92] and then doubled [93]. The doubling is a non-linear operation that resulted in spurious signals, which combined with the spurious signals of the down-converter to form a noisy spectrum within the image bandwidth, as depicted in the power measurements of the spectrum made using a spectrum analyser [50] of Figure 5.20.
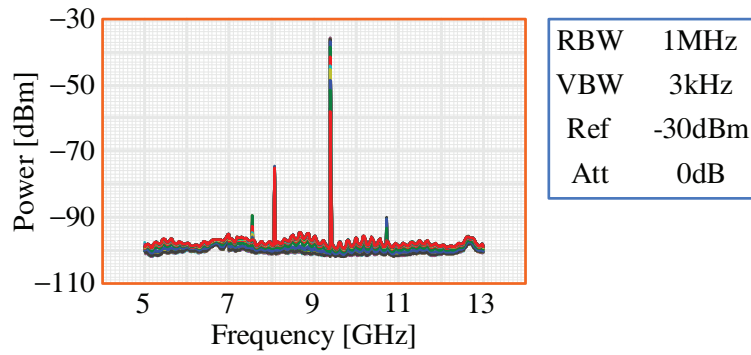
Figure 5.20: Spurious Signals within Image Bandwidth

The -35dBm signal at 9.4GHz to the desired signal, the -75dBm signal at 8.2GHz is caused by the interaction between the 42GHz signal to the LO and the mixer, with the two -90dBm signals at 7.6GHz and 10.7GHz are caused by the interaction between the spurious signals of the doubler and the mixer. Fortunately, the source can be set to a high enough power level so that the desired frequency dominates the image bandwidth.

The first measurement is performed to test the ability of the imaging system to detect a stationary object in the centre of a target are, while the antenna is swept across the target area. This is done by positioning the horn 0.53m above the centre of the reflector, with a 32.6GHz signal as its source, and rotating the antenna from $-15°$ to $+15°$ in $1°$ steps. The height of the horn is chosen to be at the orientation of the main beam at 32.6GHz, which is calculated as $12.0°$ using Equation 3.2.1.

As the response over the whole band is required, the output of the second IF amplifier is connected directly to the spectrum analyser, with the measurements depicted in Figure 5.21. As predicted by the 2D patterns depicted in Figure 3.29, the source is detected over a $9°$ range thereby blurring the image. If such a signal was divided into channels, the resulting image would mimic the simulated results of Chapter 6. However, as the source is a single point it is not detected by the neighbouring channels as would be expected for a wideband source.
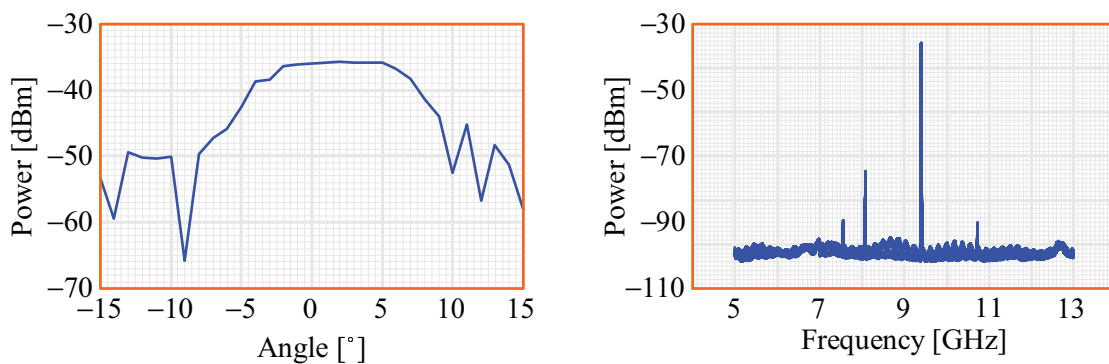
Figure 5.21: Measured Target Area containing Single Object

Such a signal can be used to obtain the position of an object in a target area. As the antenna pattern sweeps the target area as a function of frequency, by dividing the frequency range into bands the frequency range is divided into neighbouring portions of the target area. The image can be directly formed from these bands, thereby utilising the inherent space-to-frequency mapping of the antenna.

The second measurement is performed to test the ability of the imaging system to separate the frequency range into channels. This is done by moving the horn from -0.5m below the centre of the reflector to 1.5m above the centre of the reflector in 0.05m steps, with a 35.8GHz signal as its source, while keeping to antenna stationary in a position facing the horn. The detected signal should peak at 0.2m above the centre of the antenna, as the orientation of the main beam at 35.8GHz is calculated as 4.4° using Equation 3.2.1.

As the response in one channel is required, the output from the channel with a centre frequency of 6.2GHz is connected directly to the spectrum analyser, with the measurements depicted in Figure 5.22. As predicted by the 2D patterns depicted in Figure 3.29, the source is detected over a 0.2m range thereby blurring the image, with the peak signal detected around 0.2m above the centre of the antenna as calculated.
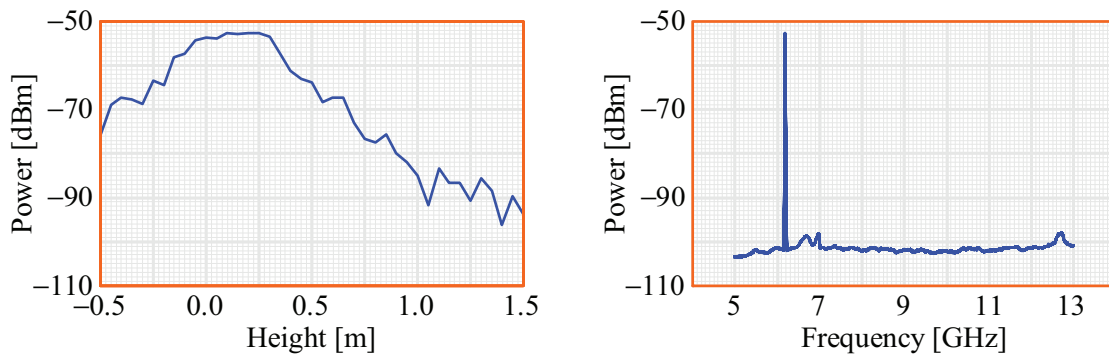
Figure 5.22: Measured Power in Channel Two for 35.8GHz Source

The second measurement is repeated, but this time with a 29.4GHz signal as the source of the horn. The detected signal should peak at 1.0m above the centre of the antenna, as the orientation of the main beam at 35.8GHz is calculated as 22.4° using Equation 3.2.1. However, the detected signal should be heavily attenuated as the output from the channel with a centre frequency of 6.2GHz should be isolated from such a signal.

The measurements are depicted in Figure 5.23. As predicted by the 2D patterns depicted in Figure 3.29, the source is detected over a 0.3m range thereby blurring the image, with the peak signal detected around 1.05m above the centre of the antenna as calculated. In comparing the two measurements performed during the second test the isolation of the channel from the 29.4GHz signal is evident in the 40dB difference between the peak value detected for the 35.8GHz source and the 29.4GHz source.
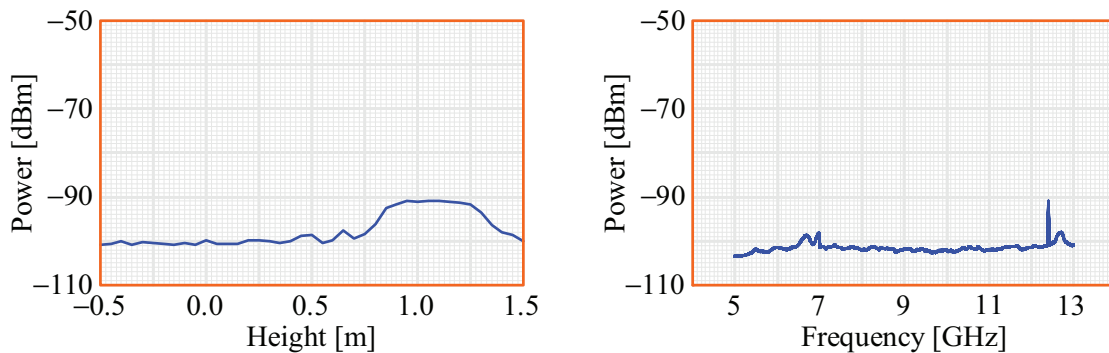
Figure 5.23: Measured Power in Channel Two for 29.4GHz Source

It can be seen from the measurements in this section that this Passive Millimetre-Wave (PMMW) imaging system can be used to accurately determine the position of an object along the plane perpendicular to the flight path in the target area based on the inherent space-to-frequency mapping of the main beam of the antenna. Also, the multiplexer channels are isolated from each other, which potentially could have been a problem because of the wide band of the frequency range. However, the position of an object is blurred along the plane of the flight path, thereby requiring a post processor to reconstruct the image.

5.8 Conclusion

In this chapter the analogue components of the radiometer are discussed. The primary function of these components is to be able to perform measurements on the MMW emissions that are incident at the antenna. As affordable, commercially available detectors operate at a much lower frequency range than that of the MMW emissions, a heterodyne system is required to down-convert the emissions to the desired frequency range.

As a PMMW imaging system form images from thermal MMW emissions the power level of the signals are very low. This causes two problems for these analogue devices. Firstly, the radiometer requires a large amount of amplification to strengthen the signals to the level of the input dynamic range of the detectors. This is achieved by making use of three amplifiers divided between the RF range and the IF range.

Secondly, the output of the down-converter contains spurious signals within the image bandwidth that dominate the images. These spurious signals are the products of the two signals present within the LO, the desired oscillation frequency and a leakage signal. While a filter has been incorporated between the LO and the mixer to attenuate the leakage signal, the image bandwidth is still populated with spurious signals, though with lower power levels.

This chapter concludes the frontend of the PMMW imaging system. The remaining chapter deals with the post-processor that is developed to deal with the blurred main beam of the antenna pattern.

Chapter 6

Post-Processor

6.1 Introduction

The design of the Passive Millimetre-Wave (PMMW) imaging system is severely limited by the size of the Unmanned Aerial Vehicle (UAV), particularly in the inability to incorporate any form of optical or mechanical scanning antenna, thereby requiring an antenna with a main beam with a scan that is electronically controlled. In using the motion of the UAV to scan along the plane of the flight path, the antenna is only required to scan along the plane perpendicular to the flight path.

The antenna displays a narrow, high gain, frequency-scanned beam along the plane perpendicular to the flight path, but a very broad beam along the plane of the flight path that leads to a larger area than the target area being detected, as depicted in Figure 6.1. When flying over the target area the image of an object is blurred along the plane of the flight path, making it difficult to accurately determine the position of an object or to differentiate between objects situated along the plane of the flight path.
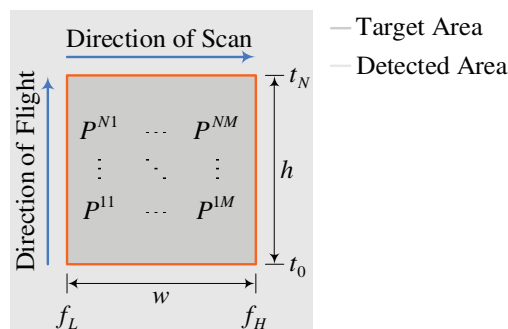
Figure 6.1: Target Area

Prevention of object blurring is impossible as the size of the UAV precludes the use of bulky optics to focus the antenna pattern along the plane of the flight path as well. The only solution is to reconstruct the target area from the blurred image. This dissertation proposes a technique of image reconstruction based on the Kalman filter to reconstruct an accurate image of the target area from such a detected signal [1, 2]. It is shown that the Kalman filter is able to successfully reconstruct the image using the measured antenna pattern to model the scanning process and reverse the blurring effect.

6.2 Iterative Filter

Image degradation is conventionally defined in literature as the combination of blurring of the edges between the regions of an image and the addition of random noise to the image

$$z \;=\; G_{\sigma_b} * x + n \qquad (6.2.1)$$

where x is the actual image, z is the measured image, $G_\sigma(x_b)$ is a Gaussian function of standard deviation σ_b that blurs the edges between the regions of an image and n is Gaussian noise of standard deviation σ_n that adds random spikes to the image, as depicted in the 100 pixel images of Figure 6.2.
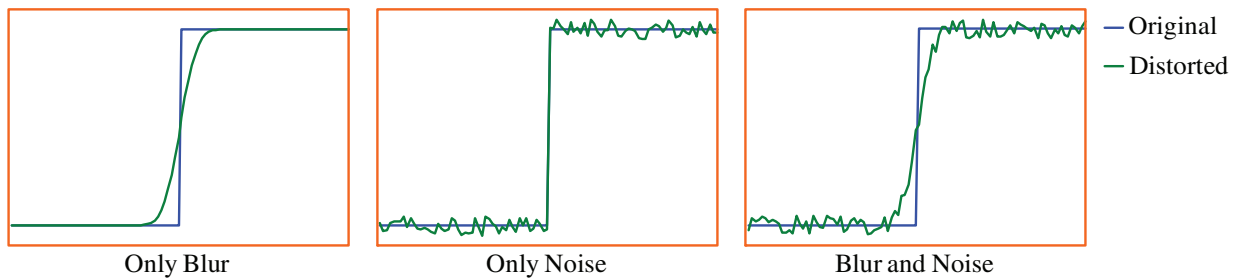
Figure 6.2: Image Degradation

The conventional methodology of image reconstruction is to invert the effect of the degradation. If a lowpass filter is used to denoise an image, the edges between the regions are further blurred, as both noise and edges are high frequency components of the image. Therefore, as blurring and noising have opposing effects on the image, the reconstruction algorithm must balance deblurring and denoising to reconstruct the original image.

The simplest form of image denoising is the usage of grid filter to obtain an average value for each pixel. As the noise is assumed to be of a Gaussian nature with zero mean, by obtaining the mean value of a number of samples, $\bar{n}$, the noise will be averaged out, leaving just the original image, as depicted for an average of 11 pixels in Figure 6.3.
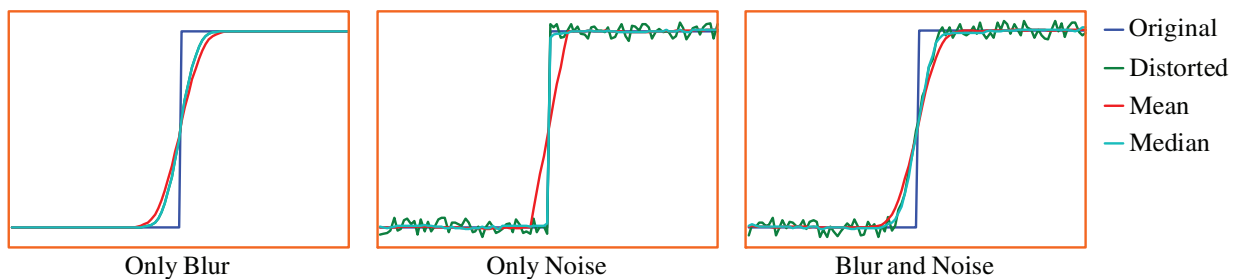
Figure 6.3: Grid Filter

Similarly, the simplest form of image deblurring is the usage of grid filter to obtain a median value for each pixel. As blur is assumed to just affect pixels near the edge of a region, the middle value of an ordered set of pixels around each pixel would restore the blurred pixel to the value of the region, as depicted for a median of 11 pixels in Figure 6.2.

As can be seen, while the mean filter removes noise and the median filter restores edges the opposite is not true. The mean filter enhances blur between regions and the median filter retains the noise. Therefore, a mechanism is required that can distinguish between regions requiring denoising and edges requiring deblurring. The conventional methodology uses algorithms containing iterative Partial Differential Equations (PDEs)

$$z_{k+1} = z_k + \Delta t \frac{\partial z_k}{\partial t} \tag{6.2.2}$$

where $z|_{t=0} = z$ is the initial condition, Δt is the algorithm step size and the reconstruction method is determined by the formulation of the PDE. These algorithms analyse the derivative of the image to differentiate between regions and edges.

6.2.1 Diffusion

The axiomatic approach to denoise an image requires linearity, spatial shift invariance, isotropy and scale invariance [94]. The unique operator that obeys these requirements is convolution with a Gaussian kernel. The canonical image denoising algorithm of isotropic diffusion is equivalent to a smoothing process with a Gaussian kernel

$$\frac{\partial z}{\partial t} = \text{div}\left[c_n\left(\nabla z\right)\nabla z\right] \tag{6.2.3}$$

where $z|_{t=0} = z$ is the initial condition and $c_n\left(\nabla z\right) = 1$.

Isotropic diffusion contains no mechanism to differentiate between regions in an image and diffuses the image as a whole. As $t \to \infty$ the edges between regions and smeared and the restored image approaches a homogeneous value, as depicted in Figure 6.4.
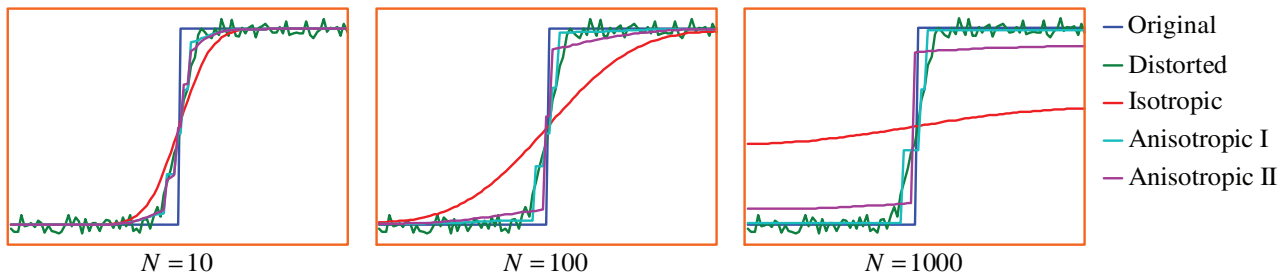
Figure 6.4: Diffusion

Anisotropic diffusion [94] was introduced in order to locate and diffuse regions separately while maintaining sharp edges by constructing a nonlinear adaptive denoising process from Equation 6.2.3 by reformulating $c_n\left(\nabla z\right)$ as a positive decreasing function of the gradient magnitude

$$c_n\left(\nabla z\right) = \exp\left[-\left(\frac{|\nabla z|}{\alpha}\right)^2\right] \tag{6.2.4}$$

$$c_n\left(\nabla z\right) = \left[1 + \left(\frac{|\nabla z|}{\alpha}\right)^2\right]^{-1} \tag{6.2.5}$$

where α is a constant. The improvement of anisotropic diffusion over isotropic diffusion is depicted in Figure 6.4 for both formulations of $c_n\left(\nabla z\right)$. The edges between regions are sharpened, while the detail within the regions is still diffused.

The literature contains other reformulations of $c_n(\nabla z)$ that improve the ability of the algorithm to handle the contradictory requirements of deblurring and denoising. Examples include incorporation of forward and backward diffusion [95] and the addition of an imaginary term that acts at the edge detector to the real part [96].

6.2.2 Variation

The variational approach to denoise an image derives a diffusion-like PDE by a functional minimisation process. The equilibrium state of an energy functional, $E(z)$, is sought based on the calculus of variations defined Euler-Lagrange equation

$$\frac{\delta E(z)}{\delta z} = 0 \tag{6.2.6}$$

that is used to construct an evolutionary process that dissipates energy.

When the energy functional is defined as

$$E(z) = \int \left[c_n(\nabla z) + \tfrac{1}{2}\lambda(x-z)^2 \right] dxdy \tag{6.2.7}$$

the minimisation of this functional using a gradient descent method leads to the canonical variational denoising algorithm known as the Total Variation (TV) minimising algorithm [97]

$$\frac{\partial z}{\partial t} = \operatorname{div}\left[c_n'(\nabla z) \frac{\nabla z}{|\nabla z|} \right] - \lambda(x-z) \tag{6.2.8}$$

where $z|_{t=0} = z$ is the initial condition, $c_n'(\nabla z) = 1$ and λ is a scalar controlling the fidelity of the solution to the measured image z

$$\lambda = \frac{1}{\sigma^2} \int \operatorname{div}\left[c_n'(\nabla z) \frac{\nabla z}{|\nabla z|} \right] (x-z)\, dxdy \tag{6.2.9}$$

formulated to finding the minimum with regards to the actual image x.

The globally defined scalar λ results in fine detail being diffused, as depicted in Figure 6.5.
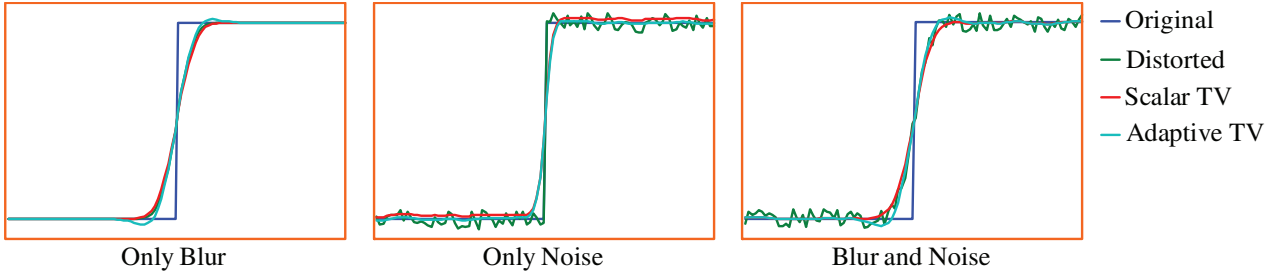
Figure 6.5: Total Variation

Adaptive total variation [98] was introduced in order to preserve texture by locally reformulating λ

$$\lambda = \frac{\operatorname{div}\left[c_n'(\nabla z) \frac{\nabla z}{|\nabla z|} \right](x-z)}{\operatorname{var}(x-z)} \tag{6.2.10}$$

where $c_n'(\nabla z) = \frac{\nabla z}{\sqrt{1+\nabla z^2}}$. The locally defined λ results in each region being denoised separately to improve the detail retention during denoising, as depicted in Figure 6.5.

The literature contains reformulations of the total variation model that improve the ability of the algorithm to distinguish between noise that must be blurred and texture that must be retained. Examples include regularising the algorithm with an anisotropic diffusion term [99] and dividing the algorithm into two sequential steps that each handle a different function [100].

6.2.3   Shock Filter

The canonical image deblurring algorithm is the hyperbolic shock filter algorithm [101] that behaves similarly to deconvolution

$$\frac{\partial z}{\partial t} \quad = \quad -\text{sign}\left[c_b\left(z_{\eta\eta}\right)\right]\left|\nabla z\right| \tag{6.2.11}$$

where $z|_{t=0} = z$ is the initial condition, η is the direction parallel to the gradient and $c_b\left(z_{\eta\eta}\right) = z_{\eta\eta}$.

The edges are sharpened by developing shocks at inflection points (zero crossings of second derivative). The shock filter is sensitive to noise as noise adds an infinite number of inflection points to the image, disrupting the process and resulting in any noise in the image being enhanced, as depicted in Figure 6.6.
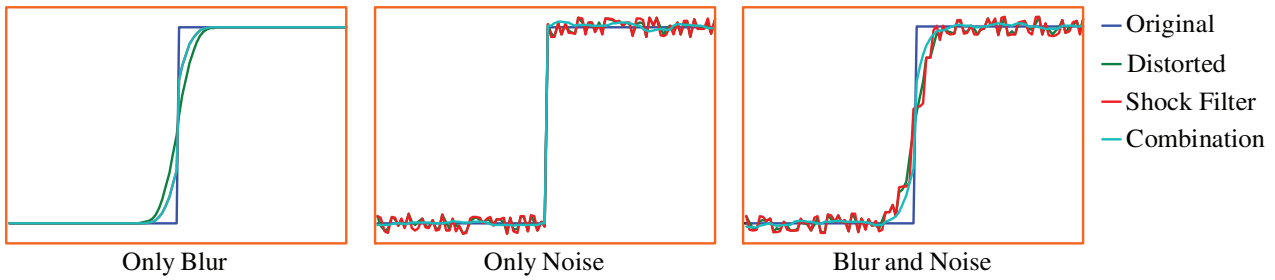
Figure 6.6: Shock Filter

The combination of the diffusion of Equation 6.2.3 and the shock filter of Equation 6.2.11 was introduced in order to increase robustness to noise by controlling the shock filter with a smoothed second derivative [102]

$$\frac{\partial z}{\partial t} \quad = \quad \text{div}\left[c_n\left(\nabla z\right)\nabla z\right] - \text{sign}\left[c_b\left(z_{\eta\eta}\right)\right]\left|\nabla z\right| \tag{6.2.12}$$

where

$$\text{div}\left[c_n\left(\nabla z\right)\nabla z\right] \quad = \quad \alpha_n z_{\xi\xi} \tag{6.2.13}$$

$$c_b\left(z_{\eta\eta}\right) \quad = \quad G_\sigma * z_{\eta\eta} \tag{6.2.14}$$

α_n is the denoising constant and ξ is the direction perpendicular to the gradient. The improvement of this combination over the shock filter is depicted in Figure 6.6. The noise is now diffused at a lose of edge sharpness.

The literature contains other combinations of diffusion and the shock filter that improve the ability of the algorithm to differentiate between regions and edges. Examples include improved control over the shock filter to prevents shocks been developed in the presence of noise inside regions using an externally control parameter [103] or an internally calculated term [96].

6.2.4   Review

The image reconstruction algorithms of diffusion, variation and the shock filter are solved using the numerical methods of Appendix B. In order to maintain the size of the image the input to the PDEs is required to be larger than the size of the image. This is done by extending the borders of the image by one pixel.

All of the above image reconstruction processes deal with localised object blurring modelled by Gaussian noise, which is insufficient to counter the more global object blurring of the antenna pattern, and are designed for stationary stand-alone images. For the problem at hand an unconventional technique is required that uses the unfocused antenna pattern to model the blur and is designed for non-stationary processes.

6.3   Recursive Filter

A perfect imaging system has a beam focused on a portion of landmass equal in size to a pixel, resulting in a one-to-one relationship between the target area and the detected image. However, no practical imaging system is perfect. Conventional image blurring caused by an imperfectly focused lens smoothes an image's edges between regions, as depicted in Figure 6.7, making it hard to distinguish between regions.
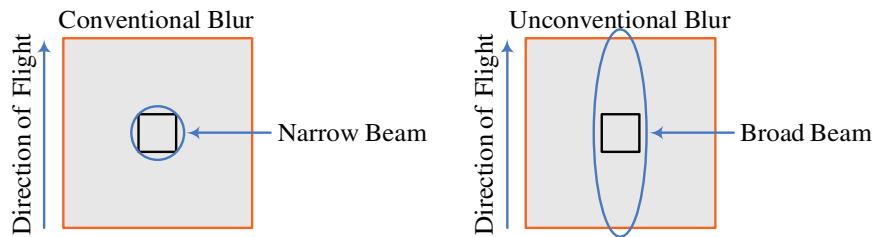
Figure 6.7: Image Blur

In the proposed application the blurring problem is magnified significantly, as there is a many-to-one relationship between the target area and the detected signal, due to the very broad beam of the antenna. Each pixel of the image incorporates data from a large portion of landmass within the target area and a large portion of landmass outside of the target area, as depicted in Figure 6.7.

While the conventional methodology of image restoration to invert the effect of the degradation holds true, the conventional techniques of diffusion, variation and the shock filter discussed in Section 6.2 cannot be used as they deal with localised object blurring modelled by Gaussian noise, which is insufficient to counter the global object blurring of the antenna pattern.

This dissertation proposes a new unconventional technique [1, 2] based on the Kalman filter [34], that uses the unfocused antenna pattern to model the blur and incorporates the flight of the UAV. For each time-interval the Kalman filter makes a prediction of the detected signal using the measured antenna pattern. The comparison between the predicted signal and the detected signal is used to generate an image of the target area.

The Kalman filter is a set of mathematical equations that estimate a process by using feedback control, as depicted in Figure 6.8. The time update equations projecting forward in time the current state estimate to the next time step and then the measurement update equations obtain feedback in the form of noisy measurements to adjust the projected estimate to obtain an improved estimate.
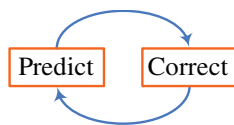
Figure 6.8: Kalman Filter Predictor-Corrector Cycle

The Kalman filter supports estimations of past, present and future states even when the precise nature of the modelled system is unknown. Advances in digital computing and the simplistic and robust nature of the Kalman filter has led to extensive research [104, 105] and application [106, 107] of the Kalman filter, particularly in the area of autonomous navigation [108, 109, 110].

For example, given a vessel lost at sea with only a captain's log and a mariner's astrolabe to guide the crew from island A to island B, as depicted in Figure 6.9. The captain's log records the estimated speed of the vessel through the water by measuring the length of log-line that passes over the stern during a fixed period of time. The astrolabe determines the latitude of the vessel by measuring the sun's noon altitude.
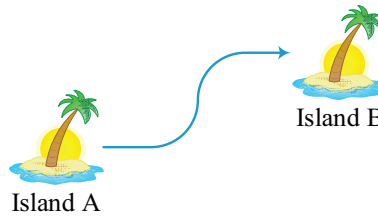
Figure 6.9: Kalman Filter Example – Island Hopping

Both measurements are flawed. The log does not give an exact measure of speed due to such unknowns as the effect of currents and the stretch of the line nor does it not give the direction of the vessel. While the astrolabe gives the latitude, it does not give the longitude. Therefore, neither the log nor the astrolabe can conclusively pinpoint the vessel's position, and are therefore used in conjunction to map the vessel's route, as depicted in Figure 6.10
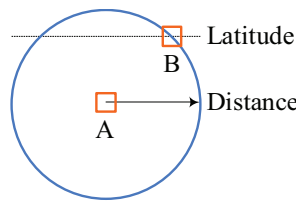
Figure 6.10: Kalman Filter Example – Position Determination

Given that the position of the vessel at noon the day before is given by point A, the new position of the vessel can be determined by calculating the distance travelled by the vessel using the log (given by the circle centred around point A) and by determining the latitude of the vessel at noon on the current day using the astrolabe (given by the dotted line). The position of the vessel is given by the point at which these two measurements meet up, at point B.

This system can be controlled by a Kalman filter, where the time update equations work with the captain's log and the measurement update equations work with the mariner's astrolabe. The current position of the vessel, x_{k+1}, can be predicted from the linear relationship between the last position of the vessel, x_k, and the distance travelled by the vessel A_k since the last position

$$x_{k+1} = A_k x_k \tag{6.3.1}$$

where the distance travelled is calculated from the speed of the vessel and the time since the last measurement.

Also, the current position of the vessel, x_{k+1}, can be predicted from the current astrolabe measurement, z_{k+1}

$$z_{k+1} = H_{k+1} x_{k+1} \tag{6.3.2}$$

The combination of these two equations is used to determine the position of the vessel.

6.3.1 Recursive State Estimation

The Kalman filter is used to model a variety of processes, working with large data sets and has been extended by the Extended Kalman Filter (EKF) [111], the Unscented Kalman Filter (UKF) [104] and other derivatives to support non-linear relationships between parameters. While the linear form of the Kalman filter is used in this work, the equations are derived from the more generalised form as follows.

A non-stationary, discrete-time, stochastic process $\mathbf{x}_{k+1} \in \Re^n$ is modelled as

$$\mathbf{x}_{k+1} = \mathbf{f}(\mathbf{x}_k, \mathbf{u}_k, \mathbf{v}_k) \tag{6.3.3}$$

where $\mathbf{u}_k \in \Re^l$ is the external control that drives the process from the state $\mathbf{x}_k$ to the state $\mathbf{x}_{k+1}$ and $\mathbf{v}_k$ is the process model inaccuracies plus process noise.

The state $\mathbf{x}_k$ is only accessible from the noise contaminated measurement $\mathbf{z}_k \in \Re^m$ modelled as

$$\mathbf{z}_k = \mathbf{h}(\mathbf{x}_k, \mathbf{w}_k) \tag{6.3.4}$$

where $\mathbf{w}_k$ is the measurement model inaccuracies plus measurement noise.

Recursive state estimation consists of iteratively reconstructing the state $\mathbf{x}_k$ from the process model $\mathbf{f}$, the measurement model $\mathbf{h}$ and the measurement $\mathbf{z}_k$. The process model inaccuracies and process noise are removed by comparing the actual process with the modelled process, with the measurement model inaccuracies and measurement noise removed by comparing the actual measurement with the modelled measurement.

The a priori estimate $\mathbf{x}_{k+1|k} \in \Re^n$ of the state $\mathbf{x}_{k+1}$ is given by the expectation

$$\mathbf{x}_{k+1|k} = E\left[\mathbf{f}(\mathbf{x}_k, \mathbf{u}_k, \mathbf{v}_k)\,|\mathbf{Z}^k\right] \tag{6.3.5}$$

where $\mathbf{x}_{i|j}, i \geq j$ is the estimate of the state $\mathbf{x}_i$ using the measurements $\mathbf{Z}^j = \{\mathbf{z}_0, \ldots, \mathbf{z}_j\}$ up to and including time j and is obtained from the noise-free version of the process model of Equation 6.3.3, the a posteriori state estimate $\mathbf{x}_{k|k}$ and the external control $\mathbf{u}_k$

$$\mathbf{x}_{k+1|k} = \mathbf{f}\left(\mathbf{x}_{k|k}, \mathbf{u}_k, \mathbf{0}\right) \tag{6.3.6}$$

The noise-free a priori estimate $\mathbf{z}_{k+1|k}$ of the measurement $\mathbf{z}_{k+1}$ is obtained by combining the measurement model of Equation 6.3.4 and the noise-free a priori state estimate $\mathbf{x}_{k+1|k}$

$$\mathbf{z}_{k+1|k} = \mathbf{h}\left(\mathbf{x}_{k+1|k}, \mathbf{0}\right) \tag{6.3.7}$$

The a posteriori state estimate $\mathbf{x}_{k+1|k+1} \in \Re^n$ is obtained from the a priori state estimate $\mathbf{x}_{k+1|k}$ and the weighted difference between the actual the measurement $\mathbf{z}_{k+1}$ and the a priori measurement estimate $\mathbf{z}_{k+1|k}$

$$\mathbf{x}_{k+1|k+1} = \mathbf{x}_{k+1|k} + \mathbf{K}_{k+1}\left(\mathbf{z}_{k+1} - \mathbf{z}_{k+1|k}\right) \tag{6.3.8}$$

where the $n \times m$ matrix $\mathbf{K}_{k+1}$ is the Kalman gain.

The choice of the Kalman gain $\mathbf{K}_{k+1}$ is made to meets some optimality criteria. In the case of the Kalman Filter, the stochastic nature of the process and measurement dynamics is taken into account in the derivation of the Kalman gain to produce an optimal linear estimator that minimises the a posteriori error covariance $\mathbf{P}_{k+1|k+1}$, the squared error on the expected value of the state estimate $\mathbf{x}_{k+1|k+1}$.

6.3.2   Linear Kalman Filter

For linear systems the process model of Equation 6.3.3 and the measurement model of Equation 6.3.4 become

$$\mathbf{x}_{k+1} \quad = \quad \mathbf{A}_k \mathbf{x}_k + \mathbf{B}_k \mathbf{u}_k + \mathbf{v}_k \tag{6.3.9}$$

$$\mathbf{z}_k \quad = \quad \mathbf{H}_k \mathbf{x}_k + \mathbf{w}_k \tag{6.3.10}$$

where the $n \times n$ matrix $\mathbf{A}_k$ relates the state $\mathbf{x}_k$ at time step k to the state $\mathbf{x}_{k+1}$ at time step $k+1$ in the absence of both the external control $\mathbf{u}_k$ and the process noise $\mathbf{v}_k$, the $n \times l$ matrix $\mathbf{B}_k$ relates the external control $\mathbf{u}_k$ to the state $\mathbf{x}_k$ and the $m \times n$ matrix $\mathbf{H}_k$ relates the state $\mathbf{x}_k$ to the measurement $\mathbf{z}_k$.

The process noise $\mathbf{v}_k$ and the measurement noise $\mathbf{w}_k$ are independent of each other, additive, zero-mean, white and Gaussian with normal probability distributions

$$\begin{aligned} p(\mathbf{v}_k) &\sim \mathcal{N}(\mathbf{0}, \mathbf{Q}_k) \\ p(\mathbf{w}_k) &\sim \mathcal{N}(\mathbf{0}, \mathbf{R}_k) \end{aligned} \tag{6.3.11}$$

where $\mathbf{Q}_k = E\left[\mathbf{v}_k \mathbf{v}_k^T\right]$ is the process noise covariance, $\mathbf{R}_k = E\left[\mathbf{w}_k \mathbf{w}_k^T\right]$ is the measurement noise covariance and $E\left[\mathbf{v}_k \mathbf{v}_n^T\right] = 0 = E\left[\mathbf{w}_k \mathbf{w}_n^T\right], n \neq k$.

From the process model of Equation 6.3.9, the noise-free a priori state estimate $\mathbf{x}_{k+1|k}$ takes the form

$$\mathbf{x}_{k+1|k} \quad = \quad \mathbf{A}_k \mathbf{x}_{k|k} + \mathbf{B}_k \mathbf{u}_k \tag{6.3.12}$$

From the measurement model of Equation 6.3.10, the noise-free a priori measurement estimate $\mathbf{z}_{k+1|k}$ takes the form

$$\mathbf{z}_{k+1|k} \quad = \quad \mathbf{H}_{k+1} \mathbf{x}_{k+1|k} \tag{6.3.13}$$

The a priori state error covariance $\mathbf{P}_{k+1|k}$

$$\mathbf{P}_{k+1|k} \quad = \quad E\left[\mathbf{e}_{k+1|k} \mathbf{e}_{k+1|k}^T \Big| \mathbf{Z}^k\right] \tag{6.3.14}$$

is obtained from the a priori state estimate $\mathbf{x}_{k+1|k}$

$$\mathbf{P}_{k+1|k} \quad = \quad \mathbf{A}_k \mathbf{P}_{k|k} \mathbf{A}_k^T + \mathbf{Q}_k \tag{6.3.15}$$

where $\mathbf{e}_{k+1|k} = \mathbf{x}_{k+1} - \mathbf{x}_{k+1|k}$ is the a priori state estimation error

$$\mathbf{e}_{k+1|k} \quad = \quad \mathbf{A}_k \mathbf{e}_{k|k} + \mathbf{v}_k \tag{6.3.16}$$

The a posteriori state error covariance $\mathbf{P}_{k+1|k+1}$

$$\mathbf{P}_{k+1|k+1} \quad = \quad E\left[\mathbf{e}_{k+1|k+1} \mathbf{e}_{k+1|k+1}^T \Big| \mathbf{Z}^k\right] \tag{6.3.17}$$

is obtained from the a posteriori state estimate $\mathbf{x}_{k+1|k+1}$

$$\mathbf{P}_{k+1|k+1} \quad = \quad \mathbf{P}_{k+1|k} - \mathbf{P}_{k+1|k} \mathbf{H}_{k+1}^T \mathbf{K}_{k+1}^T - \mathbf{K}_{k+1} \mathbf{H}_{k+1} \mathbf{P}_{k+1|k} + \mathbf{K}_{k+1} \left(\mathbf{H}_{k+1} \mathbf{P}_{k+1|k} \mathbf{H}_{k+1}^T + \mathbf{R}_{k+1}\right) \mathbf{K}_{k+1}^T \tag{6.3.18}$$

where $\mathbf{e}_{k+1|k+1} = \mathbf{x}_{k+1} - \mathbf{x}_{k+1|k+1}$ is the a posteriori state estimation error

$$\mathbf{e}_{k+1|k+1} \quad = \quad \mathbf{e}_{k+1|k} - \mathbf{K}_{k+1} \left(\mathbf{H}_{k+1} \mathbf{e}_{k+1|k} + \mathbf{w}_{k+1}\right) \tag{6.3.19}$$

Making the derivative of the trace of the a posteriori error covariance $\mathbf{P}_{k+1|k+1}$ with respect to the Kalman gain $\mathbf{K}_{k+1}$ equal to $\mathbf{0}$, and solving for $\mathbf{K}_{k+1}$ the optimal gain for the computation of the a posteriori state estimate $\mathbf{x}_{k+1|k+1}$ is obtained

$$\mathbf{K}_{k+1} \quad = \quad \mathbf{P}_{k+1|k}\mathbf{H}_{k+1}^T \left(\mathbf{H}_{k+1}\mathbf{P}_{k+1|k}\mathbf{H}_{k+1}^T + \mathbf{R}_{k+1}\right)^{-1}$$

(6.3.20)

which reduces the a posteriori state error covariance $\mathbf{P}_{k+1|k+1}$ of Equation 6.3.18 to the well known form

$$\mathbf{P}_{k+1|k+1} \quad = \quad \mathbf{P}_{k+1|k} - \mathbf{K}_{k+1}\mathbf{H}_{k+1}\mathbf{P}_{k+1|k}$$

(6.3.21)

The recursion of the a posteriori state error covariance $\mathbf{P}_{k+1|k+1}$ of Equation 6.3.21 is ill-conditioned [111]. As the filter converges the cancelling of significant digits on the a posteriori state error covariance $\mathbf{P}_{k+1|k+1}$ leads to a non Positive Semi Definite (PSD) matrix, which cannot be true from the definition of the a posteriori state error covariance $\mathbf{P}_{k+1|k+1}$ in Equation 6.3.17. The a posteriori error covariance $\mathbf{P}_{k+1|k+1}$ is guaranteed to be PSD by multiplying the Kalman gain $\mathbf{K}_{k+1}$ of Equation 6.3.20 by $\left(\mathbf{H}_{k+1}\mathbf{P}_{k+1|k}\mathbf{H}_{k+1}^T + \mathbf{R}_{k+1}\right)\mathbf{K}_{k+1}^T$ to obtain

$$\mathbf{K}_{k+1}\mathbf{H}_{k+1}\mathbf{P}_{k+1|k}\mathbf{H}_{k+1}^T\mathbf{K}_{k+1}^T - \mathbf{P}_{k+1|k}\mathbf{H}_{k+1}^T\mathbf{K}_{k+1}^T + \mathbf{K}_{k+1}\mathbf{R}_{k+1}\mathbf{K}_{k+1}^T \quad = \quad 0$$

(6.3.22)

and adding Equation 6.3.22 into the a posteriori error covariance $\mathbf{P}_{k+1|k+1}$ of Equation 6.3.21 to obtain the Joseph form of the a posteriori error covariance $\mathbf{P}_{k+1|k+1}$, which given its quadratic nature is PSD

$$\mathbf{P}_{k+1|k+1} \quad = \quad \left(\mathbf{I} - \mathbf{K}_{k+1}\mathbf{H}_{k+1}\right)\mathbf{P}_{k+1|k}\left(\mathbf{I} - \mathbf{K}_{k+1}\mathbf{H}_{k+1}\right)^T + \mathbf{K}_{k+1}\mathbf{R}_{k+1}\mathbf{K}_{k+1}^T$$

(6.3.23)

The Kalman gain $\mathbf{K}_{k+1}$ is proportional to the uncertainty in the a priori state estimate $\mathbf{x}_{k+1|k}$. For an uncertain measurement $\mathbf{z}_{k+1}$ and precise a priori state estimate $\mathbf{x}_{k+1|k}$ the prediction of the a posteriori state estimate $\mathbf{x}_{k+1|k+1}$ relies more on the process model of Equation 6.3.9 than the measurement $\mathbf{z}_{k+1}$ and the a posteriori state error covariance $\mathbf{P}_{k+1|k+1}$ sees little reduction

$$\lim_{\mathbf{P}_{k+1|k}\to\mathbf{0}} \mathbf{K}_{k+1} \quad = \quad \mathbf{0} \quad \Rightarrow \quad \begin{array}{ccc} \mathbf{x}_{k+1|k+1} & = & \mathbf{x}_{k+1|k} \\ \mathbf{P}_{k+1|k+1} & = & \mathbf{P}_{k+1|k} \end{array}$$

(6.3.24)

The Kalman gain $\mathbf{K}_{k+1}$ is inversely proportional to the uncertainty in the measurement $\mathbf{z}_{k+1}$. For a precise the measurement $\mathbf{z}_{k+1}$ and uncertain the a priori state estimate $\mathbf{x}_{k+1|k}$ the prediction of the a posteriori state estimate $\mathbf{x}_{k+1|k+1}$ relies more on the measurement $\mathbf{z}_{k+1}$ than the process model of Equation 6.3.9 and the a posteriori state error covariance $\mathbf{P}_{k+1|k+1}$ is considerably reduced

$$\lim_{\mathbf{R}_{k+1}\to\mathbf{0}} \mathbf{K}_{k+1} \quad = \quad \mathbf{H}_{k+1}^{-1} \quad \Rightarrow \quad \begin{array}{ccc} \mathbf{x}_{k+1|k+1} & = & \mathbf{H}_{k+1}^{-1}\mathbf{z}_{k+1} \\ \mathbf{P}_{k+1|k+1} & = & \mathbf{0} \end{array}$$

(6.3.25)

The Kalman filter works because the combination of the a priori state estimate $\mathbf{x}_{k+1|k}$, conditioned on all prior measurements $\mathbf{Z}^k$, and the a posteriori state estimate $\mathbf{x}_{k|k}$, with the state $\mathbf{x}_k$ distribution

$$p\left(\mathbf{x}_k|\mathbf{z}_k\right) \quad \sim \quad \mathcal{N}\left(\mathbf{x}_{k|k}, \mathbf{P}_{k|k}\right)$$

(6.3.26)

into the a posteriori state estimate $\mathbf{x}_{k+1|k+1}$ is an improved estimate of the state $\mathbf{x}_{k+1}$, based on the probability principle that the combination of two estimates results in an improved estimate, $\frac{1}{\mathbf{P}_{k+1|k+1}^2} = \frac{1}{\mathbf{P}_{k+1|k}^2} + \frac{1}{\mathbf{P}_{k|k}^2}$, as depicted in Figure 6.11.
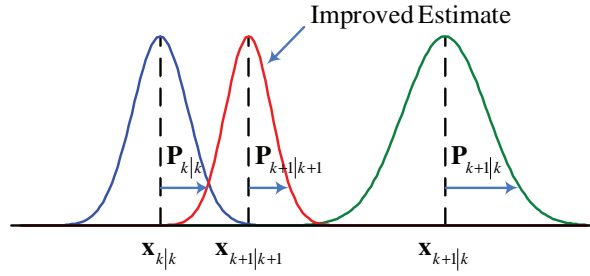
Figure 6.11: Improved Estimate Through Combination of Two Estimates

6.4 Implementation

For the proposed application of airborne surveillance for search and rescue operations, the antenna is fitted under the wings of a small UAV flying over the ocean. The target area is assumed to be a constant distance from the UAV and consist only of sea water at a uniform temperature. The only discrepancy from this continuum is the sea vessels being searched for. Reconstruction of the target area is required to accurately determine the position of an object and to differentiate between objects situated along the plane of the flight path.

For this work the state is the target area seen by the antenna at time step k, the process evolution models the change of the target area from time step k to time step $k+1$ as the antenna pattern is shifted by the flight of the UAV, the measurement is the measured output of the antenna at time step k and the measurement evolution models the antenna pattern. The change from the state $\mathbf{x}_k$ to the state $\mathbf{x}_{k+1}$ is based entirely on the flight of the UAV, with no external control, thereby reducing the process model of Equation 6.3.9 to

$$\mathbf{x}_{k+1} = \mathbf{A}_k\mathbf{x}_k + \mathbf{v}_k \tag{6.4.1}$$

There is a large overlap between the target area scanned by the measurement $\mathbf{z}_k$ and the target area scanned by the measurement $\mathbf{z}_{k+1}$, as depicted in Figure 6.12. The extension to the front of the UAV made to the target area by the measurement $\mathbf{z}_{k+1}$ is predicted and the extension to the back of the UAV no longer seen by the measurement $\mathbf{z}_{k+1}$ is omitted, with the rest of the target area carried over from the state $\mathbf{x}_k$.
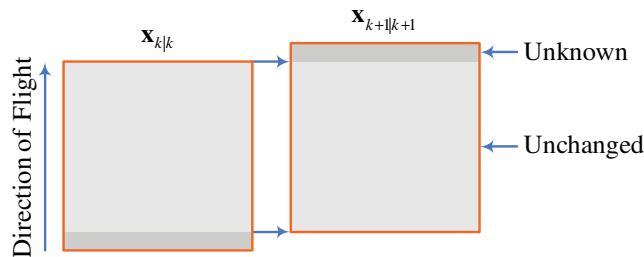
Figure 6.12: Correlation between Two States

As the target area is assumed to be static, with a few slow moving objects on a stable background, there is no significant change between time step k and time step $k+1$ and between pixel row P^n and pixel row P^{n+1}, the pixel rows $P^n|_{n=2,...,N}$ of the a posteriori state estimate $\mathbf{x}_{k|k}$ are shifted unchanged into the pixel rows $P^n|_{n=1,...,N-1}$ of the a priori state estimate $\mathbf{x}_{k+1|k}$ using the state evolution.

As the target area is assumed to be static, with a few slow moving objects on a stable background, the target area as seen by the measurement $\mathbf{z}_k$ is assumed to be equal to the target area as seen by the measurement $\mathbf{z}_{k+1}$.

For the same reason the extension to the front on the UAV seen by the measurement $\mathbf{z}_{k+1}$ is predicted to be equivalent to the target area just before this extension.

Mathematically this is done by shifting pixel rows $P^n|_{n=2,...,N}$ of the a posteriori state estimate $\mathbf{x}_{k|k}$ unchanged into pixel rows $P^n|_{n=1,...,N-1}$ of the a priori state estimate $\mathbf{x}_{k+1|k}$ and predicting pixel row P^N of the state $\mathbf{x}_{k+1}$ as equal to pixel row P^N of the state $\mathbf{x}_k$ using state evolution

$$\mathbf{A}_k = \begin{bmatrix} \mathbf{A}'_k & \mathbf{0} & \mathbf{0} & \mathbf{0} \\ \mathbf{0} & \mathbf{A}'_k & \mathbf{0} & \mathbf{0} \\ \mathbf{0} & \mathbf{0} & \ddots & \mathbf{0} \\ \mathbf{0} & \mathbf{0} & \mathbf{0} & \mathbf{A}'_k \end{bmatrix} \quad \text{where} \quad \mathbf{A}'_k = \begin{bmatrix} 0 & 1 & 0 & 0 \\ 0 & 0 & \ddots & 0 \\ 0 & 0 & 0 & 1 \\ 0 & 0 & 0 & 1 \end{bmatrix} \tag{6.4.2}$$

The a posteriori state estimate is initialised as $\mathbf{x}_{k|k}|_{k=0} = \mathbf{0}$, a $\mathbf{A}'_k$ is required for each pixel column P^m and the pixel columns P^m of the state are lexicographically ordered into one column for multiplication with the state evolution.

The antenna concurrently scans the target area along the plane perpendicular to the flight path, with each orientation scanned by a beam at a different frequency f_0^m. The frequency range f_L to f_H is divided into $M = 9$ contiguous bands, each assigned to a different pixel column P^m. Even though the main beam at frequency f_0^m is orientated to a particular part of the target, the whole target area is measured at frequency f_0^m.

Therefore, the antenna patterns at the different frequencies f_0^m are combined to reconstruct the target area. Mathematically this is done by combining the $M = 9$ measured 2D antenna patterns Ant_{2D} into one measurement evolution $\mathbf{H}_k$. Each row of measurement evolution relates one frequency component of the measurement to the state, as depicted in Figure 6.13.
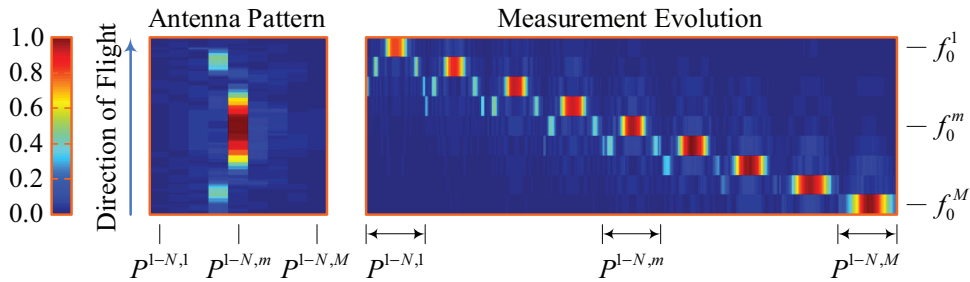
Figure 6.13: Measurement Model

As the antenna has a narrow beam along the plane perpendicular to the flight path, only pixel column P^m is significant affected by Ant_{2D}^m. As the antenna has a very broad beam along the plane of the flight path, many pixels within pixel column P^m are significant affected by Ant_{2D}^m. This blurs the image, making it difficult to accurately determine the position of an object or to differentiate between objects situated along the flight path.

The three covariance matrices are initialised as

$$\begin{aligned} \mathbf{P}_{k|k}|_{k=0} &= \mathbf{A}_k \varepsilon_1 \mathbf{A}_k^T \\ \mathbf{Q}_k|_{k=0} &= \mathbf{A}_k \varepsilon_2 \mathbf{A}_k^T \\ \mathbf{R}_k|_{k=0} &= \mathbf{H}_k \varepsilon_3 \mathbf{H}_k^T \end{aligned} \tag{6.4.3}$$

where ε_1, ε_2 and ε_3 reflect the degree of uncertainty with regards to the state $\mathbf{x}_k$, the measurement $\mathbf{z}_k$ and the process model of Equation 6.4.1.

Given the initial conditions, the Kalman filter is obtained iteratively by predicting the a priori estimates of the state, the measurement and the state error covariance

$$
\begin{aligned}
\mathbf{x}_{k+1|k} &= \mathbf{A}_k \mathbf{x}_{k|k} + \mathbf{B}_k \mathbf{u}_k \\
\mathbf{z}_{k+1|k} &= \mathbf{H}_k \mathbf{x}_{k+1|k} \\
\mathbf{P}_{k+1|k} &= \mathbf{A}_k \mathbf{P}_{k|k} \mathbf{A}_k^T + \mathbf{Q}_k
\end{aligned}
\tag{6.4.4}
$$

and computing the Kalman gain to update the a posteriori estimates of the state and the state error covariance

$$
\begin{aligned}
\mathbf{K}_{k+1} &= \mathbf{P}_{k+1|k} \mathbf{H}_{k+1}^T \left(\mathbf{H}_{k+1} \mathbf{P}_{k+1|k} \mathbf{H}_{k+1}^T + \mathbf{R}_{k+1} \right)^{-1} \\
\mathbf{x}_{k+1|k+1} &= \mathbf{x}_{k+1|k} + \mathbf{K}_{k+1} \left(\mathbf{z}_{k+1} - \mathbf{z}_{k+1|k} \right) \\
\mathbf{P}_{k+1|k+1} &= \left(\mathbf{I} - \mathbf{K}_{k+1} \mathbf{H}_{k+1} \right) \mathbf{P}_{k+1|k} \left(\mathbf{I} - \mathbf{K}_{k+1} \mathbf{H}_{k+1} \right)^T + \mathbf{K}_{k+1} \mathbf{R}_{k+1} \mathbf{K}_{k+1}^T
\end{aligned}
\tag{6.4.5}
$$

6.5 Simulations

Specific target areas are simulated to test the ability of the Kalman filter to model the flight process and to remove the blur of the measurement process. The input parameters are gradually increased from idealised values to the expected values in order to simplify the optimisation process.

As a first experiment, the ability of the Kalman filter to model the flight process is tested for a target area containing a single frequency component and with a measurement evolution of size 9×27 based on antenna measurements using a reflector focusing the pattern into a $1° \times 1°$ main beam, as depicted in Figure 6.14.
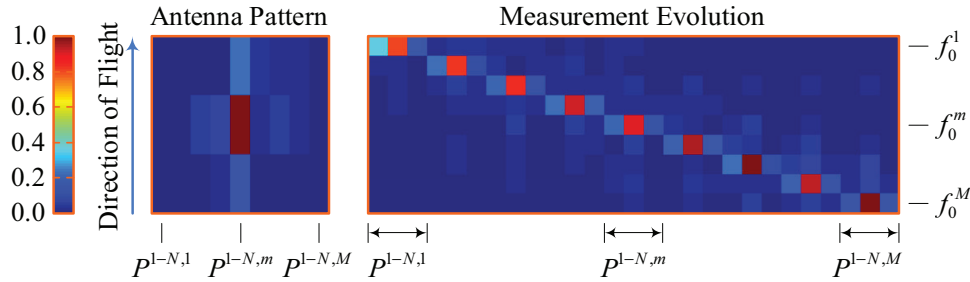
Figure 6.14: Idealised Measurement Model using Position Model

The idealisation of the antenna pattern removes the blurring effect of the antenna pattern into neighbouring frequency components and removes the blurring effect of the antenna pattern into neighbouring time intervals to simplify the problem to just one involving the modelling of the flight process.

The response of the Kalman filter to a change between pixel row P^n and pixel row P^{n+1} is improved by adding a velocity parameter Δx_k to the state $\mathbf{x}_k$. In this position-velocity model pixel row P^N of state $\mathbf{x}_{k+1}$ is predicted as the sum of pixel row P^N of state $\mathbf{x}_k$ and the change between pixel row P^{N-1} and pixel row P^N of state $\mathbf{x}_k$, with the change between pixel row P^{N-1} and pixel row P^N of state $\mathbf{x}_{k+1}$ equated with the change between pixel row P^{N-1} and pixel row P^N of state $\mathbf{x}_k$

$$
\mathbf{A}_k =
\begin{bmatrix}
\mathbf{A}_k' & \mathbf{0} & \mathbf{0} & \mathbf{0} \\
\mathbf{0} & \mathbf{A}_k' & \mathbf{0} & \mathbf{0} \\
\mathbf{0} & \mathbf{0} & \ddots & \mathbf{0} \\
\mathbf{0} & \mathbf{0} & \mathbf{0} & \mathbf{A}_k'
\end{bmatrix}
\quad \text{where} \quad
\mathbf{A}_k' =
\begin{bmatrix}
0 & 1 & 0 & 0 & 0 \\
0 & 0 & \ddots & 0 & 0 \\
0 & 0 & 0 & 1 & 0 \\
0 & 0 & 0 & 1 & 1 \\
0 & 0 & 0 & 0 & 1
\end{bmatrix}
\tag{6.5.1}
$$

It can be seen that for the standard implementation the response to the change between pixel row P^n and pixel row P^{n+1} is not quick enough, resulting in a delayed response in the a posteriori state estimate $\mathbf{x}_{k|k}$ to the state $\mathbf{x}_k$, as depicted in Figure 6.15. Also evident is the improved response of the position-velocity model, which has a reduced smear of the object and correctly predicts the central position of the object.
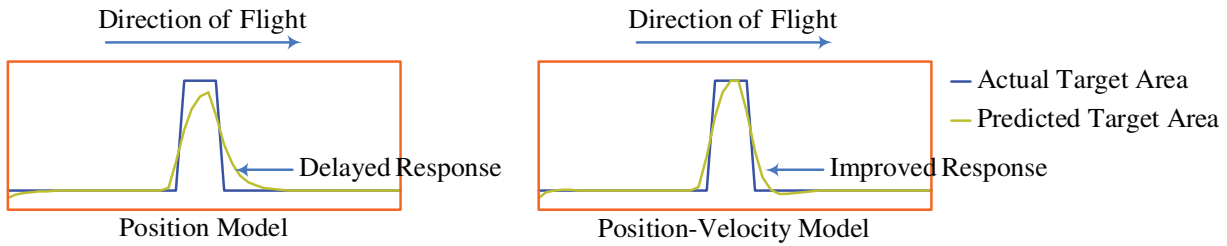
Figure 6.15: Idealised Single Frequency Target Area

With no correlation between the velocity parameter of the state and the measurement, zero-value columns are inserted after each pixel column P^m into the measurement evolution, as depicted in Figure 6.16.
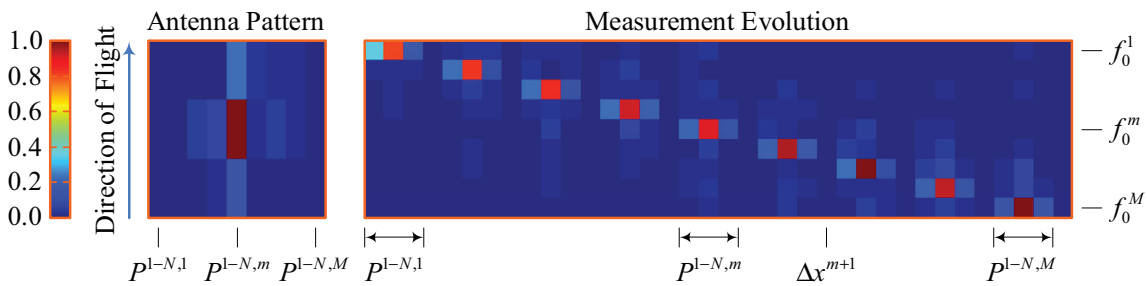
Figure 6.16: Idealised Measurement Model using Position-Velocity Model

A second experiment is performed to test the ability of the Kalman filter to model the flight process for the same target area, but this time with a measurement evolution of size 9×108 based on antenna measurements using a reflector that focuses the antenna pattern into a $1° \times 10°$ main beam, as depicted in Figure 6.17. This focusing reduces the sidelobes to such a level that blurring is almost solely reserved to within each bandwidth.
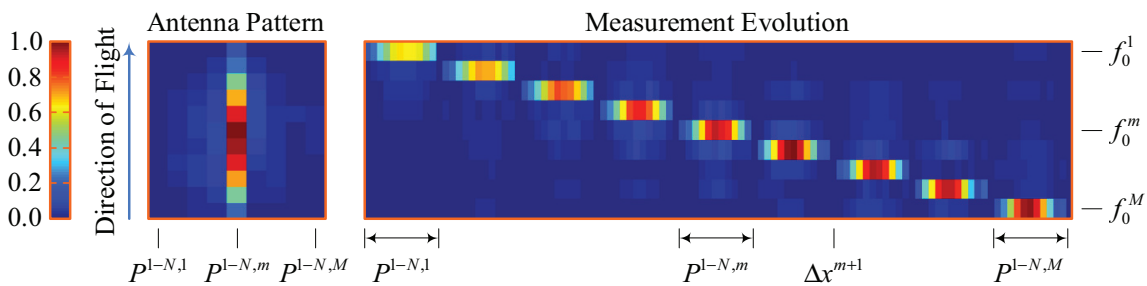
Figure 6.17: Partially Idealised Measurement Model using Position-Velocity Model

The idealisation of the measurement model is lessened to incorporate modelling of the blurring effect of the antenna pattern. The increased width of the main beam maps onto a larger surface than the $1° \times 1°$ main beam, requiring a larger measurement evolution to model the relationship between the state and the measurement.

The response to the change between pixel row P^n and pixel row P^{n+1} of the state is spread over a number of pixels proportional to the width of the main beam, resulting in a blurred response in the posteriori state estimate to the state, as depicted in Figure 6.18. An improved response is obtained by increasing the number of time steps calculated per Kalman filter loop.
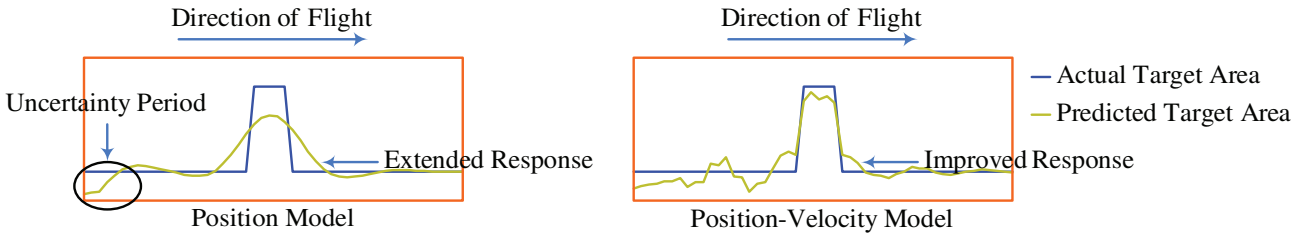
Figure 6.18: Partially Idealised Single Frequency Target Area

For this multi-measurement model the state is extended by c pixel rows, where c is the number of extra time steps calculated per Kalman filter loop, which extends the size of each $\mathbf{A}'_k$ by c in the state evolution.

Also, each row within the measurement evolution is repeated c times, but with one pixel offsets due to the shift in focus from time step k to time step $k+1$ produced by the flight of the UAV. The measurement evolution is increased from size 9×108 for $c = 0$ to size 9×198 for $c = 10$, as depicted in Figure 6.19.
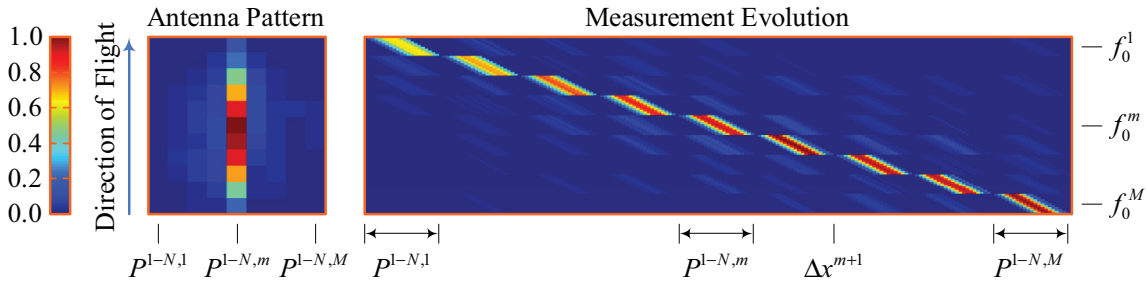
Figure 6.19: Partially Idealised Measurement Model using Multi-Measurement Model

The size of the measurement evolution has a direct effect on the number of time steps the Kalman filter takes to adapt to the model. The larger the area the main beam of the antenna pattern maps onto, the more pixels that need to be predicted concurrently in the initialisation of the posteriori state estimate and the longer the uncertainty period of the a posteriori state estimate. The uncertainty period for the $1° \times 10°$ main beam is longer than for the $1° \times 1°$ main beam, as depicted in Figure 6.18.

The reason for the improved response of the multi-measurement model is accredited to the increased size of measurement evolution. For a single time step per Kalman filter loop and a single frequency component target area, the denominator of the Kalman gain of Equation 6.3.20 is a 1×1 matrix that can only globally rectify the Kalman gain of size 12×1, and thereby only globally rectify the pixels of the state.

When the number of time steps is increased per Kalman filter loop to 11 with $c = 10$, the denominator of the Kalman gain of Equation 6.3.20 increases in size to 11×11. In approaching the size of the Kalman gain of 22×11, the elements of the Kalman gain are rectified locally and thereby the pixels of the state are rectified individually. When a large number of time steps are used per Kalman filter loop, $\mathbf{K}_k \to \mathbf{H}_{k+1}^{-1}$ when $\mathbf{R}_{k+1} \to \mathbf{0}$.

The final set of experiments test the ability of the Kalman filter to remove the errors in the measurement process using the measurement evolution of Figure 6.19 and a full frequency range target area of size 9×50 containing a single central high intensity object of size 3×3 surrounded by a low intensity background, as depicted in Figure 6.20.
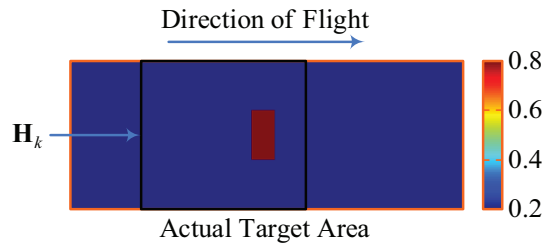
Figure 6.20: Partially Idealised Full Range Target Area with Single Object

The last idealisation is removed to incorporate modelling of the blurring effect into neighbouring frequency components and to incorporate modelling of the unequal gain between frequency components. The large size of the measurement evolution results in a long uncertainty period.

The variance in absolute gain between the components of the antenna pattern returns a false multi-level object and background, while the partial blurring of the object to neighbouring bands is accredited to non-ideal slope of the main beam. The Kalman filter is able to reduce both of these inaccuracies once the long uncertainty period has past, as depicted in Figure 6.21.
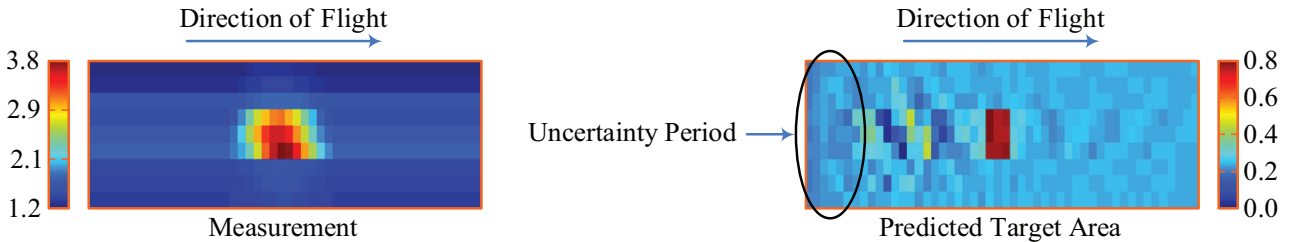
Figure 6.21: Predicted Target Area for Partially Idealised Full Range Target Area with Single Object

The ability of the Kalman filter to differentiate between objects situated along the plane of the flight path is tested using the same measurement evolution of Figure 6.19, but this time with a full frequency range target area of size 9×50 containing a single central high intensity object of size 3×3 bordered by two moderately high intensity objects of size 7×7 and surrounded by a low intensity background, as depicted in Figure 6.22.
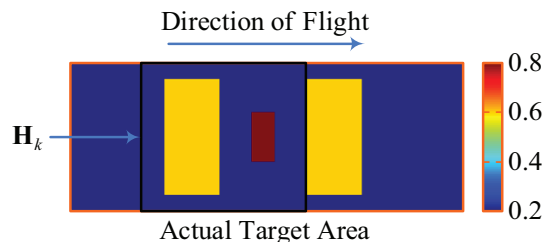
Figure 6.22: Partially Idealised Full Range Target Area with Multiple Objects

The ability of the Kalman filter is not affected by the number of objects within the target area. The blurring effect of the antenna pattern merges the closely spaced objects into a single object, with a false higher intensity at the location of the two border objects. The Kalman filter is able to respond quickly enough to a change between pixel row P^n and pixel row P^{n+1} of the state, resulting in the objects being sharpened and detached from each other, as depicted in Figure 6.23.
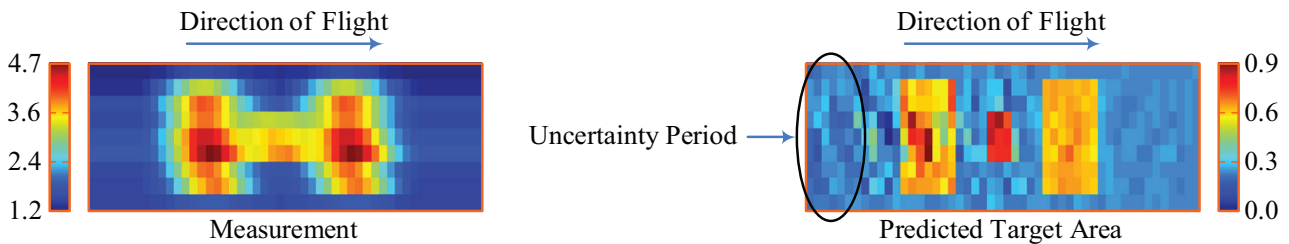
Figure 6.23: Predicted Target Area for Partially Idealised Full Range Target Area with Multiple Objects

The Kalman filter is able to correct for unequal gain between frequency components, reduces blur into other frequency components and into other time intervals and to separate closely spaced objects.

The ability of the Kalman filter to operate on noisy measurements is tested using the same measurement evolution of Figure 6.19, but this time with noise injected into the target area with multiple objects, as depicted in Figure 6.24. The variance of the noise is equal in magnitude to the variance between the central high intensity object and the two moderately high intensity objects.
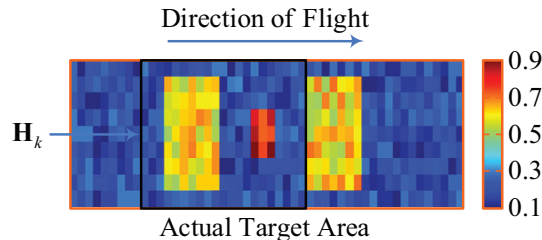
Figure 6.24: Partially Idealised Full Range Noisy Target Area with Multiple Objects

The ability of the Kalman filter is not affected by the noise within the target area, with the closely spaced objects only again detached from each other, as depicted in Figure 6.25. However, the reconstructed image is still noisy, but this is to be expected as the image reconstruction has been developed to model the blurring effect of the antenna pattern and not conventional noise.
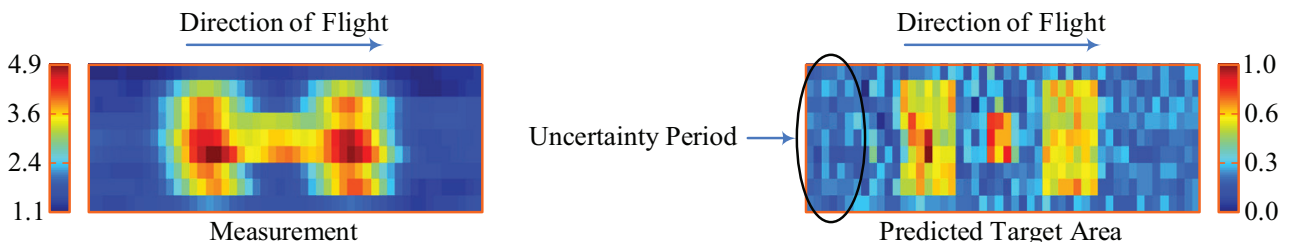
Figure 6.25: Predicted Target Area for Partially Idealised Full Range Noisy Target Area with Multiple Objects

In order to clarify the corrective power of this algorithm, the results are compared with that of a straight deconvolution algorithm, where for each measurement $\mathbf{z}_k$ the predicted target area $\mathbf{x}_k$ is calculated as

$$\mathbf{x}_k \quad = \quad \mathbf{H}_k^T \mathbf{z}_k \tag{6.5.2}$$

where $\mathbf{H}_k^T$ is the pseudo-inverse of the measurement evolution. The inverse is not calculated as the measurement evolution is not square. Instead the pseudo-inverse is obtained, with the potential for singularity issues.

The ability of the straight deconvolution algorithm to operate on noisy measurements is tested using a measurement evolution of size 9×99 based on antenna measurements using a reflector that focuses the antenna pattern into a $1° \times 10°$ main beam, as depicted in Figure 6.26. This measurement evolution is equivalent to the measurement evolution of Figure 6.17, just without the velocity parameter.
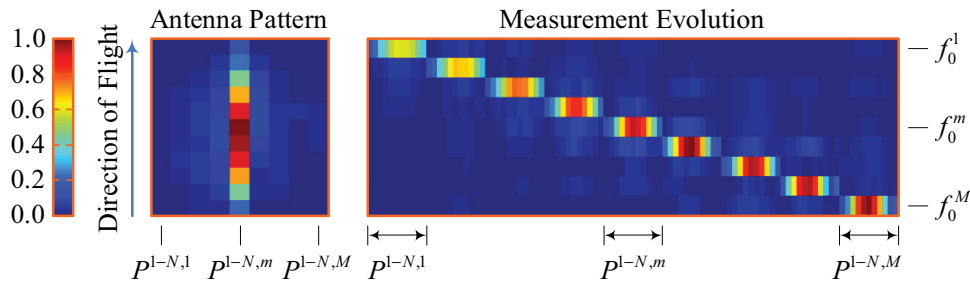
Figure 6.26: Partially Idealised Measurement Model using Position Model

The ability of the straight deconvolution algorithm to operate on noisy measurements is tested on the noise injected target area with multiple objects of Figure 6.24, with the predicted target area depicted in Figure 6.27. The predicted target area contains two uncertainty periods, at the beginning and the end of the measurements, with the three objects still blurred together.
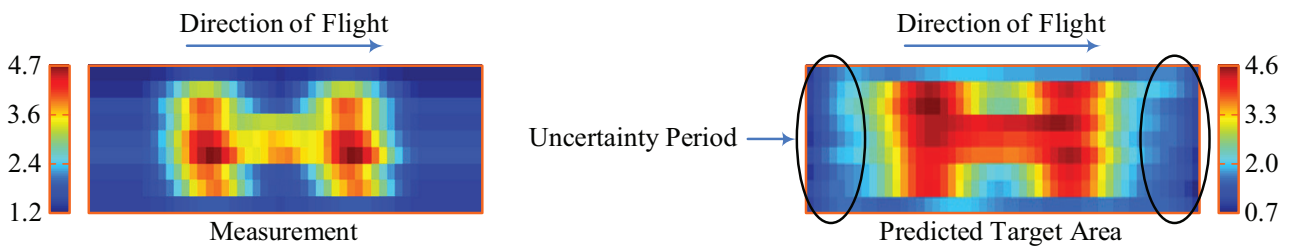
Figure 6.27: Predicted Target Area using Straight Deconvolution Algorithm

In the straight deconvolution algorithm only working on a single measurement at a time, it is very difficult to determine the position of an object due to the blurring effect on the antenna pattern. Only when a whole range of measurements are used is it possible to locate the central point of an object. In the straight deconvolution algorithm not taking into account the relationship between consequent measurements, any information gained in stage k regarding the target area is not passed onto stage $k+1$ to improve the prediction of the target area.

Due to the large overlap of target area between subsequent measurements and the blurring effect of the antenna pattern, the reconstruction algorithm needs to take into account multiple measurements and multiple predictions to correctly predict the target area. This is done by the Kalman filter, and is the reason for its supremacy with regards to a straight deconvolution algorithm.

6.6   Conclusion

In this chapter the post processor algorithm is described. The broad beam of the antenna pattern along the plane of the flight path causes three interrelated problems for the post processor, requiring a novel technique that does not fall within the conventional image reconstruction algorithms of the literature.

Firstly, the image formation process needs to be modelled. In using the the flight path of the UAV to move the measurement plane of the imaging system along, the sequential order of measurements needs to be maintained, as well as the overlapping layers of the reconstructed images.

Secondly, the image blurring process needs to be modelled. As can be seen in the 3D antenna patterns depicted in Chapter 3, the blur is different for different antenna configurations as well as for different frequency bands within the same antenna configuration. This causes the variance between channels in response to a common input, as described in Section 6.5.

Thirdly, the many-to-one relationship between the measurement and the detected area needs to be modelled. The broad beam of the antenna pattern results in a large area being detected during the measurement made for each pixel, resulting in the chance of singularities forming within the matrices of the algorithm.

Conventional image reconstruction processes have not been designed to work with such problems. They have been developed to reconstruct stationary, independent images that have been blurred by the unfocused lens of the camera modelled by Gaussian functions and for a near linear relationship between the measurement and the target area, with only a limited extension to the borders of the images to account for blurring at the borders.

Therefore, this dissertation proposes a novel technique. This technique is based on the Kalman filter, which has been developed for dynamic systems with the relationship between the image and target area defined by the user, which for this application is the actual measured antenna pattern. In using the overlapping antenna patterns, the many-to-one relationship is reduced by concurrently reconstructing all the pixels of one measurements and is further redueces by concurrently reconstructing the pixels of many measurements.

It has been shown for a simulated target area that the image reconstruction algorithm is capable of reconstructing the target area. The next step is to test the algorithm on actual measurements of the imaging system. As the full measurement of an airborne system is a major project on its own, with the variations in flight path, yaw and pitch to be factored into the algorithm, this is to form the focus of future projects.

Chapter 7

Conclusion

Man is technologically driven to improve his quality of life by artificially controlling the natural world around him. Man is the only species to design shelters from the natural elements, to design vehicles to to transport goods and personnel at unnatural speeds, and to design communication systems to speak to people on other continents from the comfort of one's own home.

Man's drive to increase his vision capabilities beyond the optical emissions that is naturally detected by his eyes is another such endeavour, with examples of radar, lidar, sonar and thermal imaging in the Infra-Red (IR) region. Thermal imaging in the Millimetre-Wave (MMW) region, defined as 30GHz to 300GHz, is another example, and is the focus of this dissertation.

While MMW imaging does not seem the obvious choice when calculating the expected radiation levels of MMW emissions, as the MMW emissions of room temperature objects are between 10^{10} and 10^7 times smaller than IR emissions within the thermal imaging region of 20THz to 300THz. However, when taking into account such phenomena as the effect of atmospheric constituents on emissions, this does become an attractive option.

Unlike optical and IR emissions, which are severely scattered and absorbed by inclement weather, within certain transmissions windows of the MMW region the difference in MMW emissions from different objects remain constant over a large range of weather conditions, such as cloud cover, fog, sand storms and marine layers, with heavy rain one of the few limiting conditions.

The focus of this work is to make use of the emission, reflection and transmission properties of objects within the MMW region to form images for applications such as airborne surveillance in search and rescue operations. The imaging system would be attached to the wing of a small Unmanned Aerial Vehicle (UAV), detecting the MMW emissions through the inclement weather.

Such a system would be able to locate boats and trace their point of origin because of the contrast of metal, fibreglass, wood, rubber and long, trailing wakes to a water background. Such systems have been used in applications such as search and rescue operations, for surveillance and reconnaissance and in the detection and capture of drug traffickers.

The size, maximum payload and limited power available on a UAV place severe restrictions on the possible implementations of the imaging system, especially the inability to make use of any form of mechanical or optical antenna techniques to couple the MMW emissions to the rest of the system. This is because the imaging system must conform to the shape of the wing of the UAV to minimise the effect on the aerodynamics of the UAV, with mechanical and optical techniques requiring motors and optics that are too bulky for this application.

The proposed solution is a long, thin waveguide antenna that is chosen for its inherent space-to-frequency mapping, where the orientation of the main beam of the antenna sweeps across the target area as a function of frequency. Such an antenna has a narrow, high gain, frequency-scanned beam along the plane perpendicular to the flight path, but a very broad beam along the plane of the flight path.

Techniques exists to focus the antenna pattern along the plane of the flight path as well, but as has already been stressed, these mechanical and optical techniques require components that are too massive for attachment to the underside of a small UAV. The only solution is to make use of a post processor to reconstruct an image of the target area from the blurred measurement.

Conventional image techniques are designed to work with localised blurring of a Gaussian nature, and are unable to deal with the more global blur of the antenna pattern along the plane of the flight path. Therefore, a novel technique was implemented that makes use of the measured antenna pattern to model the blur and reconstruct an image of the target area.

The full measurement of an airborne system is a major project on its own, as variations in flight path, yaw and pitch have to be factored into any image data in such a measurement. This is to form the focus of future projects. For the purposes of this work, it was shown that the system can reconstruct simulated targets using the actual measured antenna pattern successfully.

7.1   Recommendations for Future Work

Due to the scope of the project, the focus of this dissertation was the design of the system, a contiguous wideband stripline multiplexer and the post processor. However, a large number of components were built or bought, configured and connected to each other to obtain a working system that would form the basis for future models, with individual projects assigned to investigate a different subsystem.

The antenna, while not designed as part of this work, is a key role in the imaging system, with the characteristics of the antenna pattern the basis of the image reconstruction algorithm. The focus of the main beam and the instantaneous Field of View (FOV) of the main beam are the two key characteristics of the antenna on the imaging system.

Any improvement to the focus of the main beam by increasing the size of the antenna is instantly passed on to the rest of the system, with no need to redesign any components. However, measurements of the improved antenna pattern would be needed by the post processor to correctly reconstruct an image from the target area for this antenna. This does not place a unnecessary burden on the designer, as these measurements should be done to verify the antenna design.

The same cannot be said for an improvement in instantaneous FOV. There is a theoretical limit to the FOV obtainable by the antenna that can only be extended by increasing the frequency range of the system. This would lead to a redesign to a large portion of the rest of the system, as most of the components are frequency-dependent. In particular, a complete redesign on the multiplexer would be needed.

The multiplexer design was an arduous task, working with strict design specification, a large set of conflicting parameters to optimise, near the limits of the available manufacturing processes and with a medium known to be lossy at the design frequency. However, the multiplexer does successfully perform the task set before it, with the only shortcoming the high loss, which is to be expected at microwave frequencies.

The multiplexer can be improved in three ways.

The first improvement would be the use of a lower loss medium. The obvious realisation at microwave frequencies is waveguide, but this is not a viable option due to the wide bandwidth at the Intermediate Frequency (IF) range, resulting in a lossy stripline solution. Another obvious realisation is suspended stripline which would reduce the loss of the circuit, but would dramatically increase the complexity of the manufacturing process.

Therefore, an indepth study into the possible methods of decreasing the loss of the multiplexer is required. Any improvement would benefit the rest of the system, with only the amplification in the IF range requiring reevaluation to ensure that the dynamic range of the input to the detectors remains optimal.

The second improvement would be the increase in channels. The resolution of the system is equivalent to the number of output channels of the multiplexer. Any increase in channels will improve the resolution and ease the operator's task of identifying objects in the image. However, this would seriously increase the cost of the system, in requiring a larger number of detectors and more computational power to deal with all the channels.

The third improvement would be the adjustment of the frequency range. The bandwidth of the multiplexer was chosen to meet the operational frequencies of affordable, commercially available detectors. If the system were to use devices capable of detection at MMW frequencies, the multiplexer could be realised in waveguide. This would greatly decrease the loss of the multiplexer and would ease the design and manufacturing processes. However, detection at MMW frequencies is expensive.

As has already been discussed, the work of this dissertation was focused on designing a working system that would fuel interest in the field and be the basis for future models. Therefore, as each one of the analogue components were bought and not designed specifically for this application, a large number of progress to the system can be made in these subsystems, with two key examples listed below.

Firstly, while the down-converter would work well with a large input signal, the spectrum of the IF output contains spurious signals that pose problems to the imaging system. Therefore, a redesign of the down-converter would improve the system, with no need to redesign any other subsystem once this improvement has been made.

Secondly, while the dynamic range of affordable, commercially available detectors is very wide at the specified frequencies of the detectors, the dynamic range is very narrow at the upper frequencies of the IF range of the imaging system. A redesign of the detectors would improve the resolution sensitivity of the imaging system and would reduce the amplification required by the system.

7.2   Concluding Remarks

The work in this dissertation covers a wide range of operations performed by a large number of components operating at different frequencies and utilising different media. The frontend of the system is a waveguide antenna operating at MMW frequencies, followed by analogue down-conversion to an IF range for connection to a stripline multiplexer and microstrip detector. The backend of the system works with Direct Current (DC) voltages and digital signals on a post processor.

Each one of these sections required an indepth literature study, and resulted in the design of two novel components, namely the design of a contiguous wideband multipexer realised in stripline and the design of a post processor that makes use of a Kalman filter to reconstruct an image of the target area based on the measured antenna pattern. The end result is a working system that demonstrates the principle that a passive imaging system compact enough to be fitted to the underside of a wing of a small UAV can be used in applications such as airborne surveillance in search and rescue operations to detect maritime vessels in inclement weather.

Appendix A

Construction

A.1 Construction of Antenna

Slot position is given relative to the load end of the waveguide and is taken at the centre of the slot at the centre of the narrow waveguide wall. Slot angles are relative to the normal to the broad wall of the waveguide (as seen from the slot side). Positive angles are clockwise from the normal. Depth is relative to the thinned surface.

Table A.1: Specifications for Machining Narrow Wall Slots

Number	Position [mm]	Angle	Depth [mm]	Number	Position [mm]	Angle	Depth [mm]
110	101.00	+18°40'	0.83	55	361.15	-10°00'	0.99
109	105.73	-18°05'	0.84	54	365.88	+10°05'	0.99
108	110.46	+16°45'	0.87	53	370.61	-9°60'	0.99
107	115.19	-15°25'	0.90	52	375.34	+9°45'	0.99
106	119.92	+14°35'	0.91	51	380.07	-9°30'	0.99
105	124.65	-14°20'	0.92	50	384.80	+9°20'	0.99
104	129.38	+14°00'	0.92	49	389.53	-9°20'	0.99
103	134.11	-13°20'	0.94	48	394.26	+9°20'	0.99
102	138.84	+12°25'	0.95	47	398.99	-9°10'	0.99
101	143.57	-11°40'	0.96	46	403.72	+8°55'	1.00
100	148.30	+11°20'	0.97	45	408.45	-8°40'	1.00
99	153.03	-11°20'	0.97	44	413.18	+8°35'	1.00
98	157.76	+11°20'	0.97	43	417.91	-8°30'	1.00
97	162.49	-11°00'	0.97	42	422.64	+8°25'	1.00
96	167.22	+10°35'	0.98	41	427.37	-8°15'	1.00
95	171.95	-10°30'	0.98	40	432.10	+7°55'	1.00
94	176.68	+10°45'	0.98	39	436.83	-7°45'	1.00
93	181.41	-11°10'	0.97	38	441.56	+7°40'	1.00
92	186.14	+11°25'	0.97	37	446.29	-7°35'	1.00
						Continued on next page	

Table A.1: Specifications for machining narrow-wall slots (continued)

| Number	Position [mm]	Angle	Depth [mm]	Number	Position [mm]	Angle	Depth [mm]
91	190.87	-11°20'	0.97	36	451.02	+7°30'	1.01
90	195.60	+11°15'	0.97	35	455.75	-7°15'	1.01
89	200.33	-11°25'	0.97	34	460.48	+7°00'	1.01
88	205.06	+11°55'	0.96	33	465.21	-6°55'	1.01
87	209.79	-12°15'	0.95	32	469.94	+6°50'	1.01
86	214.52	+12°15'	0.95	31	474.67	-6°45'	1.01
85	219.25	-12°05'	0.96	30	479.40	+6°35'	1.01
84	223.98	+11°60'	0.96	29	484.13	-6°20'	1.01
83	228.71	-12°10'	0.96	28	488.86	+6°05'	1.01
82	233.44	+12°25'	0.95	27	493.59	-5°55'	1.01
81	238.17	-12°30'	0.95	26	498.32	+5°50'	1.02
80	242.90	+12°20'	0.95	25	503.05	-5°40'	1.02
79	247.63	-11°60'	0.96	24	507.78	+5°25'	1.02
78	252.36	+11°55'	0.96	23	512.51	-5°10'	1.02
77	257.09	-12°05'	0.96	22	517.24	+4°60'	1.03
76	261.82	+12°15'	0.95	21	521.97	-4°50'	1.03
75	266.55	-12°10'	0.96	20	526.70	+4°45'	1.03
74	271.28	+11°55'	0.96	19	531.43	-4°35'	1.04
73	276.01	-11°40'	0.96	18	536.16	+4°25'	1.04
72	280.74	+11°40'	0.96	17	540.89	-4°15'	1.05
71	285.47	-11°50'	0.96	16	545.62	+4°05'	1.05
70	290.20	+11°55'	0.96	15	550.35	-4°05'	1.05
69	294.93	-11°45'	0.96	14	555.08	+4°05'	1.05
68	299.66	+11°30'	0.97	13	559.81	-4°00'	1.05
67	304.39	-11°20'	0.97	12	564.54	+4°00'	1.05
66	309.12	+11°20'	0.97	11	569.27	-4°00'	1.05
65	313.85	-11°30'	0.97	10	574.00	+4°10'	1.05
64	318.58	+11°25'	0.97	9	578.73	-4°20'	1.04
63	323.31	-11°05'	0.97	8	583.46	+4°25'	1.04
62	328.04	+10°50'	0.98	7	588.19	-4°30'	1.04
61	332.77	-10°45'	0.98	6	592.92	+4°35'	1.04
60	337.50	+10°45'	0.98	5	597.65	-4°40'	1.03
59	342.23	-10°45'	0.98	4	602.38	+4°45'	1.03
58	346.96	+10°35'	0.98	3	607.11	-4°50'	1.03
57	351.69	-10°15'	0.98	2	611.84	+4°55'	1.03
56	356.42	+10°05'	0.98	1	616.57	-4°50'	1.03

A.2 Construction of Reflector
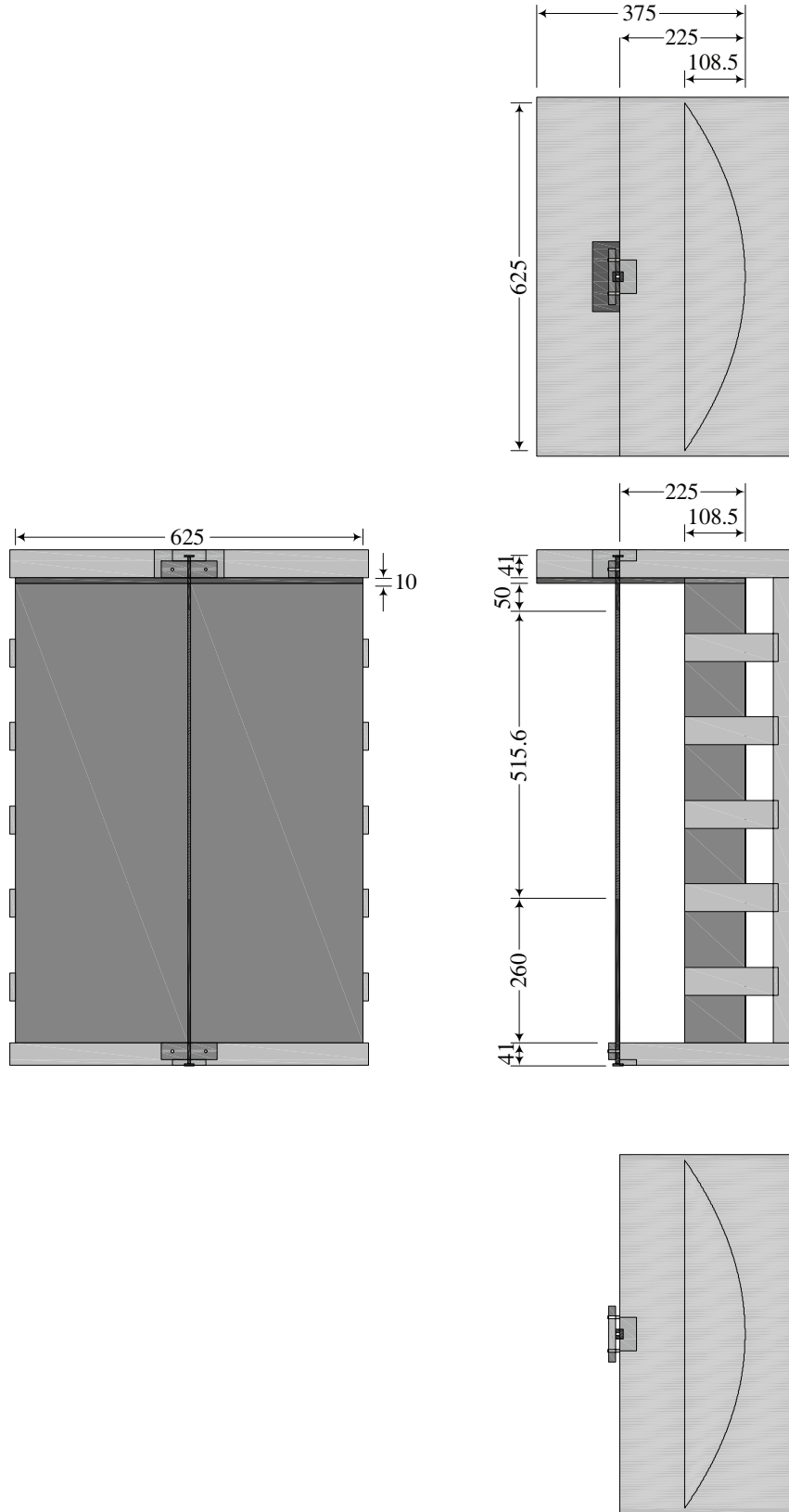
Figure A.1: Technical Drawings of Reflector

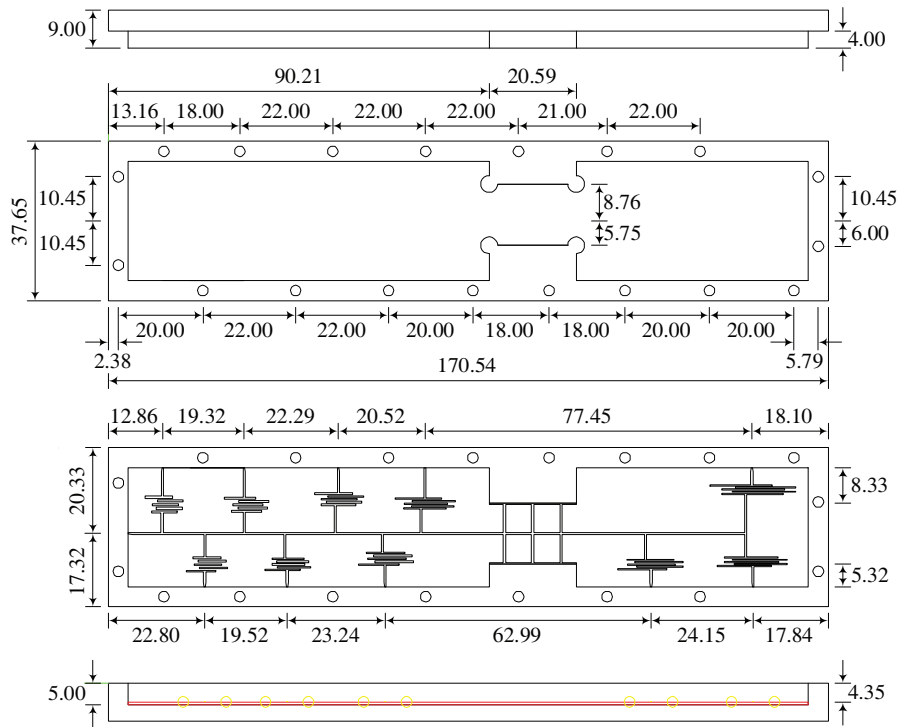## A.3 Construction of Multiplexer

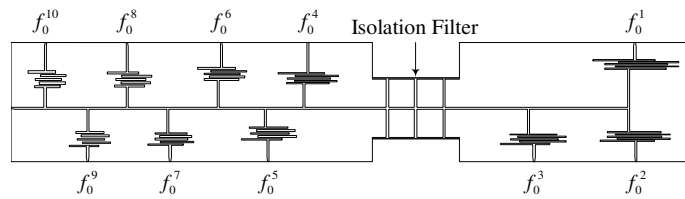**Figure A.2:** Technical Drawings of Multiplexer

Figure A.3: Technical Drawings of Filter Placement on Multiplexer

A.4 Construction of Waveguide Filter
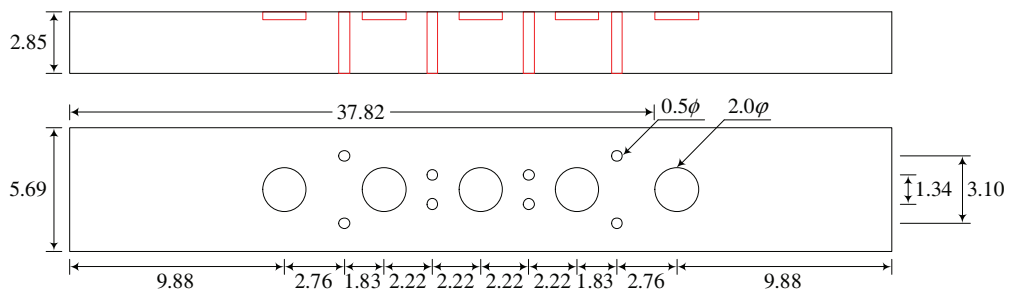
Figure A.4: Coupled-Post Filter Outline

Appendix B

Numerical Methods

For a function $z(x,y)$ discretised at points h-space apart so that

$$z(x,y) \approx z_{i,j} = z(x_i, y_j) \tag{B.0.1}$$

the first-order partial derivatives are

$$
\begin{aligned}
\frac{\partial z}{\partial t} &\approx \frac{z_{i,j}^{n+1} - z_{i,j}^n}{\Delta t} \\
\frac{\partial z}{\partial x} &\approx z_{i,j}^x &= \frac{z_{i+1,j} - z_{i-1,j}}{2h} \\
\frac{\partial z}{\partial x}^+ &\approx z_{i,j}^{x+} &= z_{i+1,j} - z_{i,j} \\
\frac{\partial z}{\partial x}^- &\approx z_{i,j}^{x-} &= z_{i,j} - z_{i-1,j} \\
\frac{\partial z}{\partial y} &\approx z_{i,j}^y &= \frac{z_{i,j+1} - z_{i,j-1}}{2h} \\
\frac{\partial z}{\partial y}^+ &\approx z_{i,j}^{y+} &= z_{i,j+1} - z_{i,j} \\
\frac{\partial z}{\partial y}^- &\approx z_{i,j}^{y-} &= z_{i,j} - z_{i,j-1}
\end{aligned}
\tag{B.0.2}
$$

and the second-order partial derivatives are

$$
\begin{aligned}
\frac{\partial^2 z}{\partial x^2} &\approx z_{i,j}^{xx} &= \frac{z_{i+1,j} - 2z_{i,j} + z_{i-1,j}}{h^2} \\
\frac{\partial^2 z}{\partial y^2} &\approx z_{i,j}^{yy} &= \frac{z_{i,j+1} - 2z_{i,j} + z_{i,j-1}}{h^2} \\
\frac{\partial^2 z}{\partial xy} &\approx z_{i,j}^{xy} &= \frac{z_{i+1,j+1} - z_{i+1,j-1} - z_{i-1,j+1} + z_{i-1,j-1}}{4h^2}
\end{aligned}
\tag{B.0.3}
$$

and the second-order derivatives are

$$
\begin{aligned}
z_{\eta\eta} &\approx z_{i,j}^{\eta\eta} &= \frac{z_{i,j}^{xx}\left|z_{i,j}^x\right|^2 + 2z_{i,j}^{xy}z_{i,j}^x z_{i,j}^y + z_{i,j}^{yy}\left|z_{i,j}^y\right|^2}{\left|z_{i,j}^x\right|^2 + \left|z_{i,j}^y\right|^2} \\
z_{\xi\xi} &\approx z_{i,j}^{\xi\xi} &= \frac{z_{i,j}^{xx}\left|z_{i,j}^y\right|^2 - 2z_{i,j}^{xy}z_{i,j}^x z_{i,j}^y + z_{i,j}^{yy}\left|z_{i,j}^x\right|^2}{\left|z_{i,j}^x\right|^2 + \left|z_{i,j}^y\right|^2}
\end{aligned}
\tag{B.0.4}
$$

where η is parallel to the gradient and ξ is perpendicular to the gradient.

The absolute of the gradient is

$$|\nabla z| \approx |\nabla z_{i,j}| = \sqrt{m^2\left(z_{i,j}^{x+}, z_{i,j}^{x-}\right), m^2\left(z_{i,j}^{y+}, z_{i,j}^{y-}\right)} \tag{B.0.5}$$

where

$$
m(x,y) = \begin{cases} \frac{1}{2}\left[\text{sign}(x) + \text{sign}(y)\right]\min\left(|x|, |y|\right) & xy \geq 0 \\ 0 & xy < 0 \end{cases}
\tag{B.0.6}
$$

B.1 Diffusion

Equation 6.2.3 is

$$\text{div}\left[c_n\left(\nabla z\right)\nabla z\right] \quad \approx \quad c_{i,j}^{y+}z_{i,j}^{y+} + c_{i,j}^{x+}z_{i,j}^{x+} - c_{i,j}^{y-}z_{i,j}^{y-} - c_{i,j}^{x-}z_{i,j}^{x-} \tag{B.1.1}$$

where

$$
\begin{aligned}
c_{i,j}^{y+} &= c\left(z_{i,j}^{y+}\right) \\
c_{i,j}^{y-} &= c\left(z_{i,j}^{y-}\right) \\
c_{i,j}^{x+} &= c\left(z_{i,j}^{x+}\right) \\
c_{i,j}^{x-} &= c\left(z_{i,j}^{x-}\right)
\end{aligned}
\tag{B.1.2}
$$

B.2 Variation

The first term of Equation 6.2.8 is

$$\text{div}\left[c\left(\nabla z\right)\frac{\nabla z}{|\nabla z|}\right] \quad \approx \quad \text{Div}\left(z_{i,j}^n\right) \quad = \quad \frac{z_{i,j}^{xx}\left|z_{i,j}^y\right|^2 - 2z_{i,j}^{xy}z_{i,j}^x z_{i,j}^y + z_{i,j}^{yy}\left|z_{i,j}^x\right|^2}{\left(\left|z_{i,j}^x\right|^2 + \left|z_{i,j}^y\right|^2\right)^{\frac{3}{2}}} \tag{B.2.1}$$

Equation 6.2.9 is

$$\frac{1}{\sigma^2}\int \text{div}\left[c\left(\nabla z\right)\frac{\nabla z}{|\nabla z|}\right]\left(x-z\right)dxdy \quad \approx \quad \frac{\overline{\text{Div}\left(z_{i,j}^n\right)\left(x-z\right)}}{\sigma^2} \tag{B.2.2}$$

Equation 6.2.10 is

$$\frac{\text{div}\left[c(\nabla z)\frac{\nabla z}{|\nabla z|}\right]\left(x-z\right)}{\text{var}(x-z)} \quad \approx \quad G_\sigma * \left[\frac{\text{Div}\left(z_{i,j}^n\right)\left(x-z\right)}{\sigma^2}\right] \tag{B.2.3}$$

B.3 Shock Filter

Equation 6.2.11 is

$$-\text{sign}\left[c_b\left(z_{\eta\eta}\right)\right]\left|\nabla z\right| \quad \approx \quad -\text{sign}\left[c\left(z_{i,j}^{\eta\eta}\right)\right]\left|\nabla z_{i,j}\right| \tag{B.3.1}$$

List of References

[1] D. M. P. Smith, P. Meyer, and B. M. Herbst, "Image Reconstruction by means of Kalman Filtering in Passive Millimetre-Wave Imaging," in *South-East European Conference on Computational Mechanics*, Rhodes, Greece, 22–24 June 2009. 4, 14, 72, 77

[2] D. M. P. Smith, P. Meyer, and B. M. Herbst, "Image Reconstruction by means of Kalman Filtering in Passive Millimetre-Wave Imaging," *Journal of the Serbian Society for Computational Mechanics*, vol. 4, 2009. 4, 14, 72, 77

[3] R. Appleby and R. N. Anderton, "Millimeter-Wave and Submillimeter-Wave Imaging for Security and Surveillance," *Proceedings of the IEEE*, vol. 95, no. 8, pp. 1683–1690, August 2007. 6

[4] H. J. Liebe, "Atmospheric EHF Window Transparencies near 35, 90, 140, and 220 GHz," *IEEE Transactions on Antennas and Propagation*, vol. 31, no. 1, pp. 127–135, January 1983. 8

[5] J. E. Bjarnason, T. L. J. Chan, A. W. M. Lee, M. A. Celis *et al.*, "Millimeter-Wave, Terahertz, and Mid-Infrared Transmission through Common Clothing," *Applied Physics Letters*, vol. 85, no. 4, pp. 519–521, 26 July 2004. 8

[6] D. D. King, *Radar Handbook*, 1st ed. New York, USA: McGraw-Hill, 1970, ch. 39 – Passive Detection, pp. 39–1 to 39–36. 8

[7] F. T. Ulaby, R. K. Moore, and A. K. Fung, *Microwave Remote Sensing: Active and Passive*. Dedham, USA: Artech House, 1986, vol. 3. 8, 12

[8] L. Yujiri, M. Shoucri, and P. Moffa, "Passive Millimeter-Wave Imaging," *IEEE Microwave Magazine*, vol. 4, no. 3, pp. 39–50, September 2003. 9, 12

[9] W. J. Wilson, R. J. Howard, A. C. Ibbot, G. S. Parks *et al.*, "Millimeter-Wave Imaging Sensor," *IEEE Transactions on Microwave Theory and Techniques*, vol. 34, no. 10, pp. 1026–1035, October 1986. 9, 11, 13

[10] A. H. Lettington, D. Dunn, M. Attia, and I. M. Blankson, "Passive Millimetre-Wave Imaging Architectures," *Journal of Optics A: Pure and Applied Optics*, vol. 5, no. 4, pp. S103–S110, July 2003. 10

[11] A. H. Lettington, D. Dunn, N. E. Alexander, A. Wabby *et al.*, "Design and Development of a High Performance Passive MM-Wave Imager for Aeronautical Applications," in *Radar Sensor Technology and Passive Millimeter-Wave Imaging Technology*, vol. 5410, Orlando, USA, 14 April 2004, pp. 210–218. 11

[12] J. A. Lovberg, C. Martin, and V. Kolinko, "Video-Rate Passive Millimeter-Wave Imaging using Phased Arrays," in *IEEE MTT-S International Microwave Symposium Digest*, Honolulu, USA, 3–8 June 2007, pp. 1689–1692. 11

[13] G. S. Dow, D. C. W. Lo, Y. Guo, E. W. Lin *et al.*, "Large Scale W-Band Focal Plane Array for Passive Radiometric Imaging," in *IEEE MTT-S International Microwave Symposium Digest*, vol. 1, San Francisco, USA, 17–21 June 1996, pp. 369–372. 11

[14] G. Dow, T. N. Ton, H. Wang, D. C. W. Lo *et al.*, "W-Band MMIC Direct Detection Receiver for Passive Imaging System," in *IEEE MTT-S International Microwave Symposium Digest*, vol. 1, Atlanta, USA, 14–18 June 1993, pp. 163–166. 11, 13, 57

[15] V. Chandrasekar, H. Fukatsu, and K. Mubarak, "Global Mapping of Attenuation at Ku- and Ka-Band," *IEEE Transactions on Geoscience and Remote Sensing*, vol. 41, no. 10, pp. 2166–2176, October 2003. 11, 12

[16] R. Hopper, "System Solutions using MMW Sensors," in *Proceedings of the Automated RF and Microwave Measurement Society*, Newport Pagnell, UK, 7–8 November 2005. 12

[17] T. J. Greenwald and A. S. Jones, "Evaluation of Seawater Permittivity Models at 150 GHz using Satellite Observations," *IEEE Transactions on Geoscience and Remote Sensing*, vol. 37, no. 5, pp. 2159–2164, September 1999. 12

[18] L.-C. Shen, "Remote Probing of Atmosphere and Wind Velocity by Millimeter Waves," *IEEE Transactions on Antennas and Propagation*, vol. 18, no. 4, pp. 493–497, July 1970. 12

[19] G. Wadge, D. G. Macfarlane, D. A. Robertson, A. J. Hale *et al.*, "AVTIS: A Novel Millimetre-Wave Ground Based Instrument for Volcano Remote Sensing," *Journal of Volcanology and Geothermal Research*, vol. 146, no. 4, pp. 307–318, September 2005. 12

[20] J. W. Waters, L. Froidevaux, R. S. Harwood, R. F. Jarnot *et al.*, "The Earth Observing System Microwave Limb Sounder (EOS MLS) on the Aura Satellite," *IEEE Transactions on Geoscience and Remote Sensing*, vol. 44, no. 5, pp. 1075–1092, May 2006. 12

[21] C. Prigent, J. R. Pardo, and W. B. Rossow, "Comparisons of the Millimeter and Submillimeter Bands for Atmospheric Temperature and Water Vapor Soundings for Clear and Cloudy Skies," *Journal of Applied Meteorology and Climatology*, vol. 45, no. 12, pp. 1622–1633, December 2006. 12

[22] J. R. Pardo, M. C. Wiedner, E. Serabyn, C. D. Wilson *et al.*, "Side-by-Side Comparison of Fourier Transform Spectroscopy and Water Vapor Radiometry as Tools for the Calibration of Millimeter/Submillimeter Ground-Based Observatories," *Astrophysical Journal Supplement Series*, vol. 153, no. 1, pp. 363–367, July 2004. 12

[23] AAI, "Aerosonde Mark 4.4." 13

[24] BAE Systems, "Silver Fox," 30 July 2009. 13

[25] BAI Aerosystems, "Viking 100." 13

[26] M. Sato, T. Hirose, T. Ohki, H. Sato *et al.*, "94-GHz Band High-Gain and Low-Noise Amplifier using InP-HEMTs for Passive Millimeter Wave Imager," in *IEEE MTT-S International Microwave Symposium Digest*, Honolulu, USA, 3–8 June 2007, pp. 1775–1778. 13, 57

[27] Analog Devices, "AD8318 – 1 MHz to 8 GHz, 70 dB Logarithmic Detector/Controller," 2007, rev. B. 13, 57

[28] Analog Devices, "AD8319 – 1 MHz to 10 GHz, 45 dB Log Detector/Controller," 2008, rev. B. 13, 57

[29] Hittite, "Catalog," 2009. 13, 57

[30] Spacek Labs, "MKa-8 Mixer," 17 September 2008. 13, 58

[31] Spacek Labs, "GKa-420 Mechanically Tuned Gunn Oscillator," 15 February 2007. 13, 59

[32] Lucix, "RF/Microwave Amplifiers," 2009. 13, 64, 65

[33] QuinStar, "Catalog," 2009. 14, 20, 25, 27, 63, 64, 65

[34] R. E. Kalman, "A New Approach to Linear Filtering and Prediction Problems," *Transactions of the ASME – Journal of Basic Engineering*, vol. 82, no. Series D, pp. 35–45, March 1960. 14, 77

[35] E. Knox-Davies, "Construction and Measurement of a 29 – 37 GHz Frequency-Scanned Antenna for a Millimetre-Wave Imager," December 2007. 15, 19

[36] C. A. Balanis, *Antenna Theory, Analysis and Design*, 2nd ed. New York, USA: John Wiley & Sons, 1997. 15, 25

[37] T. A. Milligan, *Modern Antenna Design*, 2nd ed. Hoboken, USA: John Wiley & Sons, 2005. 16, 17, 19, 21, 23

[38] J. Frank and J. D. Richards, *Radar Handbook*, 3rd ed. New York, USA: McGraw-Hill, 2008, ch. 13 – Phased Array Radar Antennas, pp. 13.1 – 13.74. 16, 17

[39] I. W. Hammer, *Radar Handbook*, 1st ed. New York, USA: McGraw-Hill, 1970, ch. 13 – Frequency-scanned Arrays, pp. 13–1 to 13–27. 18

[40] A. Villeneuve, "Taylor Patterns for Discrete Arrays," *IEEE Transactions on Antennas and Propagation*, vol. 32, no. 10, pp. 1089–1093, October 1984. 19

[41] R. Elliott, "On the Design of Traveling-Wave-Fed Longitudinal Shunt Slot Arrays," *IEEE Transactions on Antennas and Propagation*, vol. 27, no. 5, pp. 717–720, September 1979. 19

[42] CST, "Microwave Studio," 2009. 19, 22, 44, 48, 50, 52

[43] Agilent, "8510C 45 MHz to 50 GHz Network Analyzer," 11 July 2006. 20, 53, 54, 63

[44] M. E. Cooley and D. Davis, *Radar Handbook*, 3rd ed.   New York, USA: McGraw-Hill, 2008, ch. 12 –
      Reflector Antennas, pp. 12.1 – 12.43. 21

[45] EMSS, "FEKO Suite," 2009. 22

[46] Emerson & Cuming, "Eccosorb HR: Lightweight Flat-Sheet Broadband Microwave Absorbers," Wes-
      terlo, Belgium, June 2007. 23, 67

[47] E. B. Joy, W. M. Leach, G. P. Rodrigue, and D. T. Paris, "Applications of Probe-Compensated Near-
      Field Measurements," *IEEE Transactions on Antennas and Propagation*, vol. 26, no. 3, pp. 379–389,
      May 1978. 25

[48] Agilent, "8514B 45MHz to 20GHz *S*-Parameter Test Set," 1 July 2001. 27

[49] MathWorks, "Matlab," 2009. 30

[50] Rohde&Schwarz, "FSEK30 20Hz–40GHz Spectrum Analyzer." 33, 59, 63, 68

[51] R. J. Wenzel, "Application of Exact Synthesis Methods to Multichannel Filter Design," *IEEE Transac-
      tions on Microwave Theory and Techniques*, vol. 13, no. 1, pp. 5–15, January 1965. 36

[52] R. J. Wenzel, "Wideband High-Selectivity Diplexers utilizing Digital Elliptic Filters," *IEEE Transactions
      on Microwave Theory and Techniques*, vol. 15, no. 12, pp. 669–680, December 1967. 36

[53] J. D. Rhodes and R. Levy, "A Generalized Multiplexer Theory," *IEEE Transactions on Microwave
      Theory and Techniques*, vol. 27, no. 2, pp. 99–111, February 1979. 36

[54] J. D. Rhodes and S. A. Alseyab, "A Design Procedure for Bandpass Channel Multiplexers Connected
      at a Common Junction," *IEEE Transactions on Microwave Theory and Techniques*, vol. 28, no. 3, pp.
      246–253, March 1980. 36

[55] J.-A. Gong and W.-K. Chen, "Computer-Aided Design of a Singly-Matched (S-M) Multiplexer with a
      Common Junction," *IEEE Transactions on Microwave Theory and Techniques*, vol. 41, no. 5, pp. 886–
      890, May 1993. 36

[56] E. G. Cristal and G. L. Matthaei, "A Technique for the Design of Multiplexers Having Contiguous
      Channels," *IEEE Transactions on Microwave Theory and Techniques*, vol. 12, no. 1, pp. 88–93, January
      1964. 36

[57] P. M. LaTourrette, "Multi-Octave Combline-Filter Multiplexer," in *IEEE MTT-S International Micro-
      wave Symposium Digest*, vol. 77, no. 1, June 1977, pp. 298–301. 36

[58] P. M. LaTourrette and J. L. Roberds, "Extended-Junction Combline Multiplexers," in *IEEE MTT-S Inter-
      national Microwave Symposium Digest*, vol. 78, no. 1, June 1978, pp. 214–216. 36, 47

[59] D. M. Pozar, *Microwave Engineering*, 3rd ed.   Hoboken, USA: John Wiley & Sons, 2005. 37, 38

[60] R. J. Cameron and M. Yu, "Design of Manifold-Coupled Multiplexers," *IEEE Microwave Magazine*,
      vol. 8, no. 5, pp. 46–59, October 2007. 37, 38, 39

[61] F. S. Coale, "A Traveling-Wave Directional Filter," *IRE Transactions on Microwave Theory and Techniques*, vol. 4, no. 4, pp. 256–260, October 1956. 37

[62] F. S. Coale, "Applications of Directional Filters for Multiplexing Systems," *IRE Transactions on Microwave Theory and Techniques*, vol. 6, no. 4, pp. 450–453, October 1958. 37

[63] J. E. Dean and J. D. Rhodes, "Design of MIC Broadband Contiguous Multiplexers," in *IEEE MTT-S International Microwave Symposium Digest*, vol. 80, no. 1, May 1980, pp. 147–149. 38

[64] J. D. Rhodes and R. Levy, "Design of General Manifold Multiplexers," *IEEE Transactions on Microwave Theory and Techniques*, vol. 27, no. 2, pp. 111–123, February 1979. 39

[65] J. W. Bandler, S. Daijavad, and Q.-J. Zhang, "Exact Simulation and Sensitivity Analysis of Multiplexing Networks," *IEEE Transactions on Microwave Theory and Techniques*, vol. 34, no. 1, pp. 93–102, January 1986. 39

[66] J. W. Bandler and Q.-J. Zhang, "An Automatic Decomposition Approach to Optimization of Large Microwave Systems," *IEEE Transactions on Microwave Theory and Techniques*, vol. 35, no. 12, pp. 1231–1239, December 1987. 39

[67] C. Rauscher, "Efficient Design Methodology for Microwave Frequency Multiplexer Using Infinite-Array Prototype Circuits," *IEEE Transactions on Microwave Theory and Techniques*, vol. 42, no. 7, pp. 1337–1346, July 1994. 39

[68] L. Accatino and M. Mongiardo, "Hybrid Circuit-Full-Wave Computer-Aided Design of a Manifold Multiplexers without Tuning Elements," *IEEE Transactions on Microwave Theory and Techniques*, vol. 50, no. 9, pp. 2044–2047, September 2002. 39, 51

[69] J. R. Montejo-Garai, J. A. Ruiz-Cruz, and J. M. Rebollar, "Full-Wave Design of *H*-Plane Contiguous Manifold Output Multiplexers Using the Fictitious Reactive Load Concept," *IEEE Transactions on Microwave Theory and Techniques*, vol. 53, no. 8, pp. 2628–2632, August 2005. 39, 42, 51

[70] A. Morini, T. Rozzi, and M. Mongiardo, "Efficient CAD of Wideband Contiguous Channel Multiplexers," in *IEEE MTT-S International Microwave Symposium Digest*, vol. 3, 17–21 June 1996, pp. 1651–1654. 39, 51

[71] A. Morini, T. Rozzi, and M. Morelli, "New Formulae for the Initial Design in the Optimization of T-Junction Manifold Multiplexers," in *IEEE MTT-S International Microwave Symposium Digest*, vol. 2, 8–13 June 1997, pp. 1025–1028. 39, 51

[72] A. Morini and T. Rozzi, "Constraints to the Optimum Performance and Bandwidth Limitations of Diplexers Employing Symmetric Three-Port Junctions," *IEEE Transactions on Microwave Theory and Techniques*, vol. 44, no. 2, pp. 242–248, February 1996. 39

[73] Rogers, "RO4000 Series High Frequency Circuit Materials," 11 February 2007. 41

[74] G. L. Matthaei and G. L. Hey-Shipton, "Novel Staggered Resonator Array Superconducting 2.3-GHz Bandpass Filter," *IEEE Transactions on Microwave Theory and Techniques*, vol. 41, no. 12, pp. 2345–2352, December 1993. 42

[75] G. L. Matthaei, L. Young, and E. M. T. Jones, *Microwave Filters, Impedance-Matching Networks, and Coupling Structures*. Norwood, USA: Artech House, 1980. 43, 44, 60, 61

[76] S. Srisathit, S. Patisang, R. Phromloungsri, S. Bunnjaweht *et al.*, "High Isolation and Compact Size Microstrip Hairpin Diplexer," *IEEE Microwave and Wireless Components Letters*, vol. 15, no. 2, pp. 101–103, February 2005. 47

[77] M. H. Weng, C. Y. Hung, and Y. K. Su, "A Hairpin Line Diplexer for Direct Sequence Ultra-Wideband Wireless Communications," *IEEE Microwave and Wireless Components Letters*, vol. 17, no. 7, pp. 519–521, July 2007. 47

[78] AWR, "Microwave Office," 2008. 48, 52

[79] R. Levy, "New Coaxial-to-Stripline Transformers using Rectangular Lines," *IRE Transactions on Microwave Theory and Techniques*, vol. 9, no. 3, pp. 273–274, May 1961. 48

[80] E. H. England, "A Coaxial to Microstrip Transition," *IEEE Transactions on Microwave Theory and Techniques*, vol. 24, no. 1, pp. 47–48, January 1976. 48

[81] J. Chenkin, "DC to 40 GHz Coaxial-to-Microstrip Transition for 100-μm-Thlck GaAs Substrates," *IEEE Transactions on Microwave Theory and Techniques*, vol. 37, no. 7, pp. 1147–1150, July 1989. 48

[82] C. N. Capsalis, C. P. Chronopoulos, and N. K. Uzunoglu, "A Rigorous Analysis of a Coaxial to Shielded Microstrip Line Transition," *IEEE Transactions on Microwave Theory and Techniques*, vol. 37, no. 7, pp. 1091–1098, July 1989. 48

[83] J. S. Wight, O. P. Jain, W. J. Chudobiak, and V. Makios, "Equivalent Circuits of Microstrip Impedance Discontinuities and Launchers," *IEEE Transactions on Microwave Theory and Techniques*, vol. 22, no. 1, pp. 48–52, January 1974. 48

[84] M. L. Majewski, R. W. Rose, and J. R. Scott, "Modeling and Characterization of Microstrip-to-Coaxial Transitions," *IEEE Transactions on Microwave Theory and Techniques*, vol. 29, no. 8, pp. 799–805, August 1981. 48

[85] Southwest Microwave, "Catalog," 26 June 2008. 49, 50

[86] W. Schwab and W. Menzel, "On the Design of Planar Microwave Components using Multilayer Structures," *IEEE Transactions on Microwave Theory and Techniques*, vol. 40, no. 1, pp. 67–72, January 1992. 51

[87] R. Levy, "Analytical Design of Contiguous Multiplexers," in *IEEE MTT-S International Microwave Symposium Digest*, vol. 3, Anaheim, USA, 13–19 June 1999, pp. 899–902. 51

[88] HP, "8671B 2 to 18GHz Synthesized CW Generator." 57, 58, 68

[89] Tektronix, "TDS 340A, TDS 360 & TDS 380 Digital Real-Time Oscilloscopes." 57, 58

[90] Weger, "Apparent Sky Temperatures in the Microwave Region," *Journal of Meteorology*, vol. 17, pp. 159–165, April 1960. 66

[91] Narda, "Catalog." 68

[92] Agilent, "8349B 2 to 20GHz High Performance Broadband Amplifer," 1 December 1990. 68

[93] Agilent, "83554A 26.5 to 40GHz mm-wave Source Module," 29 November 2001. 68

[94] P. Perona and J. Malik, "Scale-Space and Edge Detection Using Anisotropic Diffusion," *IEEE Transactions on Pattern Analysis and Machine Intelligence*, vol. 12, no. 7, pp. 629–639, July 1990. 74

[95] G. Gilboa, N. Sochen, and Y. Zeevi, "Forward-and-Backward Diffusion Processes for Adaptive Image Enhancement and Denoising," *IEEE Transactions on Image Processing*, vol. 11, no. 7, pp. 689–703, July 2002. 75

[96] G. Gilboa, N. Sochen, and Y. Y. Zeevi, "Image Enhancement and Denoising by Complex Diffusion Processes," *IEEE Transactions on Pattern Analysis and Machine Intelligence*, vol. 26, no. 8, pp. 1020–1036, August 2004. 75, 76

[97] L. I. Rudin, S. Osher, and E. Fatemi, "Nonlinear Total Variation Based Noise Removal Algorithms," *Physica D: Nonlinear Phenomena*, vol. 60, no. 1–4, pp. 259–268, November 1992. 75

[98] G. Gilboa, N. Sochen, and Y. Y. Zeevi, "Texture Preserving Variational Denoising Using an Adaptive Fidelity Term," in *Proceedings of the Variational, Geometric and Level Set Methods in Computer Vision*, Nice, France, 11–12 October 2003, pp. 137–144. 75

[99] A. Marquina and S. Osher, "Explicit Algorithms for a New Time Dependent Model Based on Level Set Motion for Nonlinear Deblurring and Noise Removal," *SIAM Journal on Scientific Computing*, vol. 22, no. 2, pp. 387–405, 2000. 75

[100] M. Lysaker, S. Osher, and X.-C. Tai, "Noise Removal using Smoothed Normals and Surface Fitting," *IEEE Transactions on Image Processing*, vol. 13, no. 10, pp. 1345–1357, October 2004. 75

[101] S. Osher and L. I. Rudin, "Feature-Oriented Image Enhancement Using Shock Filters," *SIAM Journal on Numerical Analysis*, vol. 27, no. 4, pp. 919–940, Augusts 1990. 76

[102] L. Alvarez and L. Mazorra, "Signal and Image Restoration Using Shock Filters and Anisotropic Diffusion," *SIAM Journal on Numerical Analysis*, vol. 31, no. 2, pp. 590–605, April 1994. 76

[103] O. Coulon and S. R. Arridge, "Dual Echo MR Image Processing Using Multi-Spectral Probabilistic Diffusion Coupled with Shock Filters," in *British Conference on Medical Image Understanding and Analysis*, London, UK, 2000, pp. 141–144. 76

[104] S. J. Julier, J. K. Uhlmann, and H. F. Durrant-Whyte, "A New Approach for Filtering Nonlinear Systems," in *Proceedings of the American Control Conference*, vol. 3, Seattle, USA, 21–23 June 1995, pp. 1628–1632. 77, 79

[105] D. Simon, "Kalman Filtering for Fuzzy Discrete Time Dynamic Systems," *Applied Soft Computing*, vol. 3, no. 3, pp. 191–207, November 2003. 77

[106] D. Mackenzie, "Ensemble Kalman Filters Bring Weather Models Up to Date," *SIAM News*, vol. 36, no. 8, pp. 1–4, October 2003. 77

[107] E. L. Haseltine and J. B. Rawlings, "Critical Evaluation of Extended Kalman Filtering and Moving-Horizon Estimation," *Industrial and Engineering Chemistry Research*, vol. 44, no. 8, pp. 2451–2460, 2005. 77

[108] R. van der Merwe, E. A. Wan, and S. J. Julier, "Sigma-Point Kalman Filters for Nonlinear Estimation and Sensor-Fusion – Applications to Integrated Navigation," in *AIAA Guidance, Navigation, and Control Conference and Exhibit*, no. 5120, Providence, USA, 16–19 August 2004. 77

[109] S.-L. Sui, J. Yuan, and W.-X. Zhang, "Unscented Kalman Filter based Autonomous Optical Navigation Method," in *Chinese Control Conference*, Harbin, China, 7–11 August 2006, pp. 403–406. 77

[110] K. Xiong, L. D. Liu, and H. Y. Zhang, "Modified Unscented Kalman Filtering and its Application in Autonomous Satellite Navigation," *Aerospace Science and Technology*, vol. 13, no. 4–5, pp. 238–246, June–July 2009. 77

[111] J. Andrade-Cetto, "The Kalman Filter," Institut de Robòtica i Informàtica Industrial, Universitat Politècnica de Catalunya, Barcelona, Spain, Tech. Rep. IRI-DT-02-01, May 2005. 79, 81